

IJCESEN

ISSN : 2149-9144

International

Journal of

Computational and

Experimental

Science and

ENgineering

Volume: 5 - No:1 - 2019

ijcesen@gmail.com

Founder-Editor-in-Chief : **Prof.Dr. İskender AKKURT**

dergipark.gov.tr/ijcesen

Journal Info	
Web	dergipark.gov.tr/ijcesen
E-mail	ijcesen@gmail.com
ISSN	2149-9144
Frequency	March-July-November
Founded	2015
Journal Abbreviation	IJCESEN
Language	English-Turkish
Founder-Editor-in-Chief	
Prof.Dr. İskender AKKURT	Suleyman Demirel University-TURKEY
Editorial Board	
Prof.Dr. Mahmut DOGRU	Fırat University- TURKEY
Prof.Dr.Mitra DJAMAL	Institut Teknologi Bundung-INDONESIA
Prof.Dr. Sevil Cetinkaya GÜNER	Cumhuriyet University- TURKEY
Prof.Dr. Mohamed EL TOKHI	United Arab Emirates University-UAE
Prof.Dr. Nezam AMİRİ	Sharif University-IRAN
Prof.Dr. Berin SİRVANLI	Gazi University- TURKEY
Prof.Dr. Abdelmadjid RECIUI	M'Hamed Bougara University, ALGERIA
Dr. Nabi IBADOV	Warsaw University of Technology-POLAND
Dr. Yusuf CEYLAN	Selçuk University-TURKEY
Dr. Fengrui SUN	China University of Petroleum, Beijing, CHINA
Dr. Zuhale ER	Istanbul Technical University- TURKEY
Dr. Nurten Ayten UYANIK	Isparta Uygulamalı Bilimler University- TURKEY
Dr. Amer AL ABDEL HAMİD	Yarmouk University-JORDAN
Dr. Zehra Nur KULUÖZTÜRK	Bitlis Eren University- TURKEY
Dr. Dhafer ALHALAFI	De Montfort University, Leicester-UK
Dr. Zeynep PARLAR	Istanbul Technical University- TURKEY
Dr. Mandi ORLİC BACHLER	Zagreb University of Applied Sciences-CROATIA
Dr. M. Fatih KULUÖZTÜRK	Bitli Eren University- TURKEY
Dr. Irida MARKJA	University of Tirana-ALBANIA
Dr. Kadir GÜNOĞLU	Isparta Uygulamalı Bilimler University- TURKEY
Dr. Ahmet BEYÇİOĞLU	Adana Bilim Teknoloji University- TURKEY
Dr. Hakan AKYILDIRIM	Suleyman Demirel University- TURKEY
Dr. Zakaria MAAMAR	Zayed University-UAE
Dr. Tomasz PIOTROWSKI	Warsaw University of Technology-POLAND

Table of Contents

Volume: 5	No: 1	March-2019	
Authors	Title	DOI:	Pages
Wei ZHAO, Huiqing LIU, Chuan LU, Jing WANG, Lin MENG, Ruihong ZHONG	Experimental Investigation of CSS Assisted by Gas-viscosity Reducer Co-Injection with Different Types of Wells and Heavy Oil	10.22399/ijcesen.485188	1-9
Burak SEVİN, Su Buse ŞAHİN	Determination of The Cross Types to be used in a Trailer Chassis by Finite Element Method	10.22399/ijcesen.477613	10-18
Atilla EVCİN, Bahri ERSOY, Hakan ÇİFTÇİ	Utilization of Marble and Boron Waste in Brick Products	10.22399/ijcesen.480487	19-22
Billur ECER, Ahmet AKTAŞ	Clustering of European Countries in terms of Healthcare Indicators	10.22399/ijcesen.416611	23-26
Tolga PALANDIZ, Ramazan ŞENOL, Hilmi Cenk BAYRAKÇI	Optimization Of Traffic Signalization For Complex Roundabout By Fuzzy Logic According To Various Parameters	10.22399/ijcesen.446666	27-30
Iredia ERHUNMWUN, John AKPOBI	Effect of Change in Radial Clearance on Pressure Variation of Fluid in Hydrodynamic Journal Bearing	10.22399/ijcesen.492548	31-36
Jian SUN, Qi LI, Mingqiang CHEN, Zekai ZHANG	The Key Factor Analysis to the Reservoirs on the Basis of Bayesian Law	10.22399/ijcesen.422691	37-42
Ahmet AKSÖZ, Ali SAYGIN	Decreasing the Cogging Torque using Virtual Positive Impedance Based Active Damping Control Method for PMSMs	10.22399/ijcesen.522865	43-47
Hadi ALBIDHANI, Kadir GUNOGLU, Iskender AKKURT	Natural Radiation Measurement in Some Soil Samples from Basra oil field, IRAQ State	10.22399/ijcesen.498695	48-51
Mehmet ŞAHBAZ, Hasan KAYA, Aykut KENTLI, Mehmet UÇAR, Serkan ÖĞÜT, Kerim ÖZBEYAZ	Experimental Comparison of Al5083 Alloy Subjected to Annealing and Equal-Channel Angular Pressing	10.22399/ijcesen.394542	52-55



Experimental Investigation of CSS Assisted by Gas-viscosity Reducer Co-Injection with Different Types of Wells and Heavy Oil

Wei ZHAO^{1,2*}, Huiqing LIU^{1,2}, Chuan LU³, Jing WANG^{1,2}, Lin MENG⁴ and Ruihong ZHONG^{1,2}

¹ State Key Laboratory of Petroleum Resources and Engineering in China University of Petroleum, Beijing, China;

² MOE Key Laboratory of Petroleum Engineering in China University of Petroleum, Beijing, China;

³ Research Institute of China National Offshore Oil Corporation, Beijing, China;

⁴ Department of Chemical & Petroleum Engineering, University of Calgary, Calgary, AB, Canada T2N1N4

* Corresponding Author : zhaoweicup@126.com

ORCID: 0000-0001-7439-4258

Article Info:

DOI: 10.22399/ijcesen.485188

Received : 19 November 2018

Accepted : 12 December 2018

Keywords

Cyclic steam stimulation

EOR

Viscosity reducer

Non-condensable gas

Abstract:

The efficiency of conventional thermal recovery methods is limited due to heat loss, steam overlapping and other factors. Steam injection assisted by various additives, such as no-condensable gas, solvent and surfactant, has proved to be an effective and beneficial method to improve thermal oil recovery. However, based on previous studies, systematic and comprehensive investigation of the compound system of gas-chemical agent and the application criteria is lacking.

In this paper, a 3D physical model with different types of wells and heavy oil were designed. The additives consist of nitrogen and viscosity reducer (VR). Different injection fluid combinations (single gas, single VR and gas-VR co-injection), fluid injection configurations (gas-steam and gas+steam, VR-steam and VR+steam,) were applied to investigate the effects of the compound system on oil recovery, oil-steam ratio and oil production rate.

The results indicated that steam injection assisted by gas-VR performs effectively in enhancing the thermal recovery. The conclusions are drawn according to the variation curves of characteristic parameters. The effects of the compound system kept increasing the oil recovery after different injection patterns. Meanwhile, the cumulative SOR decreased after the corresponding processes sequentially. The distribution of temperature showed that gas-VR co-injection not only inhibited steam overlapping, which promoted the horizontal expansion of the steam chamber but also reduced the viscosity of heavy oil significantly. More oil was produced due to the gas expansion. In summary, this work provides a practical understanding of CSS assisted by gas-VR co-injection and optimization of the injection schemes for different types of reservoirs.

1. Introduction

With the decrease of conventional oil reserves and increase of the oil demand, heavy oil resources attract more attention of petroleum engineers. A series of thermal recovery techniques, such as cyclic steam stimulation (CSS), steam flooding, steam assisted gravity drainage (SAGD) are developed to enhance the heavy oil recovery [1,11,18]. However, the efficiency of conventional thermal recovery methods is limited due to heat

loss, steam overlapping and other factors. Steam injection assisted by various additives, such as no-condensable gas, solvent and surfactant, has proved to be an effective and beneficial method to improve thermal oil recovery.

Non-condensate gas, such as nitrogen and CO₂, were always used as a heat insulation agent [2,9,17]. It turned out to be beneficial for the EOR process. The mechanisms of steam injection assisted by no-condensate gas mainly include higher swelling effect, lower heat conductivity

coefficient and interfacial-tension reduction [6,9,15] by using 2-D visualized model. The microscopic pictures displayed the oil displacement.

The chemical agents such as surfactant and solvent have also been used to assist the steam injection [4,8,14]. Due to low cost and stable properties, surfactant was applied to the process of thermal recovery, especially for viscosity reduction [7]. It has been shown that solvent additives can improve oil production rates with reduced steam injection [5,10]. However, most studies just showed the mechanism of gas and chemical agent separately [3,12]. Few systematic and comprehensive explanations were given to state the mechanism of the compound system of gas-chemical agent and the application conditions.

In this paper, a series of experiments were conducted to study the effect of gas and viscosity-reducer injected with steam during the CSS stage. Different injection fluids, injection orders and injection patterns were investigated to study the effects of the compound system on oil recovery, oil-steam ratio and oil production rate.

2. Experimental apparatus and procedures

2.1 Experimental apparatus

As shown in Figure 1, the setup for the experiments consisted of five subsystems: injection system, energy-supply system, temperature-pressure monitoring system, 3D physical simulation system, and fluid-data acquisition system. The injection system consisted of an ISCO pump, a steam generator, a nitrogen tank, a gas mass flow controller, a heating belt and a cylindrical tank. The 3D reservoir model was a stainless-steel container, with the dimensions of 36cm in length, 36cm in width and 21cm in depth. The maximum tolerance pressure of the model was 3Mpa. The 3D model could be used to simulate development with different types of the reservoirs and wells, different injection patterns and different injection fluids. The whole model was in the thermotank to maintain the constant temperature. The monitoring system included 36 temperature transducers and 8 pressure transducers. In the process of experiment, all these transducers were placed evenly in the model to detect the variation of the temperature and pressure with time. The data was recorded by the acquisition system. The energy-supply system was a cylindrical vessel filled with oil and compressed gas to provide energy for the physical model. A hand pump and a back-pressure regulator were installed in the outlet ensuring the stable production of the oil wells under reservoir pressure.

Comparing with the actual reservoir scale, the 3D physical model is relatively small. For the accuracy and reliability of experiments, the similarity criteria were established. Here, Pujol-Boberg's similarity criteria were used to calculate the designed parameters [13]. Table 1 shows the similarity criterion numbers of cyclic steam stimulation for heavy oil reservoir.

Table 1 Similarity criterion numbers of cyclic steam stimulation for heavy oil reservoir

Parameters	Similarity Criterion	Physical Meaning
Vertical well spacing or horizontal well length	L	Geometric similarity
Permeability	$\frac{K\rho_o g t}{\phi(1-S_{wc}-S_{or})\mu_o L}$	Darcy's law
Production time	$\frac{\alpha t}{L^2}$	Dimensionless time
Production pressure difference	$\frac{\Delta P}{\rho_o g L}$	Ratio of pressure and gravity
Steam injection rate	$\frac{i_s t}{\phi(1-S_{wc}-S_{or})\rho_w L^3}$	Ratio of flow volume and storage volume

In Table 1, L is vertical well spacing or horizontal well length, m. K is permeability of prototype or simulation model, $10^{-3}\mu\text{m}^2$. ρ_o is the oil density, g/cm^3 . g is the gravitational acceleration, m/s^2 . t is time, s. ϕ is the porosity of prototype or simulation model. S_{wc} is the irreducible water saturation. S_{or} is the residual oil saturation. μ_o is the oil viscosity, $\text{mPa}\cdot\text{s}$. α is the thermal diffusion coefficient, m^2/s . ΔP is the differential pressure of production, MPa. i_s is the steam injection rate. ρ_w is the water density, g/cm^3 .

According to the similarity criteria, we can get the physical simulation parameters table based on the actual parameters of reservoir and internal parameters of 3D physical model, as shown in Table 2.

2.2 Experimental procedures

In this study, 3D physical model which included CSS in vertical well model with extra-heavy oil and CSS in horizontal well model with ultra-heavy oil were conducted. We named Set 1 and Set 2 for the 3D experiments, respectively. The processes were as follows:

Set 1: (1) The washed quartz sand and oil sample were prepared firstly. (2) The oil and the sand were mixed according to the designed proportion (volume ratio=7:13). The clay was used to simulate the capping bed covering the oil layer. The vertical well was installed in the middle of the model. It was covered by the 300 meshes filter to prevent sand production.

Table 2. Experimental parameters during different CSS stages.

		VERTICAL WELL		HORIZONTAL WELL	
Parameter		Prototype	Model	Prototype	Model
Basic parameters	Length of horizontal well (m, cm)	-	-	150	30
	Reservoir thickness (m, cm)	16	10.24	3	6
	Porosity (%)	31	35	27	35
	Absolute permeability (10^{-16}m^2)	1250	146000	1120	70500
	Oil density (g/cm^3)	0.9709	0.9362	0.9794	0.9888
	Initial oil saturation (%)	70	100	65	100
	Reservoir temperature (°C)	25	25	25	25
	Oil viscosity at 25°C (mPa·s)	16715	10688	52405	50910
	Steam temperature (°C)	250	250	250	250
	Steam quality	0.7	0.7	0.7	0.7
CSS stage	Steam injection rate (t/d, ml/min)	80	401	170	28
	Steam injection time (d, min)	10	0.59	10	10
	Soaking time (d, min)	4	0.24	3	1.73
	Cycle increase rate (%)	15	15	10	10
	Production time (a, min)	1	21.53	1/6	35.04
	Production rate (t/d, ml/min)	2000	200	7000	700
CSS assisted by gas stage	Gas injection rate (t/d, ml/min)	1	1	2	2
	Gas injection rate (t/d, ml/min)	400	40	1400	140
	Gas injection time (d, min)	5	5	10	10
	Gas injection rate (t/d, ml/min)	4.69	8.7	3.15	5.83
CSS assisted by VR stage	VR concentration (wt.%)	0.5	0.5	0.4	0.4
	Liquid injection rate (t/d, ml/min)	0.94	1.74	0.63	1.17
	VR concentration (wt.%)	0.5	0.5	0.4	0.4
	VR concentration (wt.%)	0.5	0.5	0.4	0.4
CSS assisted by gas-VR co-injection stage	Gas injection rate (t/d, ml/min)	400	40	1400	140
	Liquid injection rate (t/d, ml/min)	0.94	1.74	0.63	1.17
	VR concentration (wt.%)	0.5	0.5	0.4	0.4

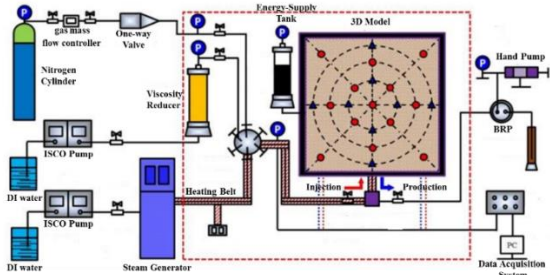


Figure 1. Schematic diagram of the experimental setup for the 3D experiments

During the process of filling the model with oil sands, all the temperature and pressure transducers were placed in the designed locations. After the reservoir thickness reached the designed value (10.24cm), the clay was used to fill the top capping bed (3) Check the tightness of the model to prevent oil leakage. The sealed model was pressurized by nitrogen under 3MPa for 12h. The leakage of the model was estimated based on the pressure variation. (4) According to the designed parameters, four displacement schemes were carried out. The produced fluid was collected by the measuring cylinder. When the oil-steam ratio is 0.1, stop the experiments. Figure 2 shows the section diagram of the vertical model. It displays the

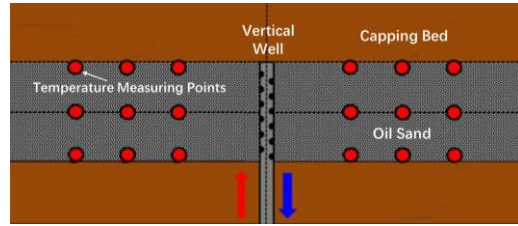


Figure 2 Section diagram of vertical-well model in extra heavy oil reservoir

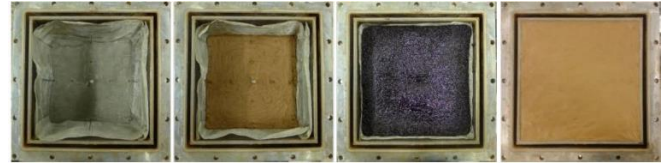


Figure 3. The preparation process of vertical-well model in extra heavy oil reservoir

internal situation of the model. Figure 3 shows the preparation process of vertical-well model in extra heavy oil reservoir.

Set 2: (1) The experimental preparation process was exactly the same with Set 1 except the oil samples and the well type. The oil was ultra-heavy oil and the well was horizontal well with the length of 30cm. (2) In this section, the reservoir thickness was 6cm. The filling and sealing process were also the same with Set 1. (3) There were also four patterns to be used as the designed parameters table. Figure 4 shows the section diagram of horizontal-well model. Figure 5 shows the preparation process of horizontal-well model in ultra-heavy oil reservoir. The location of the temperature measuring points was displayed visually.

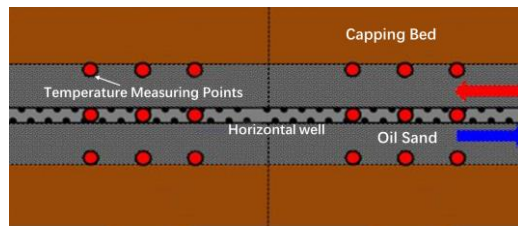


Figure 4. Section diagram of horizontal-well model in ultra-heavy oil reservoir

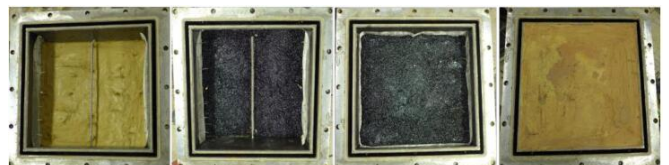


Figure 5. The preparation process of horizontal-well model in ultra-heavy oil reservoir

3. Results and discussion

3.1 Experimental Results of Set 1

CSS using vertical well in extra-heavy oil model was conducted in Set 1, different injection fluids, injection orders and injection patterns were applied to study the effect of EOR. The results were as follows:

(1) CSS Stage

As show in Figure 6, in the stage of CSS, the steam expanded and moved upwards under the action of gravity segregation which resulted in higher temperature at the top of the reservoir and lower temperature at the bottom of the reservoir. Figure 4a and 4b showed the direction of the section area. Both of these represented the same situation of CSS stage at the same time, just in different directions. With the increase of CSS cycles, the steam overlapping became more severe, leading to the stronger heterogeneity of vertical and horizontal expansion. At the end of CSS, the temperature of top, middle and bottom layer were 68.1°C, 50.5°C and 44.5°C, respectively. It can be seen that the temperature difference was obvious.

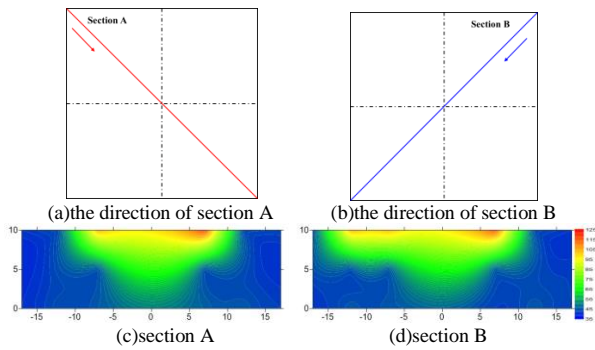


Figure 6. Vertical distribution of temperature at the end of CSS stage

Figure 7 shows the variation curves of characteristic parameters including oil production rate and cumulative oil-steam ratio during CSS stage. At the initial stage of CSS, the oil saturation around the well was high. Under the condition of high-temperature steam, the heavy oil volume expanded, and the viscosity reduced which led to a high production rate. However, with the increase of CSS cycles, the oil production rate decreased and then remained stable. According to Figure 5, it can be seen that the stable cumulative oil-steam ratio was 0.16.

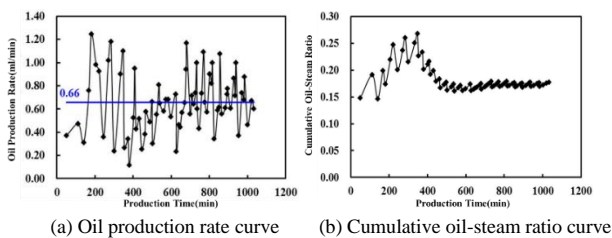


Figure 7. Variation curves of characteristic parameters during CSS stage

(2) CSS Assisted by Gas Stage

Single injection process: according to the designed scheme, single injection was first applied with nitrogen injection first and then steam injection. The fluid-acquisition-data indicated that the incremental oil recovery factor was 6.19%. Figure 6(a) showed that the temperature of top, middle and bottom layer were 64.9°C, 53.5°C and 46.5°C, respectively. Compared with the temperature of CSS stage, it can be seen that the temperature of middle and bottom layers increased, on the contrary, the top layer temperature decreased. It indicated that nitrogen injection inhibited the steam overlapping phenomenon because the gas reached the top layer firstly and pushed the steam down which promoted the vertical expansion of the steam chamber. However, the effect on the horizontal expansion of steam chamber was not significant.

Mixed injection process: after the single injection process was finished, the mixed injection process was conducted. The total recovery was 26.85%, increased by 5.39% than last process. As show in Figure 7(b), the heating area in horizontal direction increased obviously and the steam overlapping was further restrained compared with Figure 7(a). The reason was that the mixture of N₂ and steam accelerated the process of heating, which was easier for N₂ and steam to migrate in the porous media resulting in migration distance increased. Finally, the mixed injection process promoted the horizontal expansion of the steam chamber.

Figure 8 shows the variation curves of characteristic parameters during CCS assisted by N₂. For the single injection process, the average oil production rate was 1.61ml/min and the cumulative oil-steam ratio reached 0.35. Also, the average oil production rate decreased to 1.32ml/min but was also high and the cumulative oil-steam ratio remained stable. The results indicated that single injection was more beneficial to the vertical expansion of the steam chamber and had a stronger effect on the drainage of N₂. Besides, mixed injection reduced the heat loss around the well and increased the lateral expansion distance and sweep area.

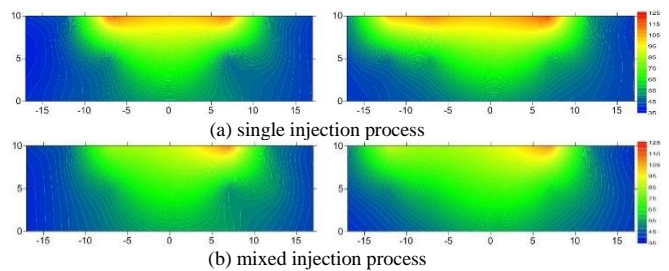
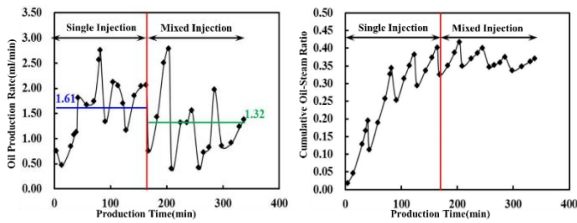


Figure 8. Vertical distribution of temperature at the end of CSS assisted by gas



(a) Oil production rate curve (b) Cumulative oil-steam ratio curve
Figure 9. Variation curves of characteristic parameters during CSS assisted by N₂ stage

(3) CSS Assisted by VR stage

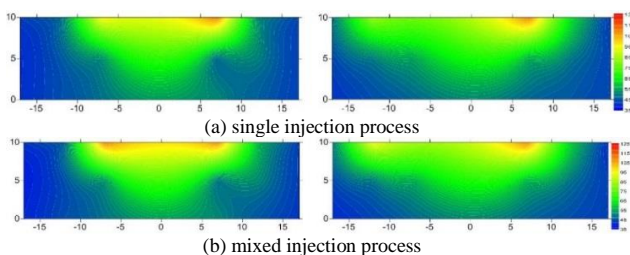
Single injection process: in this process, VR was injected before steam injection. At the end of single injection process, the final recovery reached 31.98% which was 5.13% higher than the process with gas stage. Figure 8(a) showed that, compared with the N₂ stage, the total sweep area decreased especially at the bottom and middle layers. The main reason was that the VR solution increased the water storage around the well and prevented the steam contacting with heavy oil directly which resulted in higher condensing rate of steam and heating loss.

Mixed injection process: in this process, the mixture of steam and VR was injected. As shown in Figure 10(b), the temperature of the top, middle and bottom layer were 69.6°C, 54.6°C and 44.8°C, respectively. The total average temperature and heating area were larger than that of single injection process which indicated the heating loss was lower than the single injection process.

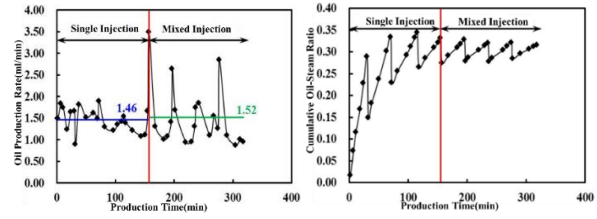
Figure 11 shows the variation curves of characteristic parameters during CCS assisted by VR. The oil rates of two injection patterns were 1.46ml/min and 1.52ml/min, respectively, both of which were higher than that of mixed injection of N₂-Steam. Meanwhile, the cumulative oil-steam ratio remained stable at 0.3. Under the combined effect of VR and high-temperature steam, the viscosity of extra-heavy oil was notably decreased leading to higher mobility. At the same time, the emulsification of VR was significant, which resulted in a higher oil production rate.

(4) CSS Assisted by Gas-VR co-injection stage

In this stage, the N₂-VR co-injection with steam was conducted.



(a) single injection process (b) mixed injection process
Figure 10. Vertical distribution of temperature at the end process of CSS assisted by VR



(a) Oil production rate curve (b) Cumulative oil-steam ratio curve
Figure 11. Variation curves of characteristic parameters during the process of CSS assisted by VR stage

The final recovery was 40.89%, increased by 4.29% over the last stage. According to Figure 12, the temperature of the top layer was lower than that of VR injection stage. In addition, the emulsion phenomenon was obvious in the photomicrograph of production liquid which illustrated the effect of VR still played a role. Also, the oil production rate and cumulative oil-steam ratio showed a stable trend, further explaining that more oil was produced under the combined effect of gas and VR even after many cycles.

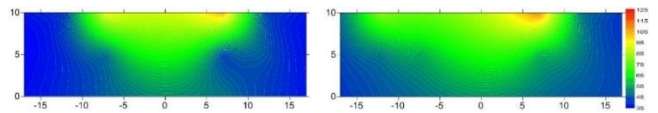
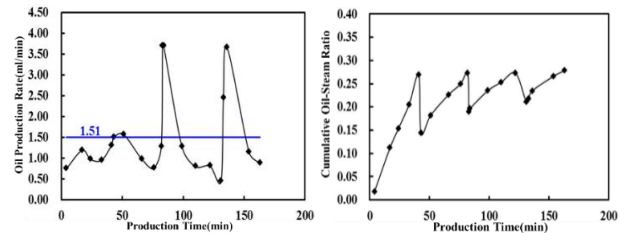


Figure 12 Vertical distribution of temperature at the end process of CSS assisted by Gas-VR co-injection stage



(a) Oil production rate curve (b) Cumulative oil-steam ratio curve
Figure 13. Variation curves of characteristic parameters during CSS assisted by Gas-VR co-injection stage

Figure 14 displays the variation curves of characteristic parameters of different liquid injection for Set 1. It can be seen that the additive of gas and VR can obviously increase the oil production rate. The oil recovery was improved significantly after the CSS process, the oil recovery of which was just 15.26%. The incremental oil recovery was 11.58%, 9.76%, 4.29% after gas injection, VR injection and gas-VR co-injection in turn and the final recovery was 40.89%. All of this shows that gas-VR co-injection not only inhibited steam overlapping, which promoted the horizontal expansion of the steam chamber but also reduced the viscosity of heavy oil significantly. More oil was produced due to the gas expansion energy.

3.2 Experimental Results of Set 2

CSS using horizontal well in ultra-heavy oil model

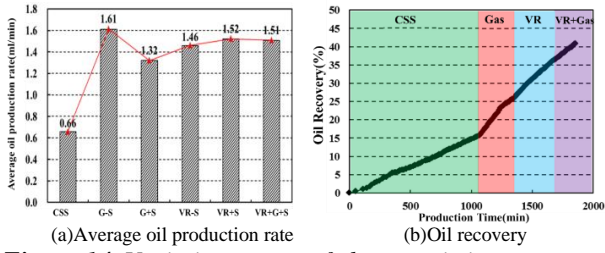


Figure 14. Variation curves of characteristic parameters for Set 1 process

were conducted in Set 2. The injection patterns were similar with Set 1. The details were as follows:

(1) CSS Stage

In this process, the final recovery of CSS was 17.28%. According to the plane and the vertical distribution of temperature, as shown in Figure 15 and 16, it can be seen that steam overlapping was serious, the temperature of the top layer was higher than that of the other two layers. Meanwhile, the shape of the temperature field was conical. The reason was that steam flow in the horizontal well was variable mass flow resulting in different injection rate in the different position of the horizontal well, and the heating loss was also different due to the long length of the well. The final results were displayed in the temperature field map. The sweep area of heel was higher than that of toe.

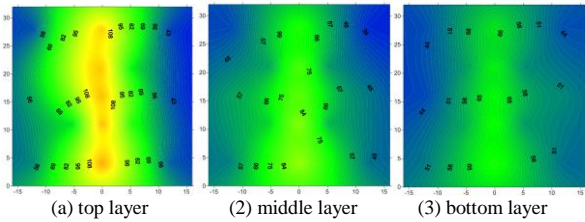


Figure 15. Plane distribution of temperature at the end process of CSS stage

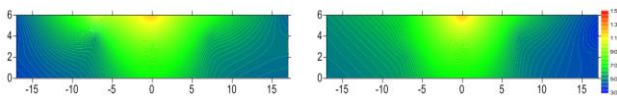


Figure 16. Vertical distribution of temperature at the end process of CSS stage

As shown in Figure 17, in the early stage of CSS, the thermal efficiency was high leading to a high oil production rate because of the low water storage near the well. At the end stage of CSS, the oil production rate and the cumulative oil-steam ratio decreased due to the low thermal efficiency.

(2) CSS Assisted by Gas Stage

Single injection process: The gas (N₂) was first injected before the steam injection. The total recovery at the end of the process was 27.49%, which increased by 10.21%.

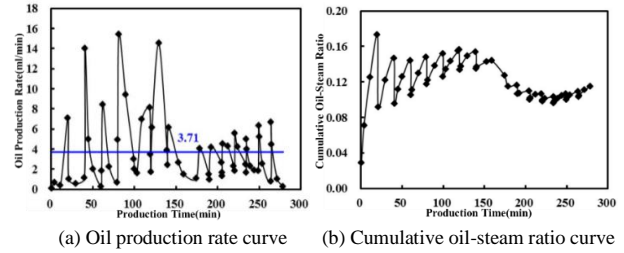


Figure 17. Variation curves of characteristic parameters during CSS stage in Set 2

The average pressure increased from 148kPa to 309kPa leading to the high steam injection pressure and thermal efficiency. N₂ gathering at the top layer pushed the steam down and improved the temperature of the middle and bottom layers. This scenario was more obvious at the beginning of the displacement.

Mixed injection process: The recovery was 37.87% which increased by 10.38% in this process. As shown in Figure 18(b), the heating area increased along the direction of the wings, especially for the bottom layer. The average temperature of the bottom layer in this process was 57.7°C which was 5.3°C higher than that in the single injection process.

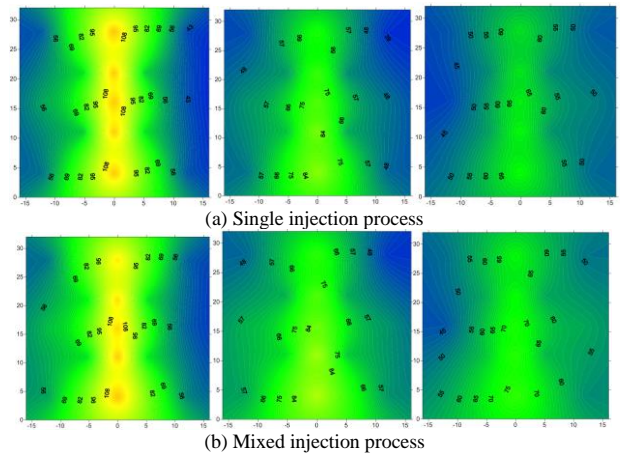


Figure 18. Plane distribution of temperature at the end process of CSS assisted by gas stage in Set 2

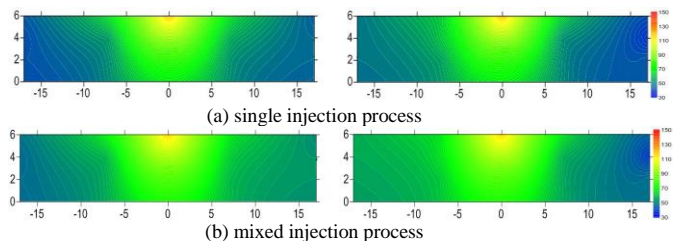


Figure 19. Vertical distribution of temperature at the end process of CSS assisted by gas stage in Set 2

And we can also see that the temperature difference between the heel and the toe became smaller and the heat distribution was more uniform. As shown in Figure 20, the average oil production rate for single injection process was 8.89ml/min, and it was

5.05ml/min for mixed injection process, both of which were higher than that of CSS process. The cumulative oil-steam ratio remained as 0.25 at the end of the stage. It demonstrated that the addition of nitrogen was an effective way to improve the energy of the reservoir and oil displacement, which was similar to the result of Set 1.

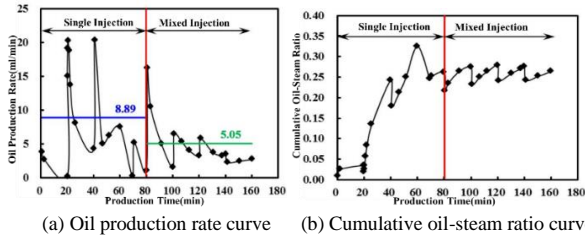


Figure 20. Variation curves of characteristic parameters during CSS assisted by gas stage in Set 2

(3) CSS Assisted by VR stage

Single injection process: VR was first injected before the steam injection. The recovery was 42.87%, which increased by 5.00% compared to the previous stage. As shown in Figure 21(a), compared with the previous stage of N_2 , the temperature and the steam chamber decreased. The reason is that the injection volume of VR was smaller than that of N_2 , so the pressurizing effect was not obvious. In addition, the water storage around the well increased leading to a higher heating loss. Thus, the thermal efficiency was affected.

Mixed injection process: the final recovery was 46.45% at the end of this process. Compared with the previous process, the average temperature of the top, middle and bottom layer were 67.6°C, 61.7°C and 58.2°C, respectively, which increased dramatically. It indicated that the mixed injection process reduced the heating loss. The horizontal expansion was more effective and uniform according to Figure 22. As shown in Figure 23, the oil production rate of single injection was 5.29ml/min, slightly higher than that of mixed injection. Considering the difference of heating area, it indicated that the degree of reaction between VR and heavy oil for single injection process increased, and it was important for the large water storage situation around the well after many cycles of CSS. In the mixed injection process, the sweep area did not increase but the oil production rate maintained as a high value which indicated that VR improved the displacement efficiency of near wellbore area.

(4) CSS Assisted by Gas-VR Co-injection Stage

In this process, N_2 , VR and steam were injected into the model simultaneously. At the end of the stage, the recovery was 59.29%, which increased

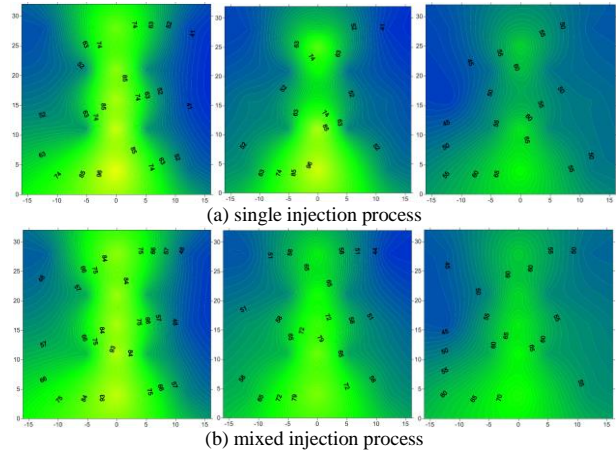


Figure 21. Plane distribution of temperature at the end process of CSS assisted by VR stage in Set 2

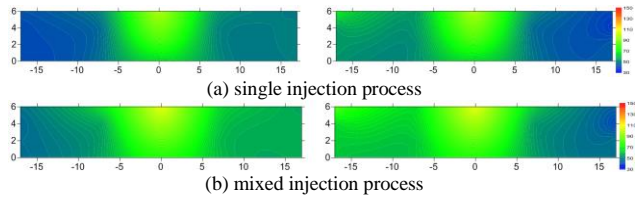


Figure 22. Vertical distribution of temperature at the end process of CSS assisted by VR stage in Set 2

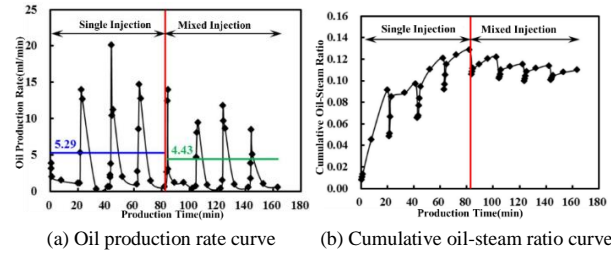


Figure 23. Variation curves of characteristic parameters during CSS assisted by VR stage in Set 2

by 9.42%. At the end of this process, according to the distribution of temperature, the average temperature was high and the sweep area expanded to the sides of the model. The conical shape caused by the heating loss and variable mass flow was not obvious, especially for the top and middle layers. This phenomenon was more clearly in the vertical distribution of temperature, as shown in Figure 25. It indicated that gas-VR co-injection inhibited steam overlap, promoting the horizontal expansion of the steam chamber, and reduced the viscosity of heavy oil significantly. The gas expansion pushed more oil out of the reservoir. Both the effect of VR and N_2 were fully-developed. Figure 26 shows the variation curves of characteristic parameters of different liquid injection for Set 2. It indicated the average oil production rate and oil recovery of different injection stage. It can be seen that the additive of gas can improve the oil production rate significantly which was contributed to the supplied-energy effect of the injection gas.

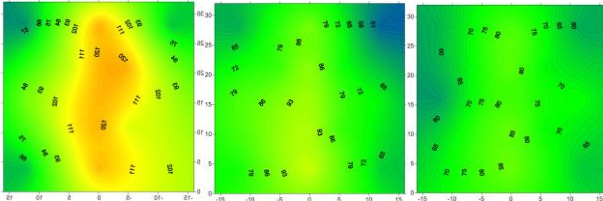


Figure 24. Plane distribution of temperature at the end process of CSS assisted by N₂-VR Co-injection stage in Set 2

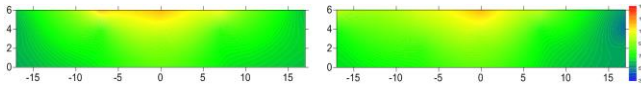


Figure 25. Vertical distribution of temperature at the end process of CSS assisted by N₂-VR Co-injection stage in Set 2

For the thin reservoirs of heavy oil with horizontal well, the horizontal expansion of the steam chamber was the main contradiction affecting the development effect. The added gas helped the horizontal expansion of steam. Based on the produced liquid, oil-in-water (O/W) emulsions generated under the combined-effect of gas and VR were more dispersive, compared with the single injection. According to Figure 26(b), the oil recovery of CSS was 17.28%, the incremental oil recoveries were 20.59%, 8.57%, 8.8% after gas injection, VR injection and gas-VR co-injection in turn above and the final recovery was 55.29%. The effects of the compound system still worked and increased the oil recovery after different injection patterns.

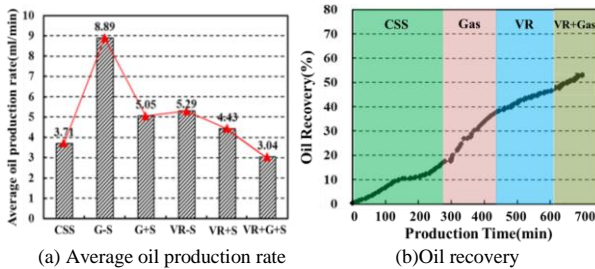


Figure 26. Variation curves of characteristic parameters for Set 1 process

4. Conclusions

A series of experiments were conducted to investigate the effect of gas and VR injected with steam during the CSS stage. The conclusions are as follows:

- The compressibility of nitrogen can improve the reservoir energy. Due to the gravity segregation, the nitrogen can occupy the upper section which inhibits the steam overlapping. Also, it can promote the vertical expansion of the steam chamber and increase the swept area.

- The injected VR solution can reduce the viscosity of heavy oil and change the scenario of the trapped oil near wellbore area especially. O/W emulsion is produced when the mobility gets stronger.
- It is proved that steam injection assisted by gas-VR is more beneficial to enhance the thermal recovery.
- Different injection orders have an impact on the recovery and sweep situation.

Acknowledgement

This work was financially supported by the National Science and Technology Major Project of China(2016ZX05031003004)

Nomenclature

- CSS cyclic steam simulation,
- EOR enhanced oil recovery,
- SOR steam-oil ratio,
- VR viscosity reducer,
- ISCO the type of pump used in the experiments.

References

- [1] C.A. Connally, Jr., J.E. Marberry. Steam Flood Pilot, Nacatoch Sand-Troy Field, Arkansas. SPE-4758-MS presented at Improved Oil Recovery Symposium of the Society of Petroleum Engineers of AIME: 22–24 April, (1974) Tulsa, Okla, USA. DOI: <http://dx.doi.org/10.2118/4758-MS>
- [2] Cai, Y. C., et al. A study on the technology of steam - hot water - nitrogen compound drive after steam channeling in steam flooding. Applied Mechanics & Materials, 316-317, 854-859. (2013) DOI: [10.4028/www.scientific.net/AMM.316-317.854](https://doi.org/10.4028/www.scientific.net/AMM.316-317.854).
- [3] Decker, A. M., & Flock, D. L. Thermal stability and application of emulsion composed blocking agents for steamflooding. Journal of Canadian Petroleum Technology, 27(4), 69-78.
- [4] Erincik, M. Z., Qi, P., Balhoff, M. T., & Pope, G. A. (2017, October 9). New Method to Reduce Residual Oil Saturation by Polymer Flooding. Society of Petroleum Engineers. DOI:10.2118/187230-MS
- [5] Gates, I. D., & Chakrabarty, N. Design of the steam and solvent injection strategy in expanding-solvent steam-assisted gravity drainage. Journal of Canadian Petroleum Technology, 47(9), (2008), 12-20. DOI: <https://doi.org/10.2118/08-09-12-CS>
- [6] Jha, K. N. (1986). A laboratory study of heavy oil recovery with carbon dioxide. Journal of Canadian Petroleum Technology, 25(2), 54-63. (1988) DOI: <https://doi.org/10.2118/SS-85-04>.
- [7] Liu, Q., Dong, M., & Ma, S. Alkaline surfactant flood potential in western Canadian heavy oil reservoirs. SPE/DOE Symposium on Improved Oil Recovery. (2006) DOI: <https://doi.org/10.2118/99791-MS>

- [8] Lu, C., Liu, H., Liu, Q., Lu, K., & Wang, L. Research on the Effect of Non-Condensable Gas and Viscosity Reducer for Better SAGD Performance. (2014) DOI: <https://doi.org/10.2118/170026-MS>.
- [9] Lu, C., Liu, H., & Zhao, W. Visualized study of displacement mechanisms by injecting viscosity reducer and non-condensable gas to assist steam injection. *Journal of the Energy Institute*, 90(1). (2015) DOI: <https://doi.org/10.1016/j.joei.2015.10.005>
- [10] Lu, C., Liu, H., Zhao, W., Lu, K., Liu, Y., & Tian, J., et al. Experimental investigation of in-situ emulsion formation to improve viscous-oil recovery in steam-injection process assisted by viscosity reducer. *Spe Journal*, 22(1). (2017) DOI: <https://doi.org/10.2118/181759-PA>.
- [11] Lyu, X., et al., "Visualized study of thermochemistry assisted steam flooding to improve oil recovery in heavy oil reservoir with glass micromodels." *Fuel* 218: 118-126. DOI: <https://doi.org/10.1016/j.fuel.2018.01.007>
- [12] Miller, J. S., & Jones, R. A. A Laboratory Study to Determine Physical Characteristics of Heavy Oil After CO₂ Saturation. SPE/DOE Enhanced Oil Recovery Symposium. Society of Petroleum Engineers. (1981) DOI: <https://doi.org/10.2118/9789-MS>
- [13] Pujol L and Boberg T C. Scaling accuracy of laboratory steam flooding models. Paper SPE 4191 Presented at the SPE California Regional Meeting, Bakersfield, California. (1972) DOI: <https://doi.org/10.2118/4191-MS>
- [14] Qi, P., Ehrenfried, D. H., Koh, H., & Balhoff, M. T. Reduction of Residual Oil Saturation in Sandstone Cores by Use of Viscoelastic Polymers. Society of Petroleum Engineers (2017). DOI:10.2118/179689-PA
- [15] Rojas, G. A. Dynamics of subcritical co₂/brine floods for heavy-oil recovery. *SPE Reservoir Engineering*, 3(1), (1988) 35-44. DOI: <https://doi.org/10.2118/13598-PA>.
- [16] S.R. Upreti, A. Lohi, R.A. Kapadia, et al., Vapor extraction of heavy oil and bitumen: a review, *Energy Fuels* 21 (3) (2007) 1562-1574. DOI: 10.1021/ef060341j
- [17] Wang, Y., Ge, J. J., Jiang, P., Zhang, G. C., & Du, Y. Mechanism and Feasibility Study of Nitrogen Assisted Cyclic Steam Stimulation for Ultra-Heavy Oil Reservoir. (2013) DOI: <https://doi.org/10.2118/165212-MS>
- [18] Zhang Xia, Zhang Xialin. Optimization Study of Production-Injection Ratio for Steam Flooding. IPTC-16458-MS presented at International Petroleum Technology Conference, (2013)26-28 March, Beijing, China. DOI: <http://dx.doi.org/10.2523/16458-MS>



Determination of The Cross Types to be used in a Trailer Chassis by Finite Element Method

Burak SEVIN^{1*}, Su Buse ŞAHİN²

¹ TIRSAN Solutions/P&D Low-Bed & Special Vehicles Business Unit, Sakarya, Turkey

² TIRSAN Solutions/P&D Tank & Silo Business Unit, Sakarya, Turkey

* Corresponding Author : burak.sevin@kaessbohrer.com

ORCID: 0000-0001-9048-1204

Article Info:

DOI: 10.22399/ijcesen.477613

Received : 1 November 2018

Accepted : 16 December 2018

Keywords

Trailer
Cross Member
Finite Element Method
FEA
Transportation

Abstract: Cargo transportation is done by airway, railway, maritime line and highway according to time and cost criteria. Trailers are widely used in highway transportation which is one of these cargo transportation types. Depending on the amount and variety of loads, the trailers vary among themselves. In addition to this diversity, it is desirable that a trailer should be lightweight and at the same time strong as far as transport safety and transport costs are concerned. When all these factors come together, serious research and development activities are required from the design stage to the final stage of manufacturing. One of the R&D phases is computer aided engineering analyzing. Without requiring material, labor and time, a design can be tested in virtual environment under certain boundary conditions before physical validation. Crosses, which are the one of the main carrier components in a trailer structure, between the longeron (main beam) and the frame, that exist perpendicular to these components, has been investigated in this study by taking into consideration of 1 g static loading, 0.8 g braking and torsion scenarios. In this study, the essential criteria are displacement and stress values of these crosses which have different geometries (cross-sections). Comparisons were made according to the results and in the light of these information, the finite element analysis results of the combination of the chosen crosses to be used in the production of the trailers were evaluated.

1. Introduction

In airway, railway, maritime line and highway transportation, highway transportation has a great importance in terms of its portion. According to Turkish Statistical Institute, 10% growth was achieved on the basis of exports realized in 2017 and the portion of highway transportation in this growth was 40%. Compared to the previous year, highway transportation increased by 7% [1].

When developing technologies and innovation initiatives of companies are taken into consideration, TIRSAN Solutions is a leading brand that gives direction to Europe and the world with its various products and transportation solutions. Under this great responsibility, products are produced according to the comfort, safety and cost criteria brought by transportation. Achieving these

criteria leads to serious R&D needs, and one of these needs is virtual tests which is known as simulations in other words, under the verification heading. Without requiring material, labor and time, a design can be tested in virtual environment under certain boundary conditions before physical validation.

Cross members, which are the one of the main carrier components in a trailer structure, between the longeron (main beam) and the frame, that exist perpendicular to these components, has been investigated in this study. The types of cross-sections examined are omega, reversed omega, box profile, C-type and reversed U-profile. Similar to this study, M. J. Akhtar, in his master's thesis named "Development of Guidelines for the Selection of Structural Profiles to Achieve Optimized Flooring Structure", examined the types

of cross members having different geometries [2]. These cross-sections were evaluated according to displacement and stress criteria and 1 g static loading, 0.8 g braking and torsion scenarios were applied [3]. In the braking scenario, certain calculations were made under the boundary conditions. During analyses, independent domains were used to ensure that the cross members did not affect each other and that an accurate assessment was made. Since cross-sections of these cross members are examined geometrically under certain loads and conditions, the thickness and length of these cross member types are the same. Comparisons were made according to the results and in the light of these information, the finite element analysis results of the combination of the chosen cross members to be used in the production of the trailers were evaluated via HyperWorks software [4].

2. Methodology

The method, Finite Element Analysis (FEA) which is developed by NASA, that helps to simulate mechanical components and systems to get information about failure, deformation and stresses under some various kind of loadings or conditions [5, 6, 8, 9]. In fact, the life determination of the structures after this method was also carried out by fatigue analysis [14].

In mechanics, the static state can be defined as the state of a system in equilibrium under balanced forces and torques. A static load can be defined as a load that does not vary. If there is a slow change in load, the system or structure can be solved by static analysis; however, if this load varies rapidly, the response of the structure must be defined by dynamic analysis [7]. On the other hand, if an analysis is static, it means that it does not depend on time. In this type of analysis, the term linearity includes small deformations, steady values or directions of loads and constraints, materials considered as elastic [5]. The solver computes the stiffness matrix for a linear static analysis by using Hooke's Law (Eq.1). For this equation, K , x and f indicates Global stiffness matrix, displacement and force respectively.

$$Kx = f \quad (1)$$

2.1 Definition of the Model

HyperMesh software is one of the best tools for creating high-quality mathematical models, although ANSYS, Abaqus, etc. softwares have their own pre-processing tools. In this study, HyperMesh

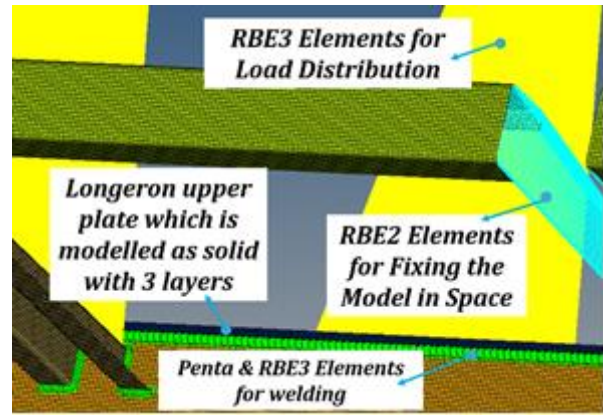


Figure 1. Element types in the Mathematical Model

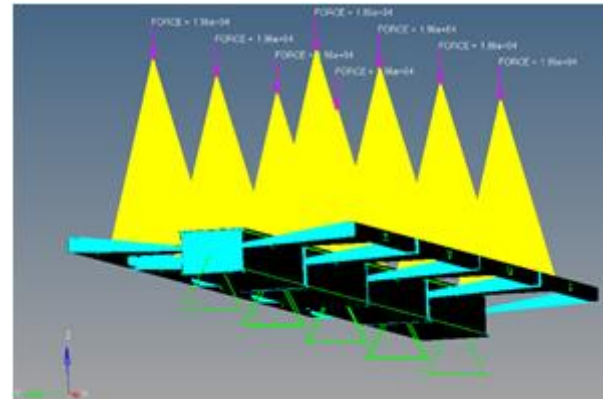


Figure 2. Capture of the Domain with Applied Forces

software was used as a pre-processing tool in constructing mathematical models [13]. Because of being in the same domain, for an independent comparison, cross members which have different cross-sections are located into frame and longeron parts separately. The average mesh size of the model is 5 mm and the components which have a thickness of 10 mm and above are modelled as solid and formed as 3 layers. Each cross member which is modelled as shell body has a thickness of 4 mm, same height of 60 mm and same length of 989 mm. Penta (mig) and RBE3 elements are used to model welding elements [10]. As a result of research on trailer platforms, a total of 40 tons cargo load can be carried by 20 cross members on average. So, each cross member has 2 tons of load on itself in this study. In the light of this information, forces at 19620 N are applied to each cross member via RBE3 elements. Load application points are 1600 mm above from the surface of the cross members. This 1600 mm measurement results from surveys and represents the average height of the center of gravity from ground of a caterpillar. The use of this height in the analysis is important for providing a moment load to the structures in the

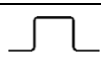



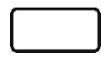
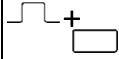
braking and torsion scenarios. The mathematical model of these structures and the definition of the domain are illustrated in Figures 1 and 2 as analysis captures.

Element types and numbers that are used in the mathematical model are also specified in Table 1 and Table 2.

Table 1. Mesh Element Types and Numbers According to Structures in the Model

Cross Member Types Used in Models	ELEMENT TYPES & NUMBERS					
	RBE2	RBE3	QUAD4	PENTA	HEX8	TOTAL
Omega	2	6113	132034	2017	287448	427614
Reversed Omega	2	6098	132034	2014	287448	427596
Box Profile	2	5654	133860	1870	279792	421178
C-Type	2	5456	116016	1800	271440	394714
Reversed U-Profile	3	5630	119580	1856	271440	398509
Combination	2	7992	181138	2624	287448	479204

Table 2. Section Views of Cross Members

Cross Member Types Used in Models	Section View	Cross Member Types Used in Models	Section View
Omega		C-Type	
Reversed Omega		Reversed U-Profile	
Box Profile		Combination	

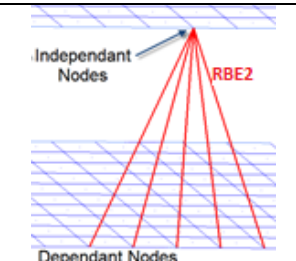
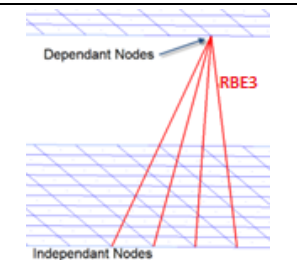
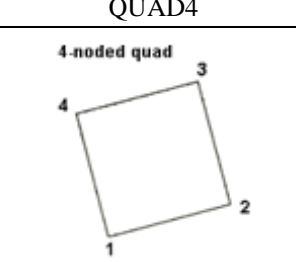
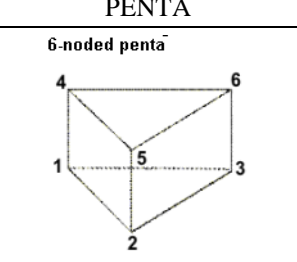
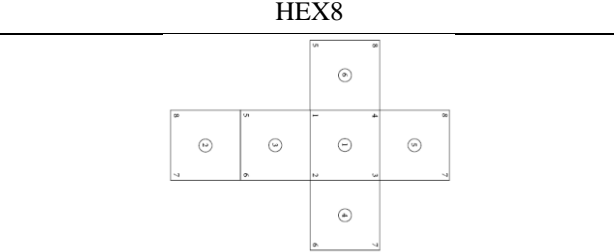
If the element types used in the mathematical model are defined, it can be specified that RBE2 and RBE3 are multi point constraint (MPC) rigid elements. A rigid element is used for node to node connection and it has infinite stiffness. It can transfer all the forces and moments that are acting on it. RBE2 Element has one independent node and multiple dependent nodes. On the other hand, RBE3 element has multiple independent nodes and a dependent node and also does not add any stiffness to the original structure. The most important difference between these two MPC rigid elements, RBE2 elements distribute the force and moment equally (homogeneously) and among all the connected nodes irrespective of position of force and moment application; whereas, RBE3 element is a constraint equation to distribute force and moment as per the distance [15, 16].

If the definition of element types is continued, the quad 4 elements used in the mathematical model, are 2D (1st order) quadrilateral elements with 4

nodes ordered in HyperMesh. There are two types of penta elements as penta6 and penta15, in which penta6 elements were used in this mathematical model. Penta6 elements are 3D (1st order) triangular prism pentahedra elements with 6 nodes ordered and Penta15 elements are 3D (2nd order) triangular prism pentahedra elements with 15 nodes ordered in HyperMesh. If it is defined where the penta elements (penta6) were used in this study, the welding elements (seam) used to connect components to each other, consist of penta6 and RBE3 elements. Finally, another element used in mathematical model is hex8 element that hex8 elements are 3D (1st order) hexahedra elements with 8 nodes ordered in HyperMesh [10].

Mentioned element types are shown in Table 3 with their visuals.

Table 3. Element Types with Their Visuals [10, 16]

Element Type	
	
	
	

2.2 Material Models

The material of entire components in the mathematical model is steel. MAT1 term as card image (supported card) is used for this material on HyperMesh Platform. Supported card MAT1 defines the material properties for linear, temperature-independent, isotropic materials. The

word “isotropic” consists of two words; these are “iso” and “tropic” which mean that “the same” and “directions” respectively. Properties of an isotropic material are independent from directions and axes. There are two independent constants that are modulus of elasticity (Young’s modulus) (E) and Poisson’s ratio (ν). It is valid for metals [11]. Properties of isotropic, orthotropic, anisotropic and laminates materials are specified in Table 4.

Table 4. Classification of Materials [11]

ISOTROPIC	<ul style="list-style-type: none"> • Iso: Same • Tropic: Directions • Properties independent of direction/axes • 2 Independent Constants (E, ν) • Metals
ORTHOTROPIC	<ul style="list-style-type: none"> • Ortho: Three • Tropic: Directions • Different properties along 3 axes • 9 independent constants • Wood, Concrete, rolled metals
ANISOTROPIC	<ul style="list-style-type: none"> • Different properties along crystallographic plane • 21 independent constants • All real life materials are anisotropic only but we simplify them into category of Isotropic and Orthotropic
LAMINATES	<ul style="list-style-type: none"> • Two or more materials bonded together in layers. • Simplest example is lamination carried out on certificates, Identity cards etc. • Mainly used for space applications and these days in automobiles the trend is shifting towards plastics and laminates from metals.

The properties of steel used in HyperMesh software is specified in the Table 5.

Table 5. Mechanical Properties of St52 Steel [12]

Material		St52 Steel
E (Young Modulus)	MPa	210000
ν (Poisson's ratio)	-	0.3
ρ (Material Density)	ton/mm ³	$7.9 \times 10^{(-9)}$
Yield Strength	MPa	355

2.3 Boundary Conditions

In the solution of a problem, the suitability of the boundary conditions is very important for the correct solution of the problem. At this point, the definitions that are verification and validation, come into play. To briefly describe these two concepts; verification can be specified as an analysis is performed correctly. On the other hand, verification can also be described as the process of checking that the software or method meets the specification. Validation is to check the results or to tend to a problem correctly [17].

As it is known, before the production of a design, service loads should be determined precisely. In the earlier stages of suspension and chassis designs, wheel loads were generally not obvious or attempted to be measured by prototypes. For this reason, instead of obtaining actual loads, the standard load scenarios which are very close to these loads are foreseen and started to be used. Manoeuvres determining these standard load scenarios, are assumed to be quasi-static and these loads are applied in the analysis scenarios in order to control the strength of the structure [18].

The 1 g static loading scenario is the most basic scenario that satisfies the expected reaction forces and shows the status of strength of the structure. In fact, it can be said that this scenario is a litmus-paper that shows the state of strength of the structure under a given payload or in unloaded condition.

When the sources related to load scenarios are examined, the acceleration value used for the braking scenario varies between 0.7 and 1 g for automotive industry [18]. For this study, 0.8 g acceleration is used for braking scenario and the force calculations that are explained in detail in the relevant section are made according to this value.

Separately from the aforementioned quasi-static cases, torsion scenarios are also applied to the structure. In general, 1 to 3 degree torsion simulations are performed for stiffness and strength controls of the trailer chassis. This scenario also shows not only the status of structures, but also the status of the welding elements that connect the structures to each other.

These scenarios were examined under three main headings for this study: 1 g static loading, 0.8 g braking and 3 degree torsion.

2.3.1 1 g Static Loading Scenario

Omega, reversed omega, box profile and C-type cross members are compared in this scenario. Frames and longerons are fixed for all translational and rotational DOFs at their edges. 1 g gravitational acceleration is applied to the entire domain. There

are two cross members for each structure at total as one for right and left side. The forces of 19620 N, corresponding to 2 tons, were applied to the crosses via RBE3 elements. Benchmark criteria are stress and displacement values.

2.3.2 0.8 g Braking Scenario

As an additional information, according to first analysis (1 g static loading) results, C-type cross member is eliminated and instead of it, reversed U-profile is examined. Hence, omega, reversed omega, box profile and reversed U-profile cross members are compared. Structures are fixed at all DOFs from the edge of frames. Structures extend through the x-coordinate in domain; so, one side of the longeron is fixed at other DOFs, except for the direction of braking. Translational DOF is free for this coordinate and from the opposite edge of longeron is pulled by calculated braking force (force application point is free for all DOFs). For the braking force, weights of groups which have four different cross member types were calculated via HyperMesh software. Total number of cross members for each group is 6 (3 for right-side and 3 for left-side) unlike models used in 1 g static loading scenario. Therefore, the total mass (M) for each group is calculated as Eq. 2:

$$M = (2 \text{ tons} \times 6 \text{ crosses}) + (m_{\text{model}}) \quad (2)$$

For the braking force, it can be calculated as Eq. 3:

$$F_{\text{Braking}} = 0.8 \text{ g} \times M \quad (3)$$

The forces for braking varies depending on the weight of each group. On the other hand, the gravitational acceleration is active.

The screenshot is shown in Figure 3, which describes the restriction of the structures to the specified degrees of freedom and the braking forces that are applied to each structure via RBE2 elements and calculated individually.

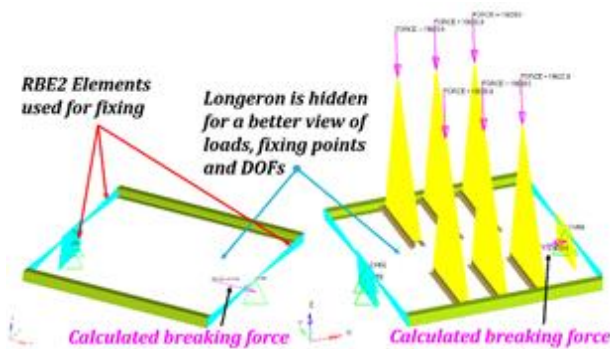


Figure 3. Constraints on DOFs and Applied Forces via RBE3 Elements

2.3.3 3 Degree Torsion Scenario

For each group of structures, all 6 DOFs are fixed but for one edge of structures the 4th DOF (rotational DOF @x coordinate) has a value of 3 degrees to perform torsional scenario. As in other scenarios, benchmark criteria are stress and displacement values. The screenshot of the torsion scenario is shown in Figure 4 with a 3-times deformation factor.

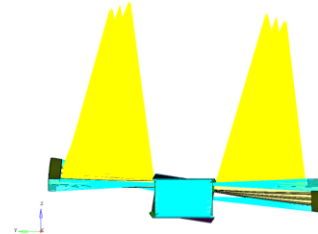


Figure 4. 3° Torsion Effect - 3x Deformation Factor

3. Linear Static Analysis Results

The screenshots of these three scenarios (HyperView) including the displacement and stress values are shown in Figure 5, 6, 7.1 and 7.2; and the values containing all these analysis results are examined in Table 6. The legend was set to 355 MPa as the yield stress value of St52 steel [12].

Table 6. Benchmark of the Cross Member Types According to Stress and Displacement Values

Cross Types	Analysis Scenarios	Max Stress [MPa] (On Welding Region)	Max Stress [MPa] (Except for Welding Region)	Max Displacement [mm]
Omega	Static 1g Loading	147.8	X	2.857
	Braking Effect	1226.3	649.2	14.707
	Torsion Effect	468	316	55.345
Reversed Omega	Static 1g Loading	236.9	X	3.909
	Braking Effect	1268.7	912.3	10.469
	Torsion Effect	573.3	429	55.458
Box Profile	Static 1g Loading	111.8	X	2.332
	Braking Effect	1788.2	380.4	10.616
	Torsion Effect	909.4	480	54.828
Reversed U-Profile	Static 1g Loading	X	X	X
	Braking Effect	1242.5	738.5	23.697
	Torsion Effect	609.5	408	57.431
C-Type Cross	Static 1g Loading	923	X	14.562

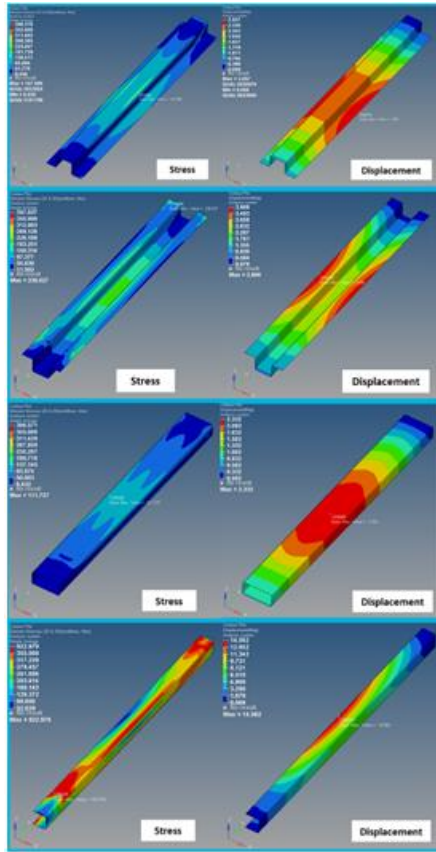


Figure 5. Results of 1 g Static Loading Scenario of the Cross Member Types

According to this benchmark, the best values and the obtained values that come after the best are indicated in this table. Considering these values, “the combination of omega and box profile cross member types” will be subjected to braking and torsion scenarios.

In consequence of braking scenario, the maximum stress value (on welding region), the maximum stress value except for welding region and the maximum displacement value are 1956.81 MPa, 575.74 MPa and 12.793 mm respectively for the combination and these are illustrated in Figure 8.

In consequence of 3° torsion scenario, the maximum stress value (on welding region), the maximum stress value except for welding region and the maximum displacement value are 930.27 MPa, 504.214 MPa and 55.171 mm respectively for the combination and these are illustrated in Figure 9.

4. Conclusion

The mathematical model formed from the combination of omega and box profile type cross members was subjected to braking and torsion scenarios.

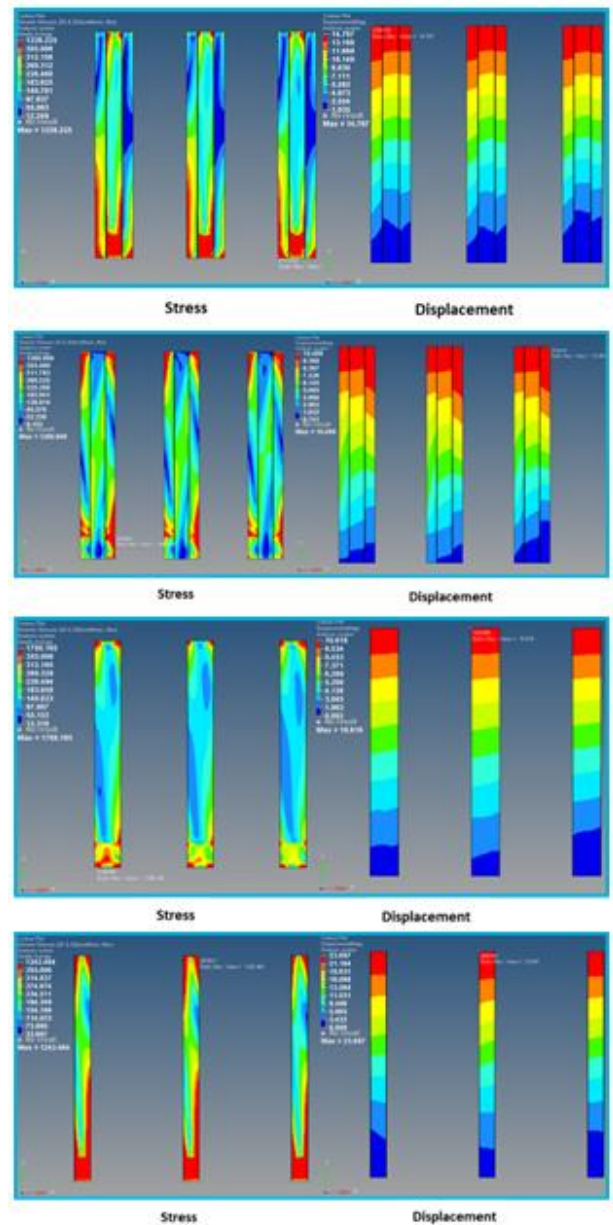


Figure 6. Results of 0.8 g Braking Scenario of the Cross Member Types

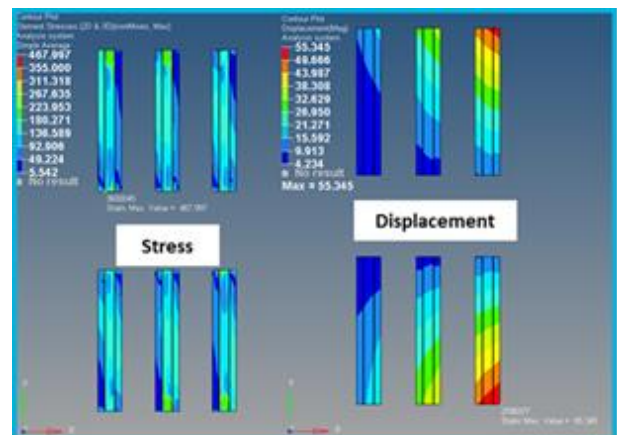


Figure 7.1. Results of 3° Torsion Scenario of the Cross Member Types

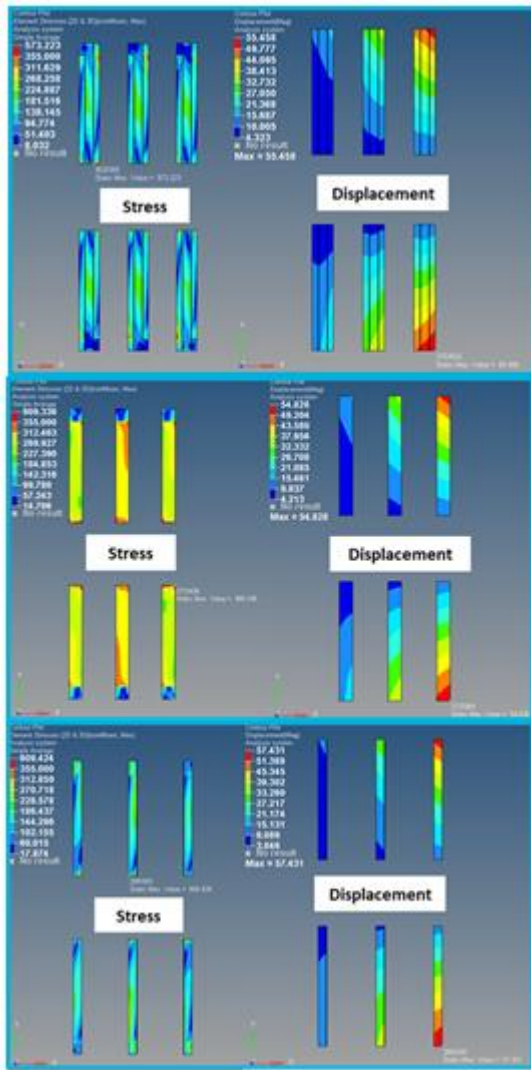


Figure 7.2. Results of 3° Torsion Scenario of the Cross Member Types

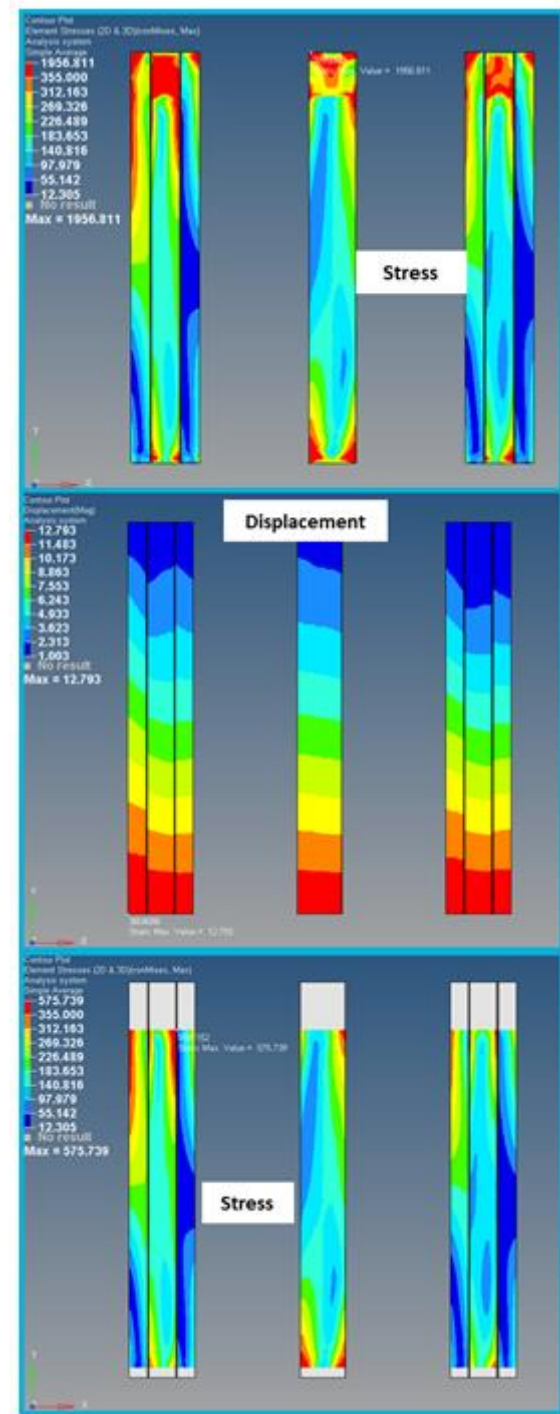


Figure 8. Results of 0.8 g Braking Scenario of the Combination

Table 7. Results of the Benchmark

Cross Types	Analysis Scenarios	Max Stress [MPa] (On Welding Region)	Max Stress [MPa] (Except for Welding Region)	Max Displacement [mm]
Omega	Static 1g Loading	147.8	X	2.857
	Braking Effect	* i 1226.3	* ii 649.2	* iv 14.707
	Torsion Effect	* i 468	* iii 316	* iv 55.345
Box Profile	Static 1g Loading	111.8	X	2.332
	Braking Effect	* i 1788.2	380.4	10.616
	Torsion Effect	* i 909.4	* iii 480	54.828
Combination	Static 1g Loading	* v N/A	* v N/A	* v N/A
	Braking Effect	* i 1956.9	* ii 575.8	* iv 12.793
	Torsion Effect	* i 930.3	* iii 504.3	* iv 55.171

In this study, the maximum stress and displacement values on the regions where belong to components and near the welding elements were investigated. Finally, in the generated table (Table 7), models constructed from only omega type cross members and only box-profile type cross members were compared with this combination mathematical model separately.

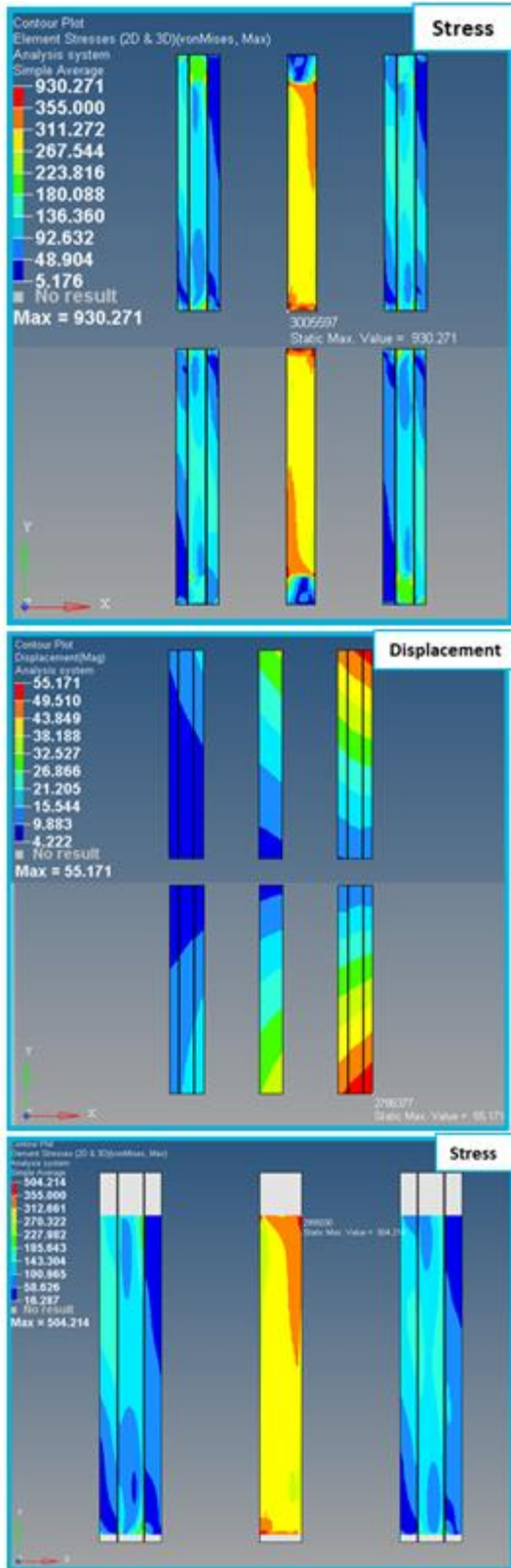


Figure 9. Results of 3° Torsion Scenario of the Combination

When the results on Table 7 are examined for the combination model:

- i. Maximum stress values on welding regions are increased for both braking and torsion scenarios.

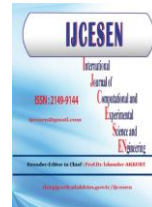
- ii. On regions where the welding zone is not included, the stress value in the braking scenario is reduced in comparison to when the omega type cross member is used alone.
- iii. Increment of stress values is observed in the torsion scenario in comparison to both omega and box-profile type cross members.
- iv. According to the braking and torsion scenarios, the displacement values are decreased in compliance with the model in which omega is used alone.
- v. Abbreviation of “Not available (N/A)” term in Table 7 means that 1g static loading scenario is not performed for the combination of cross member types. When the static loading scenarios of 1g were examined, the stress values that obtained were below the yield stress value of St52 steel which is the material of the components. Thus, the braking and torsion scenarios are used for decision.

The mass of the omega type cross member and box-profile type cross member in the mathematical model were measured as 8.55 kg and 10.26 kg, respectively. The models where box profile type cross members are used provide the best results; however, when the entire trailer chassis is constructed by using only this cross member type, approximately it will bring an extra 20% weight to the structure instead of the omega type cross member is used alone. Lightness is an important criterion for the construction of trailer bodies, it is a heavy solution to use only box profiles based on this results. Thus, to be competitive and to achieve optimum weight on the chassis, using both omega and box profile type as a combination is a logical solution.

References

- [1] Uluslararası Nakliyeciler Derneği, Statistics (30.10.2018), <https://www.und.org.tr/tr/19744/Istatistikler>
- [2] Akhtar, M. J. (2017), Master Thesis, Aalto University, Development of Guidelines for the Selection of Structural Profiles to Achieve Optimized Flooring Structure.
- [3] Shinde, D., Kalita, K., “FE Analysis of Knuckle Joint Pin Used in Tractor Trailer.” ARPN Journal of Engineering and Applied Sciences 10 (2015) 2227-2232.
- [4] Sane, S.S., Jadhav, G., Anandaraj, H., “Stress Analysis of Light Commercial Vehicle Chassis by FEM”, Piaggio Vehicle Pvt. Ltd, Pune, India (1955).

- [5] FEA for All, Linear Static Analysis (18.10.2018), <http://feaforall.com/linear-static-analysis-fea/>
- [6] Esener, E., Ercan, S., Firat, M., “Determination of the Fatigue Behavior of a Wheel Rim Using Finite Element Analysis”, 4th Int. Conf. on Comp. and Exp. Scien. and Eng. (ICCESEN-2017) , Antalya-Turkey pp. 617-619 (2017) DOI: 10.12693/APhysPolA.132.617
- [7] Altair OptiStruct Linear Analysis 13.0 Manual
- [8] Karaçalı, Ö., “Computational Material Analysis of Structural and Hemodynamic Model of Coronary Stent by CFD/FEA in Computer Aided Mechanical Engineering Approach”, 3rd Int. Conf. on Comp. and Exp. Scien. and Eng. (ICCESEN-2016) Antalya-Turkey pp. 249-251(2016). DOI: 10.12693/APhysPolA.130.249
- [9] Karaçalı, Ö., “Computational Engineering Analysis of Low-Cycle Loading for AMF-Active Micro Forceps 316 L-Stainless Steel Material by Finite Element Method”, 2nd Int. Conf. on Comp. and Exp. Scien. and Eng. (ICCESEN-2015) Antalya-Turkey pp.B-40-42 (2015). DOI:10.12693/APhysPolA.128.B-40
- [10] Altair HyperWorks 14.0 Manual
- [11] Altair University, Material and Property Information (28.10.2018), <http://altairuniversity.com/wp-content/uploads/2014/02/matprop1.pdf>
- [12] TS 2162 EN 10025, Table 5, Turkish Standards Institution, 1996
- [13] Özer, H., Can, Y., Yazıcı, M., “Investigation of the Crash Boxes Light Weighting with Syntactic Foams by the Finite Element Analysis”, 4th Int. Conf. on Comp. and Exp. Scien. and Eng. (ICCESEN-2017) , Antalya-Turkey pp. 734-737 (2017). DOI: 10.12693/APhysPolA.132.734
- [14] Özsoy M., Pehlivan K., Firat M., Özsoy N., Uçar V., “Structural Strength and Fatigue Life Calculation of Y32 Bogie Frame by Finite Element Method”, 2nd Int. Conf. on Comp. and Exp. Scien. and Eng. (ICCESEN-2015) Antalya-Turkey pp.B-327-329 (2015). B-327-329. DOI: 10.12693/APhysPolA.128.B-327
- [15] RBE2 vs RBE3 vs RBOBY (12.11.2018), <https://forum.altair.com/topic/18187-rbe2-vs-rbe3-vs-rbody/>
- [16] Altair University, 1D Elements and Connectors (12.11.2018), https://altairuniversity.com/wp-content/uploads/2012/04/HM_1D_Extract.pdf
- [17] CAE ASSOCIATES, Engineering Advantage, Is Your FEA Process Verified and Validated? (14.11.2018), <https://caeai.com/blog/your-fea-process-verified-validated>
- [18] Heißing, B., Ersoy M., Chassis Handbook, Springer Fachmedien Wiesbaden GmbH (2011), pp. 467-468



Utilization of Marble and Boron Waste in Brick Products

Atilla EVCİN^{1*}, Bahri ERSOY², Hakan ÇİFTÇİ²

¹ Afyon Kocatepe University, Department of Material Science and Engineering, , 03200, Afyonkarahisar, Turkey

² Afyon Kocatepe University, Department of Mining Engineering, 03200, Afyonkarahisar, Turkey

* Corresponding Author : evcin@aku.edu.tr

ORCID: 0000-0002-0163-5097

Article Info:

DOI: 10.22399/ijcesen.480487

Received : 08 November 2018

Accepted : 27 December 2018

Keywords

Marble waste
Boron waste
Brick
Characterization

Abstract:

In this study, usability of marble and boron wastes as alternative raw materials in the production of bricks was investigated. They were used in different ratios to prepare samples. Marble waste in concentrations of 5, 10, 15 and 20 wt% were added to the boron waste. Afyon brick clay was used as a binder in 10 wt%. Specimens were shaped by hydraulic press and fired at temperatures from 850 to 1050 °C for 4 hours. The crystalline structure and morphologies of the samples are characterized by X-ray powder diffractometer (XRD) and scanning electron microscopy (SEM), respectively. Flexural strengths of samples were measured. Acceptable mechanical properties have been obtained from the brick sample containing 5 wt% marble waste, 85 wt% boron waste and 10 wt% clay sintered at 1050 °C for 4 hours.

1. Introduction

Marble and boron wastes are one of the major environmental problems in Turkey. Only in Afyon province, disposed waste marble material is about 12 million tones/year and amount of boron waste resulting from the boron plants in Turkey is more than one million tone in a year[1-2]. There is an urgent demand to manage it in order to reduce the environmental impact. Large areas have to be allocated for disposal of them. Thus, waste storage causes environmental pollution and economical loss [3-5]. There are many studies on the use of marble and boron wastes as additive or filling materials in various applications such as ceramic [6-8], concrete [9-10], brick [11], and building materials [12].

In this study boron and marble wastes were evaluated in brick product. They were mixed in different proportions and shaped by hydraulic press. Then they were characterized by mechanic test, X-ray diffraction (XRD), scanning electron microscopy (SEM).

2. Materials and Method

Marble waste was supplied from Reis Marble Factory in Afyon. Boron waste was kindly supplied from Eti Maden Emet Boric Acid Factory in Emet, Kütahya. Marble and boron wastes were dried in oven at 100 °C, then ground in jet mill under the size of 250 µm. In order to prepare brick samples powdered marble waste, powdered boron waste and Afyon brick clay as a binder were mixed in the compositions as given in Table 1. They were shaped by hydraulic press under 100 bar and fired at temperatures from 850 to 1050 °C for 4 hours. The crystalline structure and morphologies of the brick samples were characterized by X-ray powder diffractometer (XRD) and scanning electron microscopy (SEM).

Table 1. Materials ratios in brick mixtures

Samples	Boron waste, wt %	Marble waste, wt%	Clay, wt %
BM1	90	-	10
BM2	85	5	10
BM3	80	10	10
BM4	75	15	10
BM5	70	20	10

Table 2. Chemical analysis of boron and marble wastes.

Boron waste	Component	CaO	SiO ₂	MgO	Al ₂ O ₃	Fe ₂ O ₃	K ₂ O	SO ₃	Cr ₂ O ₃	SrO	B ₂ O ₃	LOI
	Wt (%)	36.7	9.96	2.33	1.66	2.64	0.92	20.5	1.24	2.27	1.21	19.5
Marble waste	Component	CaO	SiO ₂	MgO	Al ₂ O ₃	Fe ₂ O ₃	K ₂ O	-	-	-	-	LOI
	Wt (%)	54.30	0.75	0.22	1.15	0.20	0.23	-	-	-	-	43.20

3. Results and Discussion

The best sintered samples at each temperature and mechanical strengths of fired samples in each composition were given in Fig. 1 and Fig. 2, respectively. As clearly seen from Fig. 2, the flexural strength of brick decreases linearly with increase of marble waste addition. The maximum strength was obtained with BM1 sample. However, the bricks having BM2 composition gave the reasonable strength values. Considering the reusing of the marble waste in addition to the boron waste, the BM2 brick mixing was preferred as suitable

composition. The figures also show that the best temperature for sintering is 1050 °C for the bricks. SEM images (Fig. 3) and XRD analysis (Fig.4) support this case. At 850 °C, sintering is very poor and a heterogeneous structure with high porosity is seen. However, at 1050 °C, some hydrated calcium sulphates in boron waste reacts with clay minerals and also CaO resulting from the thermal decomposition of marble waste in order to form akermanite mineral a kind of spinel phase. So that, the microstructure of the brick became more compact and homogeneous by means of solid-state sintering mechanism (Fig. 3).

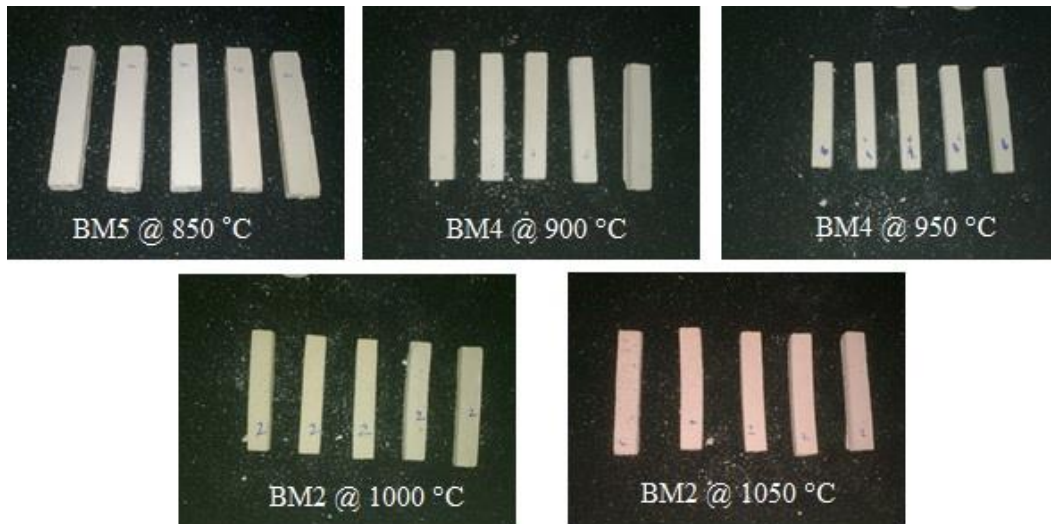


Figure 1. The best fired samples at different temperatures.

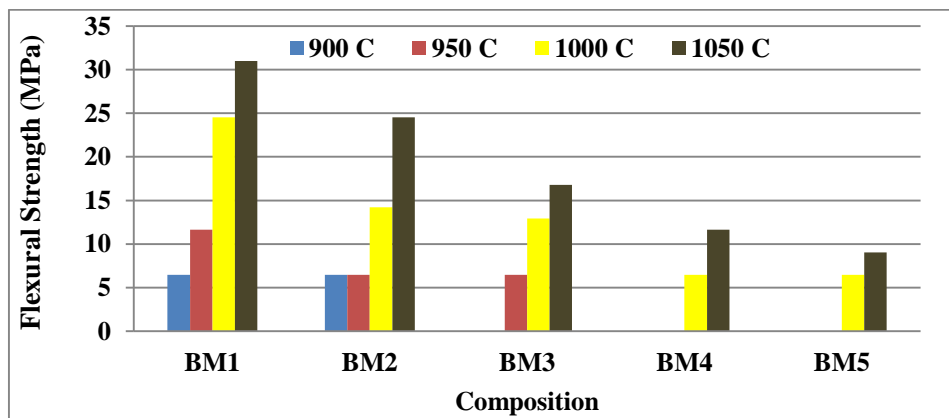


Figure 2. Flexural strengths of samples fired at different temperatures.

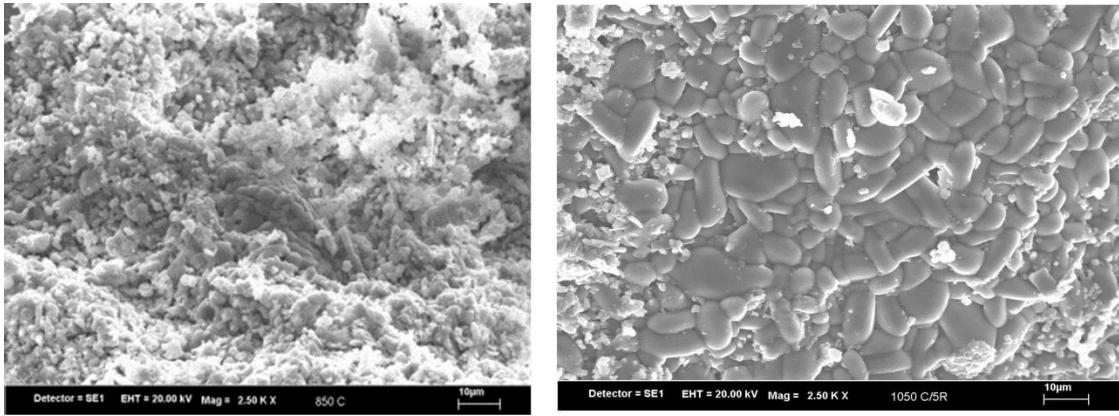


Figure 3. SEM images taken from the fracture surface of sintered BM2 samples at 850 (left) and 1050 oC (right).

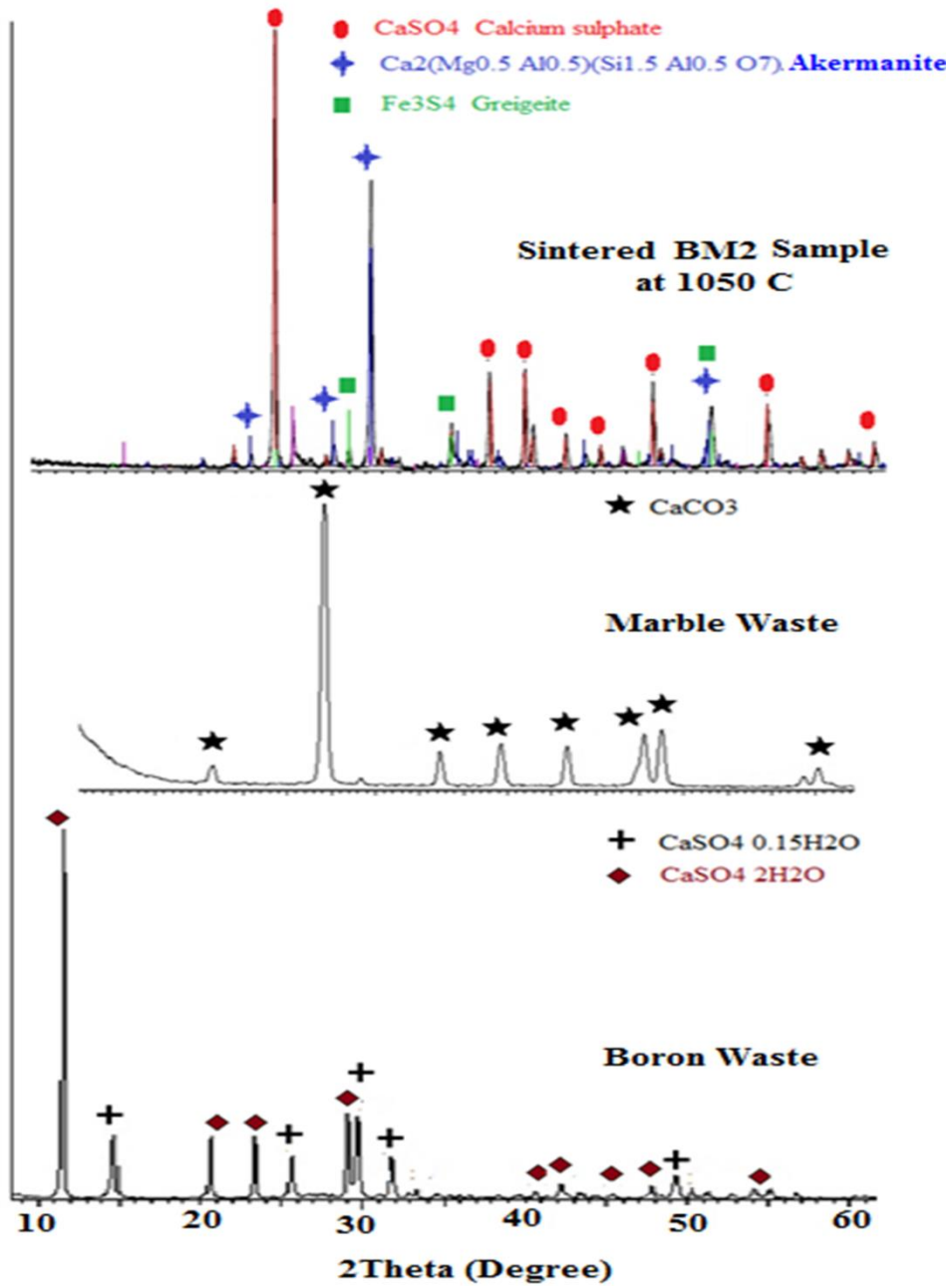


Figure 4. XRD pattern of raw materials and sintered BM2 sample.

4. Conclusion

Considering utilization of both of the boron and marble wastes the best flexural strength (~25 Mpa) value has been obtained from the brick sample containing 5 wt% marble waste, 85 wt% boron waste and 10 wt% clay sintered at 1050 °C for 4 hours. More than 5wt% marble waste addition into brick composition decreases the flexural strength of the brick significantly.

References

- [1] Ersoy, B., Sayın, Z. E., Arsoy, Z., Sayın Ü., Unaware of our underutilized resource:natural stone open pit and factory wastes, *Mine/Pit Technologies*, 27, (2015) 92- 100.
- [2] L. Koroglu, E. Butev, Z. Esen, E. Ayas, A novel approach for synthesis of monticellite based bioactive ceramic powders from boron derivative wastes, *Materials Letters*, Volume 209, (2017) 315-318. DOI: 10.1016/j.matlet.2017.08.034
- [3] Ismail Sedat Buyuksagis, Tayfun Uygunoğlu, Ertunc Tatar, Investigation on the usage of waste marble powder in cement-based adhesive mortar, *Construction and Building Materials*, Volume 154 (2017) 734-742 DOI: 10.1016/j.conbuildmat.2017.08.014
- [4] H. Hebhoub, H. Aoun, M. Belachia, H. Houari, E. Ghorbel, Use of waste marble aggregates in concrete, *Construction and Building Materials*, Volume 25, Issue 3 (2011) 1167-1171. DOI: 10.1016/j.conbuildmat.2010.09.037.
- [5] S. Özavcı and B. Çetin, Radiation Shielding Properties of Mortars and Plasters Used in Historical Buildings, *Acta Physica Polonica A*, Vol. 132 (2017) 986-987. DOI: 10.12693/APhysPolA.132.986
- [6] Selvin Yeşilay, Münevver Çakı, Hakan Ergun, Usage of marble wastes in traditional artistic stoneware clay body, *Ceramics International*, Volume 43, Issue 12 (2017) 8912-8921. DOI: 10.1016/j.ceramint.2017.04.028
- [7] Bugra Cicek, Emirhan Karadagli, Fatma Duman, Valorisation of boron mining wastes in the production of wall and floor tiles, *Construction and Building Materials*, Volume 179 (2018) 232-244. DOI: 10.1016/j.conbuildmat.2018.05.182
- [8] İ. Özkan, Utilization of Bigadiç Boron Works Waste Clay in Wall Tile Production, *Acta Physica Polonica A*, Vol. 132 (2017) 427-429 DOI: 10.12693/APhysPolA.132.427
- [9] Hasan Şahan Arel, Recyclability of waste marble in concrete production, *Journal of Cleaner Production*, Volume 131 (2016) 179-188. DOI: 10.1016/j.jclepro.2016.05.052.
- [10] Tayfun Uygunoğlu, İlker Bekir Topçu, Atilla Gürhan Çelik, Use of waste marble and recycled aggregates in self-compacting concrete for environmental sustainability, *Journal of Cleaner Production*, Volume 84 (2014) 691-700. DOI: 10.1016/j.jclepro.2014.06.019.
- [11] Yüksel Abalı, Mehmet Ali Yurdusev, M. Sadrettin Zeybek, Ahmet Ali Kumanlıoğlu, Using phosphogypsum and boron concentrator wastes in light brick production, *Construction and Building Materials*, Volume 21, Issue 1 (2007) 52-56. DOI: 10.1016/j.conbuildmat.2005.07.009.
- [12] Sarkar R, Das SK, Mandal PK, Maiti HS. Phase and microstructure evolution during hydrothermal solidification of clay-quartz mixture with natural stone dust source of reactive lime. *J Eur Ceram Soc* 26 (2006) 297–304.



Clustering of European Countries in terms of Healthcare Indicators

Billur ECER¹, Ahmet AKTAS^{2*}

¹ Ankara Yıldırım Beyazıt University Industrial Engineering Department, Ankara, Turkey

² Gazi University Industrial Engineering Department, Ankara, Turkey

* Corresponding Author : aaktas@gazi.edu.tr

ORCID: 0000-0002-4394-121X

Article Info:

DOI: 10.22399/ijcesen.416611

Received : 18 April 2018

Accepted : 20 January 2019

Keywords

Data mining

Clustering

Healthcare indicators

EU countries

Abstract:

Health is always considered as one of the most important issues related to human being. Due to this importance, governments should primarily provide the best healthcare services to their citizens. Some indicators can show the quality of healthcare services in the country. However, one country can have a higher value of one indicator and can have a lower value of another. Thus, countries can be categorized in terms of quality of healthcare services. Clustering is a useful tool for comparing countries and defining the similar countries in terms of healthcare services. In this study, 28 European Union (EU) countries were evaluated on 14 health factors and the number of clusters was determined by the generally accepted rule of thumb. To cluster countries, k-means clustering method is run in WEKA software for two cluster numbers and four different initial solution approaches. The resulting clusters were evaluated according to the Spearman rank correlation coefficient using the order of the GDP per capita values of the countries in each cluster. It seems using four clusters with Canopy initial solution approach is the most appropriate way of clustering.

1. Introduction

There are national and international health organizations working on prevention and treatment for diseases at national and international level. Apart from these, countries are also obliged to provide their citizens health services in the best possible way. Health care is important among the basic needs. It is possible to compare the level of development with the current situation in terms of health services.

In Table 1, a summary of literature for data mining studies about health subject is presented. For this reason, in this study, European Union member countries are clustered by the k-means method considering healthcare indicators. The rest of the paper organized as follows. The application of clustering with k-means method is given in the second section. The paper concluded with presenting clustering comparisons of countries and suggestions for future works in the third part.

2. Clustering of EU Countries via K – Means Algorithm

K – means clustering algorithm is developed by MacQueen in 1967 [1]. This method allows each unit to belong to only one cluster. With the K-means method, each element is assigned to the cluster that has the closest cluster center to itself. The average of values related to all elements in the cluster is the cluster center. K-means method assumes that the center point represents the cluster. The aim is to determine k clusters of elements with the least squared center distance for each cluster. In the K-means method, k-number of clusters is determined, and then clustering is performed considering distance criteria for clusters depending on the number of clusters. The disadvantage of the method is that it is difficult to determine the number of k sets. To overcome this difficulty, rule of thumb for determining cluster number k is

Table 1. Literature summary for data mining studies in healthcare.

Author	Year	Subject	Method
Ersöz [2]	2008	Evaluation of countries	Multi-dimensional scaling
Lorcu et al. [3]	2012	Evaluation of countries	Multi-dimensional scaling, hierarchical clustering
Alptekin [4]	2014	Evaluation of countries	Fuzzy clustering
Lewandowski et al. [5]	2014	Psychiatric diseases	K-means, Ward method
Moser et al. [6]	2014	Heart diseases	Hierarchical clustering, Ward method
Tsumotoa vd. [7]	2015	Nursing	Dual clustering
Olson et al. [8]	2016	Old patients	Hierarchical mass clustering, failure discovery rate

approximately calculated by the following formula [9] where k is the number of clusters, and n is the sample size:

$$k \approx \sqrt{\frac{n}{2}} \quad (1)$$

In the study, clustering of the European Union member countries in terms of health factors is done with Weka software by the k-means method. A data set consisting of the mean values of the last 20 years of the values of 14 variables listed below related to health factors of 28 EU countries is used [10]. The data set used is derived from the World Bank World Development Indicators database. There is no lost value. The following variables are considered:

- Health expenditure per capita (US \$)
- Hospital beds (per 1000 people)
- Immunization, Diphtheria Whooping cough Tetanus (% of children aged 12-23 months)
- Immunization, Measles (% of children aged 12-23 months)
- Life expectancy at birth (year)
- Risk of maternal mortality (%)
- Number of deaths under the age of five

- Number of surgical procedures (per 100,000 population)
- Prevalence of anemia among children (% of children under 5)
- Prevalence of anemia in non-pregnant women (% of women aged 15-49)
- Prevalence of anemia in pregnant women (%)
- Prevalence of anemia in women of reproductive age (% of women aged 15-49)

Table 2. Obtained clusters for trials.

Country	3 Clusters				4 Clusters			
	Random	K-Means++	Canopy	Farthest first	Random	K-Means++	Canopy	Farthest first
Germany	1	1	1	1	1	1	4	1
Austria	1 *	2 *	1 *	3 *	1 *	2 *	1 *	3 *
Belgium	1	2	1	1 *	1	2	1	1 *
Bulgaria	3 *	3 *	2 *	2 *	3 *	3 *	2 *	4 *
Czech Republic	3	3	2	2	3	3	2	4
Denmark	1	2	1	1	1	2	1	1
Estonia	3	3	2	2	4 *	3	2	4
Finland	1	1 *	1	1	1	1 *	1	1
France	1	1	1	1	1	1	4 *	1
Croatia	2	3	2	2	2	3	2	4
Netherlands	1	2	1	1	1	2	1	1
England	1	2	1	1	1	2	1	1
Ireland	1	2	1	3	1	2	1	3
Spain	1	2	1	1	1	2	1	1
Sweden	1	2	1	1	1	2	1	1
Italy	1	2	1	1	1	2	1	1
Cyprus	2 *	3	3	1	2 *	3	3 *	1
Latvia	3	3	2	2	4	3	2	2 *
Lithuania	3	3	2	2	4	3	2	4
Luxemburg	1	1	1	1	1	1	1	1
Hungary	3	3	2	2	3	4 *	2	4
Malta	1	2	1	3	1	2	1	3
Poland	3	3	2	2	3	4	2	4
Portugal	1	2	1	1	1	2	1	1
Romania	3	3	2	2	4	4	2	2
Slovakia	3	3	2	2	3	3	2	4
Slovenia	2	3	3	2	2	3	3	4
Greece	1	2	1	1	1	2	1	1

- The surviving woman until the age of 65 (% in the community)
- Male surviving until age 65 (% in community)

To create clusters, Simple K-Means method is used. The Weka program uses four different initial clustering approaches to start clustering in the K-means method. These approaches are defined as Random, K-Means ++, Canopy and Farthest First. In order to determine the number of clusters K, the rule of thumb is applied equal to 28. In this case, k is approximately equal to 3.741. Using the 4 different approaches mentioned above for the K-means methods, the results for 3 and 4 cluster formation situations are evaluated. Obtained clusters in that trials are given in Table 2. The optimal clustering should be determined by considering the effect of the different initial methods used on clustering results. The groups obtained by 4 different methods and 2 cluster numbers are evaluated by using the Spearman Rank Correlation Coefficient given in Equation (2).

$$\rho = 1 - \frac{6 \sum d_i^2}{n(n^2 - 1)} \quad (2)$$

The evaluation of the clusters is done by using the rank of GDP per capita in the corresponding countries. Average GDP values and country ranks are presented in Table 3. Taking these sequence numbers into account, the Spearman rank correlation coefficient obtained for each clustering experiment is given in Table 4.

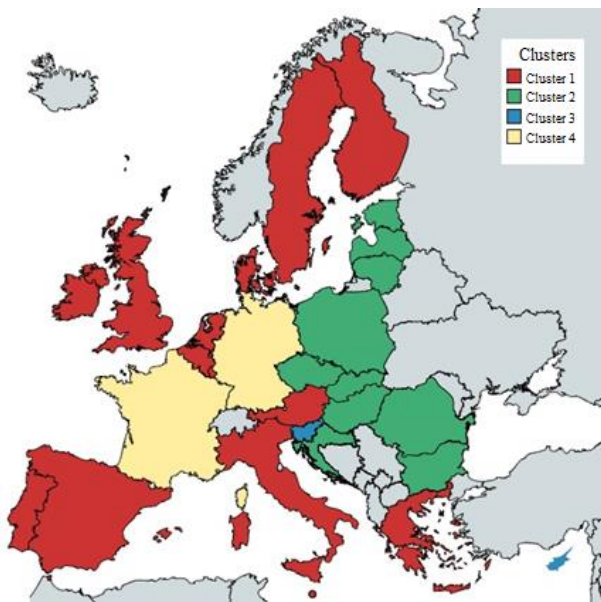


Figure 1. Representation of clusters on the European map.

Table 3. GDP values and ranks of countries.

Country	Average GDP	Rank
Germany	35470.5	10
Austria	37934.8	7
Belgium	36000.8	9
Bulgaria	3825.43	28
Czech Republic	12921.9	19
Denmark	46984.3	2
Estonia	9447.16	23
Finland	37107.2	8
France	34133.3	11
Croatia	9625.45	22
Netherlands	41110.9	5
England	38068.2	6
Ireland	46127	3
Spain	25092.3	13
Sweden	41478.5	4
Italy	30745	12
Cyprus	23183	14
Latvia	6964.52	26
Lithuania	7610.89	25
Luxemburg	76462.3	1
Hungary	10288.6	21
Malta	14969.4	18
Poland	8336.02	24
Portugal	18355.9	16
Romania	4707.28	27
Slovakia	11974.2	20
Slovenia	17371.6	17
Greece	20431.43	15

Since we have made an evaluation based on the sum of the intraclass distances, we can say that the value of the Spearman Correlation Coefficient obtained is reasonable for the larger value test. In the clustering of EU Member States in terms of health factors, 4 clusters obtained with the Canopy trial can be used. These clusters are presented in Figure 1.

3. Conclusion

In the study, European Union member states are clustered in terms of health services. The application is performed using the Weka software and the K-means method.

Table 4. Spearman Correlation Coefficients for trials.

Trial	Number of Clusters	Initial Clustering Approach	Spearman Correlation Coefficient
1	3	Random	0.7893
2	3	K-Means++	0.7126
3	3	Canopy	0.7969
4	3	Farthest first	0.7682
5	4	Random	0.7920
6	4	K-Means++	0.7184
7	4	Canopy	0.8035
8	4	Farthest first	0.7693

Spearman rank correlation coefficient is calculated to evaluate clusters obtained by using different initial clustering approaches and cluster numbers. 4 clusters with the Canopy approach seems the best. For future studies, different clustering approaches can be tried in the same data set, results can be obtained with different variables. The clusters can be evaluated according to the Pearson correlation coefficient using numerical variables, not rank variants.

References

- [1] J. MacQueen, Proc. Fifth Berkeley Symposium on Mathematical Statistics and Probability, 21 June – 18 July, 1965 and 27 December, 1965 - 7 January, 1966 Berkeley-USA.
- [2] F. Ersöz Analysis of health levels and expenditures of Turkey and OECD countries , Journal of Statisticians: Statistics & Actuarial Sciences, 2 (2008) 95–104.
- [3] F. Lorcü, B. A. Bolat, A. Atakisi, Examining Turkey and Member States of European Union in Terms of Health Perspectives of Millennium Development Goals, Quality & Quantity, 46 (2012) 959-978. DOI: 10.1007/s11135-011-9648-1
- [4] N. Alptekin, Comparison of Turkey and European Union Countries' Health Indicators by Using Fuzzy Clustering Analysis, International Journal of Business and Social Research, 4 (2014) 68-74. DOI: 10.18533/ijbsr.v4i10.607
- [5] K. E. Lewandowski, S. H. Sperry, B. M. Cohen, D. Öngür, Cognitive variability in psychotic disorders: a cross-diagnostic cluster analysis, Psychological Medicine, 44 (2014) 3239-3248. DOI: 10.1017/S0033291714000774
- [6] D. K. Moser, K. S. Lee, J. R. Wu, G. Mudd-Martin, T. Jaarsma, T. Y. Huang, X.Z. Fan, A. Strömberg, T. A. Lennie, B. Riegel, Identification of symptom clusters among patients with heart failure: An international observational study, International Journal of Nursing Studies 51 (2014) 1366-1372. DOI: 10.1016/j.ijnurstu.2014.02.004
- [7] C. H. Olson, S. Dey, V. Kumar, K. A. Monsend, B. L. Westra, Clustering of elderly patient subgroups to identify medication-related readmission risks, International Journal of Medical Informatics 85 (2016) 43-52. DOI: 10.1016/j.ijmedinf.2015.10.004
- [8] S. Tsumoto, S. Hirano, H. Iwata, Mining Schedule of Nursing Care based on Dual-Clustering, Procedia Computer Science, 55 (2015) 1203-1212. DOI: 10.1016/j.procs.2015.07.125
- [9] T. M. Kodinariya, P. R. Makwana, Review on determining number of Cluster in K-Means Clustering, International Journal of Advance Research in Computer Science and Management Studies, 6 (2013) 90-95.
- [10] World Bank (26.03.2016). World Development Indicators. Link: <http://data.worldbank.org/data-catalog/world-development-indicators> Access data: 26.03.2016.



Optimization of Traffic Signalization For Complex Roundabout By Fuzzy Logic According To Various Parameters

Tolga PALANDIZ^{1*}, Ramazan ŞENOL², Hilmi Cenk BAYRAKÇI¹

¹Isparta University of Applied Sciences, Technology Faculty, Mechatronics Engineering Dept., 32200, Isparta-Turkey

²Isparta University of Applied Sciences, Technology Faculty, Electric-Electronic Engin. Dept., 32200, Isparta-Turkey

* Corresponding Author : tolgapalandiz@gmail.com

ORCID: 0000-0003-0871-6129

Article Info:

DOI: 10.22399/ijcesen.446666

Received : 22 July 2018

Accepted : 05 January 2019

Keywords

Fuzzy logic

Intersection control

Traffic signalization

Abstract:

In this study, traffic signalization by fuzzy logic according to number of vehicles, vehicle type, fuel and time parameters of 5 leg roundabouts were simulated in computer environment. For this purpose, city surveillance cameras (mobese) were used for the selected intersection. In the simulation, the Mamdani type fuzzy model was used. The results of the application are listed in tables. According to the vehicle density coming near the intersection, the transition times or stopping times applied to the intersection were optimized. Also, types of vehicles coming near the intersection are analyzed and vehicles with high fuel consumption are given priority. Thus, fuel consumption and environmental pollution can be reduced. The methods in this study are compared in terms of fuel saving, environmental effects and faster road flow. Accordingly, neutral fuel consumption with fuzzy logic method is averagely % 15.9 less than classical method.

1. Introduction

Decision mechanisms of human didn't occur from "yes" and "no" like computers. In the face of relative situations every human has different answers. The basis of fuzzy logic occurred from fuzzy clusters. Fuzzy clusters are the most basic elements of fuzzy systems. The fuzzy set theory was described in the work of Zadeh [1]. There were so many studies made to improve signalization process at intersections. Artificial neural network and fuzzy logic were mainly used at designed systems. At 1977, Pappis and Mamdani were designed a decider model which was used signal circuit, queue length and extension time as parameters[2]. Tzes et al. were designed a traffic signal control for transportation networks at 1995 [3]. Tzes, McShane and Kim were improved a fuzzy logic based simulation model and they were compared this model with fixed time signalization [3]. Jongwan Kim by developing a simulation model for discrete and 4-phase supervised intersections with the help of their own developed

control algorithm, were determined of difference from fixed time signalization [4]. Desai and Somani (2014), Hegyi et al. (2009), and Kuhne (1991), were determined different vehicle determination techniques based real-time sensor readings to help computer's vision at the solve of traffic congestion [5,6,7]. Some problems were emerged at the end of failure to provide effective traffic flow of conventional intersection systems. In this study, differences of fuzzy logic system and conventional system were revealed. Image processing is a computational process that transforms one or more input images into an output image [8]. Meng and Chen (2015) an approach to clustering analysis and multi-attribute decision making under hesitant fuzzy environment is developed, which can cope with the situations where the weight information is incompletely known and there exist interactions between attributes [9]. Chen et al. (2015) an improved AB model is presented and can be applied to all arrival cases. Through the membership function, the delay time of platoon can be computed for all arrival cases [10]. Czubenko et

al. (2015) concern an adaptation of the ISD system to the role of an intelligent driver (xDriver), in a virtual environment [11]. The system processes vehicles with an image processing method in a fuzzy system as a car, a minibus and a truck which approach to a junction. Thus, number of various vehicles approaching to a junction and consumptive fuel quantity was compared with fuzzy logic rules and the most suitable transition time was aimed to calculate. In this method, the junction is controlled continuously in loops. Reducing traffic density at the intersection, decreasing fuel consumption while stopping by traffic lights and correspondingly minimizing savings, CO₂ emission and protection of the environment shows that this method is more advantageous than the classical method.

2. Application of Traffic Signalization with Fuzzy Logic

The two most common methods used in traffic signalizations are fixed-time traffic signalizations and the second is traffic actuated signalization systems. In fixed-time signalization, the circuit durations and phase orders are predefined and the system works fixedly in this way. In traffic actuated method, circuit times and phase orders can be dynamically controlled and changed according to the intensity of traffic during different times of the day [12]. The intersection where the signalization is performed by the fuzzy logic method is given in Figure 1. X road is including A, D and C roads, and Y road is including B and E roads. It is assumed that the traffic intensity of roads A, B and E is higher than roads C and D, and two main groups, X and Y, are separated as in Figure 1. Here, A, D and C roads are treated as subcomponents of X. Also B and E roads are treated as subcomponents of Y. Input parameters for the generated fuzzy logic-based control; number of cars, minibuses, trucks and idle fuel quantities on the A, B, C, D and E roads. The output parameters are green light durations on the A, B, C, D, E roads. The algorithm of the installed system is given in Figure 2. The structure of X in the system is shown in detail in Figure 3. Inputs and outputs on the X road are determined. The structure of Y in the system is shown in detail in Figure 4. Inputs and outputs on the Y road are determined. Three different parameters are used for the fuzzifier process of the total number of vehicles on X road by fuzzy logic: low, normal and high. Values have been correlated with the numerical values in the case of monitoring of the intersection so as to increase the accuracy of the system. The fuzzifier process was also applied to the total amount of fuel consumed on X road and

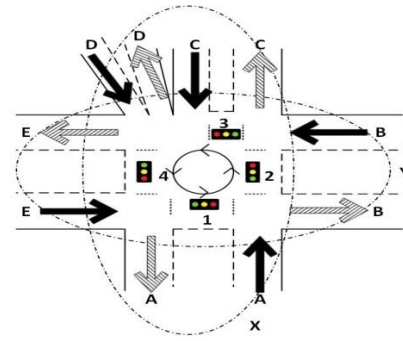


Figure 1. Drawing of intersection.

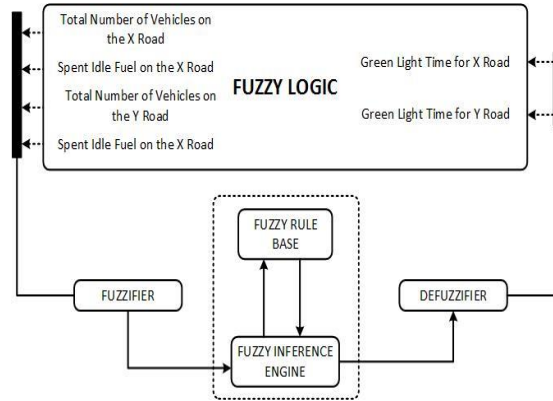


Figure 2. The algorithm of the installed system.

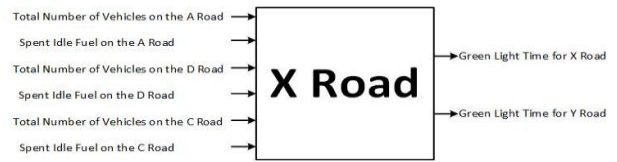


Figure 3. Inputs and outputs on the X road.

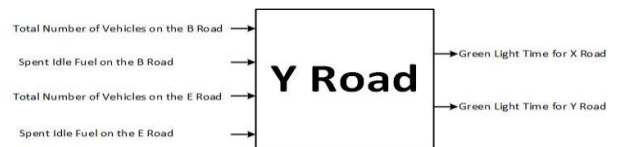


Figure 4. Inputs and outputs on the Y road.

the duration of green light on X road. The distribution of roads by vehicle type is given in Table 1. The values given are taken from real life. Waiting times vary for each road in the intersection where the simulation is performed. Therefore, the values given in Table 2 are equal to the amount of fuel in liters/ second spent waiting until the end of the lap on the road where the vehicles under examination reside.

3. Conclusion

At the simulation 17 laps were investigated and 1 lap was taken as 107 seconds, so the system was observed for about half an hour.

Table 1. Distribution of roads by vehicle types.

Laps	1st	2nd	3rd	...	15th	16th	17th
Car (X)	43	47	55	...	48	48	34
Minibus (X)	4	1	2	...	0	5	4
Truck (X)	1	0	1	...	0	0	0
Car (A)	19	26	23	...	20	16	17
Minibus (A)	1	0	1	...	0	2	1
Truck (A)	1	0	1	...	0	0	0
Car (D)	10	4	9	...	4	9	4
Minibus (D)	2	1	1	...	0	2	3
Truck (D)	0	0	0	...	0	0	0
Car (C)	14	17	23	...	24	23	13
Minibus (C)	1	0	0	...	0	1	0
Truck (C)	0	0	0	...	0	0	0
Car (Y)	25	19	22	...	15	20	26
Minibus (Y)	1	0	0	...	0	0	0
Truck (Y)	0	3	4	...	3	2	4
Car (B)	15	9	11	...	9	12	10
Minibus (B)	1	0	0	...	0	0	0
Truck (B)	0	1	2	...	2	2	0
Car (E)	10	10	11	...	6	8	16
Minibus (E)	0	0	0	...	0	0	0
Truck (E)	0	2	2	...	1	0	4

Table 2. Amount of idle fuel spent on roads by vehicle types.

Laps	1st	2nd	3rd	...	15th	16th	17th
Car (X)	0.38	0.42	0.49	...	0.43	0.43	0.3
Minibus (X)	0.11	0.02	0.05	...	0	0.14	0.11
Truck (X)	0.04	0	0.04	...	0	0	0
Car (A)	0.17	0.23	0.2	...	0.18	0.14	0.15
Minibus (A)	0.02	0	0.02	...	0	0.05	0.02
Truck (A)	0.04	0	0.04	...	0	0	0
Car (D)	0.14	0.05	0.12	...	0.05	0.12	0.05
Minibus (D)	0.08	0.04	0.04	...	0	0.08	0.13
Truck (D)	0	0	0	...	0	0	0
Car (C)	0.18	0.22	0.31	...	0.32	0.31	0.17
Minibus (C)	0.04	0	0	...	0	0.04	0
Truck (C)	0	0	0	...	0	0	0
Car (Y)	0.34	0.26	0.3	...	0.2	0.27	0.35
Minibus (Y)	0.04	0	0	...	0	0	0
Truck (Y)	0	0.2	0.27	...	0.2	0.13	0.27
Car (B)	0.2	0.12	0.15	...	0.12	0.16	0.13
Minibus (B)	0.04	0	0	...	0	0	0
Truck (B)	0	0.06	0.13	...	0.13	0.13	0
Car (E)	0.13	0.13	0.15	...	0.08	0.11	0.22
Minibus (E)	0	0	0	...	0	0	0
Truck (E)	0	0.13	0.13	...	0.06	0	0.27

Moreover, in figure 5 neutral fuel consumptions, which were obtained from fuzzy methods, were calculated and compared according to the literature [13, 14,15]. Around the world the energy systems are mainly based on fossil fuels. However, in the near future, as a result of excessive use, the sources of fuel will start to decrease and this will lead to a

search of new reserves and invention of new Technologies [16]. However, in the near future, as a result of excessive use, the sources of fuel will start to decrease and this will lead to a search of new reserves and invention of new technologies [17]. In this study, per lap fuel consumptions were calculated in terms of liter/second. Accordingly, neutral fuel consumption with fuzzy logic method is averagely %15.9 less than classical method. According to the data which were obtained from Figure 5, approximately 5.82 liter fuel saving was provided in one hour with the usage of fuzzy logic method. Plus, 3.7 tone CO₂ emission can be prevented or 167.8 trees can be saved. By this means, per hour 8.61\$ economic loss can be resolved. If we write these values daily or annually by supposing that the traffic is daily averagely crowded for 10 hours, respectively on a daily basis fuel consumption, economic profits, CO₂ emission and saved trees will be 58.2 liter, 86.1\$, 37 tone and 1678.

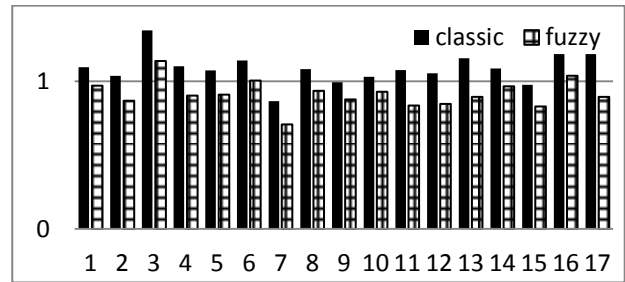


Figure 5. Comparison of fuzzy logic and classical method in terms of idle fuel consumption.

Respectively on annual basis, fuel consumption, economic profits, CO₂ emission and saved trees will be 21243 liter, 31426.5 \$, 13505 tone and 612470.

References

- [1] L.A. Zadeh, Inform. Control 8, 338 (1965).
- [2] Pappis, C.P.,Mamdani, E.H., A Fuzzy Logic Controller for a Traffic Junction, IEEE Transactions on systems, Man and Cybernetics, 707-717,(1977).
- [3] Tzes A., McShane and Kim, S., Expert Fuzzy Logic Traffic Signal Control for Transportation Networks, Institute of Transportation Engineers 65th Annual Meeting, Denver USA, 154-158, (1995).
- [4] Kim, Jongwan, A Fuzzy Logic Control Simulator for Adaptive Traffic Management, Proc IEEE International Conference on Fuzzy Systems, 1519-1524, (1997).
- [5] Desai, D., Somani, S., 2014. Instinctive traffic control and vehicle detection techniques.

- International Journal of Scientific & Engineering Research 5 (1), 2192-2195.
- [6] Hegyi, A., Bellemans, T., De-Schutter, B., 2009. Freeway traffic management and control, In: Meyers, R.A. (Ed.), *Encyclopaedia of Complexity and Systems Science*. Springer, New York, pp. 3943-3964.
- [7] Kuhne, R.D., 1991. Freeway control using a dynamic traffic flow model and vehicle reidentification techniques. *Transportation Research Record* 1320, 251-259.
- [8] N.G. Adar* , A. Egrisogut Tiryaki and R. Kozan , *Acta Phys. Pol. A* 128, B-348(2015)
- [9] F. Meng, X. Chen, 2015. Correlation Coefficients of Hesitant Fuzzy Sets and Their Application Based on Fuzzy Measures, *Cognitive Computation*, August 2015, Volume 7, Issue 4, pp 445–463.
- [10] F. Chen, L. Wang, B. Jiang, C. Wen, 2015. An Arterial Traffic Signal Control System Based on a Novel Intersections Model and Improved Hill Climbing Algorithm, *Cognitive Computation*, August 2015, Volume 7, Issue 4, pp 464–476.
- [11] M. Czubenko, Z. Kowalczyk, A. Ordys, 2015. Autonomous Driver Based on an Intelligent System of Decision-Making, *Cognitive Computation*, October 2015, Volume 7, Issue 5, pp 569–581.
- [12] Şimşir, F., Özkaynak, E., Ekmekçi D., “Kavşaklarda Trafik Sinyalizasyon Sisteminin Modellemesi ve Benzetimi”, *Akademik Bilişim*, (2013).
- [13] https://www.anl.gov/sites/anl.gov/files/idling_worksheet.pdf(Access Date: 21.08.2017)
- [14] www.cleancities.energy.gov (Access Date: 21.08.2017)
- [15] <https://www.afdc.energy.gov>(Access Date: 21.08.2017)
- [16] O.M. Pişirir and O. Bingöl, *Acta Phys. Pol. A* 130, 36 (2016)
- [17] B. Kiriş , O. Bingöl , R. Şenol and A. Altıntaş, *Acta Phys. Pol. A* 130, 55 (2016)



Effect of Change in Radial Clearance on Pressure Variation of Fluid in Hydrodynamic Journal Bearing

Iredia ERHUNMWUN*, John AKPOBI

University of Benin, Faculty of Engineering, Department of Production Engineering, Benin City, Nigeria

* Corresponding Author : iredia.erhunmwun@uniben.edu
ORCID: 0000-0002-0497-8220

Article Info:

DOI: 10.22399/ijcesen.492548

Received : 05 December 2018

Accepted : 14 February 2019

Keywords

Hydrodynamic lubrication
Journal bearing
Weak formulation
Radial clearance
Finite Element Method

Abstract:

This work entails the parametric study of the effect of the change in bearing radial clearance with pressure variation of the fluid (lubricant) in a hydrodynamic journal bearing was carried out. The classical Reynolds Equation was used to represent the pressure behaviour in the bearing. This study was carried out using the Galerkin Finite Element Method (GFEM). The result obtained shows that the pressure increases from the ambient pressure which is taken to be zero and increases significantly till 145.3737^0 . At this point, the pressure is maximum with 1.955 MPa and then drop until it gets to 180^0 where the pressure equals the ambient pressure. Between angular displacements of 180^0 and 360^0 there were also pressure variations which were equal in magnitude with those between 0^0 and 360^0 but with different direction. From the foregoing, it is observed that as the radial clearance increases, the pressure in the bearing drops significantly. Therefore, in the design of journal bearings, the radial clearance should be as high as possible to reduce the pressure in the bearing. The result obtained shows a strong positive correlation with existing result in literature.

1. Introduction

In hydrodynamic bearing, the fluid film separates the bearing and journal and thus permits a relative motion between the contacts surfaces with minimal friction. This fluid film reduces the wear of machine elements and also carries away the generated heat [1]. Clearance between the journal and bearing shells is the most important factors when it comes to the health and durability of assembly because that open area is filled with oil which provides a cushion between the journal itself and the bearing [2]. A few micron variations in the clearance may cause serious changes in different performance parameters of the bearing [3]. This important parameter can be managed at three stages of bearing life cycle such as designing, manufacturing and usage [4]. Ocvfik et al. [5] scrutinized the effect of bearing-clearance on the friction power loss, the film thickness, and the peak pressure in the oil film. They reported that the load

capacity passes through a maximum value at a small bearing clearance and then decreases with increasing bearing clearance. Mitsui et al [6] concluded that with the decrease of clearance ratio, there is an increment in the maximum bearing temperature, speed and lubricant viscosity. Prashad et al. [7] presented the effects of viscosity and clearance on the performance of hydrodynamic Journal Bearings. The higher clearance leads to an increase in the axial flow rate particularly under high applied loads and high rotational speeds [8]. El-Kersh et al. [9] analyzed the effect of thermal expansion on three polymer composite journal bearings at different rotational speeds and clearance ratio. They found that, the increase of bearing clearance ratio leads to increase the friction coefficient and minimum oil film thickness and at the same time reduces the maximum bearing temperature and load carrying capacity. Similar observations were made by [10]. They scrutinized the counter rotating floating ring journal under

different working conditions. Their investigation revealed that by decreasing the radii ratio (R_2/R_1) of the ring and clearance ratio (C_1/C_2), the coefficient of friction decreases at the same time, with this the load carrying capacity of the bearing increases. Gangrade et al. [11] found that the performance of hydrodynamic journal bearing is mainly affected by clearance ratio, aspect ratio and speed. Amit et al. [12] investigated the effect of clearance on pressure distribution and fluid film thickness of fluid film journal bearing. The behavior of these performance parameters at different relative clearance in circumferential and axial direction is scrutinized. Simms et al. [13] showed that the results for the large clearance configurations did not show the dramatic variation in maximum bearing temperature associated with a transition from laminar to turbulent cooling that was found for standard clearance cases. Papadopoulos et al. [14] theoretically presented the identification of clearances and stability analysis for a rotor journal bearing system using response measurements of the rotor at a particular point i.e the midpoint of the rotor. The measurements should be taken at two different speeds and from different wear effects. This present work also verified experimentally from the previous work. [4] studied on the journal bearing performances and metrology issues. In this experimental study out-of-roundness and radial clearance of journal bearings were measured with high precision and the impact of their metrology was examined on the specific oil film thickness of the bearing. Results showed that the radial clearance measurements can vary from one measuring device to another and the specified clearance may not necessarily meet the design criteria of specific oil film thickness. Tian et al. [15] examined the effect of bearing outer clearance on dynamic behavior of full floating ring and observed that the stability could be enhanced by increasing clearance. Fargere et al. [16] examined that the alignment of the shaft can be modified by changing the bearing clearance. Harpreet et al. [17] theoretically examine the influence of clearance parameter on the non-dimensional values of pressure distribution and static performance parameter for the bearing operating under three different values of clearance parameter. Mane et al. [18] presented a paper on the 3D model of hydrodynamic plain journal bearing using COMSOL Multiphysics 4.3a software.

In all the literatures reviewed so far, there is no general analytic solution to the classical Reynolds Equation that models the effect of side or end leakage; however, approximate solutions have been obtained by using electrical analysis, mathematical summations, relaxation methods and numerical and

graphical methods [19]. This study is presented to investigate the effect of change in radial clearance with the pressure distribution in a journal bearing under hydrodynamic lubrication assuming that the bearing is infinitely short.

2. Governing Equation and boundary conditions

The governing Equation for pressure variation in an infinitely short hydrodynamic journal bearing is shown thus:

$$\frac{\partial}{\partial z} \left(\frac{h^3}{\mu} \frac{\partial P}{\partial z} \right) = 6U \frac{\partial h}{\partial x} \quad (1)$$

where P = pressure, z = Axial direction, h = Film Thickness, μ = Lubricant viscosity, x = Circumferential direction, U = Linear velocity

Eq. 1 is the well-known Reynolds Equation for a bearing that is assumed to be infinitely short. This Equation is subject to the following set of initial and boundary conditions.

$$P(\theta, 0) = P(\theta, L) = 0 \quad (2)$$

where θ = Angular displacement, L = Length of the bearing

For symmetry reasons,

$$\left. \frac{\partial P}{\partial z} \right|_{z=0} = 0 \quad (3)$$

The domain of the problem consists of all points between $z = 0$ and $z = L$ i.e. $\Omega = (0, L)$. The domain was divided into a set of line elements, a typical element being of length h_e and located between two arbitrary points A and B. The collection of such elements is called the finite element mesh of the domain. The reason for dividing the domain into finite elements was to represent the geometry of the domain and to approximate the solution over the entire domain.

3. Mathematical analysis

In the development of the weak form, we assumed a linear mesh and placed it over the domain. This was done by multiplying Eq. 1 by the weighted function (w) and integrating the final Equation over the domain. This results in the mathematical expression in Eq. 4.

$$\int_{z_A}^{z_B} \frac{h^3}{\mu} \frac{\partial w}{\partial z} \frac{\partial P}{\partial z} dz + \int_{z_A}^{z_B} 6wU \frac{\partial h}{\partial x} dz - wQ_A - wQ_B = 0 \quad (4)$$

Eq. 4 is known as the weak form of the governing equation for hydrodynamic lubrication in journal bearing.

The weak form requires that the approximation chosen for P should be at least linear in z so that there are no terms in eq. 4 that are identically zero. Since the primary variable is simply the function itself, the Lagrange family of interpolation functions is admissible. We proposed that P is the approximation over a typical finite element domain by the expression:

$$P^e = \sum_{j=1}^n P_j^e \psi_j^e(z) \text{ and } w = \psi_i^e(z) \quad i, j = 1, 2, 3 \quad (5)$$

where $w = \psi_i^e(z)$ is the trial function

In Galerkin's weighted residual method, the weighting functions are chosen to be identical to the trial functions [20].

Substitute eq. 5 into eq. 4, we have:

$$\frac{h^3}{\mu} [K_{ij}^e] \{P_j^e\} = -6U \frac{\partial h}{\partial x} \{F_i^e\} + \{Q_i^e\} \quad (6)$$

$$\text{where } K_{ij}^e = \int_{z_A}^{z_B} \frac{\partial \psi_i^e(z)}{\partial z} \frac{\partial \psi_j^e(z)}{\partial z} dz \quad (7)$$

assembling, we have:

$$F_i^e = \int_{z_A}^{z_B} \psi_i^e(z) dz \quad (8)$$

$$Q_i^e = \psi_i^e(z) Q_A + \psi_i^e(z) Q_B \quad (9)$$

Eq. 6 is referred to as the finite element based model, eq. 7 is known as the bearing matrix and eq. 8 is referred to as the wedge matrix.

Hence, the one-dimensional Lagrange quadratic interpolation function for Equation becomes

$$\begin{aligned} \psi_1 &= \left(1 - \frac{z}{h_e}\right) \left(1 - \frac{2z}{h_e}\right), \\ \psi_2 &= \frac{4z}{h_e} \left(1 - \frac{z}{h_e}\right), \\ \psi_3 &= -\frac{z}{h_e} \left(1 - \frac{2z}{h_e}\right) \end{aligned} \quad (10)$$

where $h_e =$ Elemental length of the bearing

3.1. Evaluating the bearing matrix $[K_{ij}]$ and wedge matrix $\{F^e\}$ for journal bearing

To evaluate the K_{ij} matrix, we substitute eq. 10 accordingly into eqs. 7 and 8 respectively, we have;

$$K^e = \frac{1}{3h_e^3} \begin{bmatrix} 7h_e^2 - 24h_e z_A + 48z_A^2 & -8(h_e^2 - 3h_e z_A + 12z_A^2) & h_e^2 + 48z_A^2 \\ -8(h_e^2 - 3h_e z_A + 12z_A^2) & 16(h_e^2 + 12z_A^2) & -8(h_e^2 + 3h_e z_A + 12z_A^2) \\ h_e^2 + 48z_A^2 & -8(h_e^2 + 3h_e z_A + 12z_A^2) & 7h_e^2 + 24h_e z_A + 48z_A^2 \end{bmatrix} \quad (11)$$

$$F = \left\{ \begin{array}{c} \frac{h_e - z_A + \frac{2z_A^2}{h_e}}{6} \\ \frac{2(h_e^2 - 6z_A^2)}{3h_e} \\ \frac{h_e + z_A + \frac{2z_A^2}{h_e}}{6} \end{array} \right\} \quad (12)$$

Eq. 11 represents the generalized form of the bearing matrix for the entire domain of the bearing and eq. 12 it represents the generalized form of the wedge matrix for the entire domain of the bearing..

In our analysis, the bearing domain was divided into four quadratic elements as shown in Figure 1.

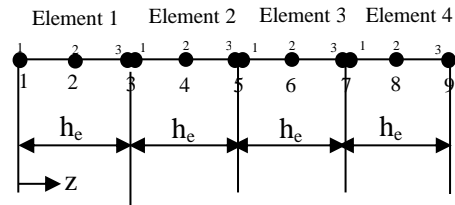


Figure 1: A four quadratic element

Analysing the elements part by part and finally

$$[K^e] = \frac{1}{3h_e} \begin{bmatrix} 7 & -8 & 1 & 0 & 0 & 0 & 0 & 0 & 0 \\ -8 & 16 & -8 & 0 & 0 & 0 & 0 & 0 & 0 \\ 1 & -8 & 38 & -80 & 49 & 0 & 0 & 0 & 0 \\ 0 & 0 & -80 & 208 & -128 & 0 & 0 & 0 & 0 \\ 0 & 0 & 49 & -128 & 230 & -344 & 193 & 0 & 0 \\ 0 & 0 & 0 & 0 & -344 & 784 & -440 & 0 & 0 \\ 0 & 0 & 0 & 0 & 193 & -440 & 614 & -800 & 433 \\ 0 & 0 & 0 & 0 & 0 & 0 & -800 & 1744 & -944 \\ 0 & 0 & 0 & 0 & 0 & 0 & 433 & -944 & 511 \end{bmatrix} \quad (13)$$

$$\{F^e\} = \frac{h_e}{6} \left\{ \begin{array}{c} 1 \\ 4 \\ 8 \\ -20 \\ 56 \\ -92 \\ 152 \\ -212 \\ 127 \end{array} \right\} \quad (14)$$

Substitute in eq. 6, eqs. 13 and 14 and finally, substituting the boundary conditions in eqs. 2 and 3 and also these parameters $h_e = L/4, U = \omega r, x = r\theta$ and $h = c(1 + \varepsilon \cos\theta)$, we have:

$$\begin{bmatrix} 16 & -8 & 0 & 0 & 0 & 0 & 0 & 0 \\ -8 & 38 & -80 & 49 & 0 & 0 & 0 & 0 \\ 1 & -80 & 208 & -128 & 0 & 0 & 0 & 0 \\ 0 & 49 & -128 & 230 & -344 & 193 & 0 & 0 \\ 0 & 0 & 0 & -344 & 784 & -440 & 0 & 0 \\ 0 & 0 & 0 & 193 & -440 & 614 & -800 & 0 \\ 0 & 0 & 0 & 0 & 0 & -800 & 1744 & 0 \end{bmatrix} \begin{bmatrix} P_2 \\ P_3 \\ P_4 \\ P_5 \\ P_6 \\ P_7 \\ P_8 \\ P_9 \end{bmatrix} = \frac{3\omega L^2 \mu \varepsilon \sin \theta}{16c^2(1+\varepsilon \cos \theta)^3} \begin{bmatrix} 4 \\ 8 \\ -20 \\ 56 \\ -92 \\ 152 \\ -212 \end{bmatrix} \quad (15)$$

where L = Length of Bearing, U = Linear velocity, ω = Angular velocity, r = radius of bearing, c = radial clearance, ε = eccentricity ratio

4. Results and Discussion

The parameters used in this analysis is as shown in Table 1.

Table 1. Parameters for calculation for short journal bearing [18]

Parameters	Short bearing
Lengths of bearing	2.50x10 ⁻² (m)
Diameter of journal	0.05 (m)
Radial clearance	2.50x10 ⁻⁵ (m)
Eccentricity	1.25x10 ⁻⁵ (m)
Eccentricity ratio	0.50
Speed of journal	1000 (rpm)
Dynamic viscosity of oil	0.19 (Pa.S)
Inlet temperature	315 (K)

4.1. Variation of pressure with angular displacements for journal bearing

The results obtained for the variation of pressure with angular displacements for a hydrodynamically loaded journal bearing which was assumed to be infinitely short is as shown in Figure 2. In the infinitely short journal bearing condition, it was assumed that there was no side leakage. The nodal values were the pressures at those points on the bearing. The graph shown was in a sinusoidal wave form. P1 to P9 shows the pressure distribution at the various nodes from 1 to 9 respectively. A combination of both the Neumann and Dirichlet boundary conditions was used. From the boundary conditions used, the pressure increases from the ambient pressure which was taken to be zero at an angular displacement of 0⁰ and increases significantly till 145.3737⁰ where the pressure becomes maximum with 1.9955 MPa. Thereafter, it began to drop until it gets to 180⁰ where the pressure became the same as the ambient pressure. From this point onward, we began to experience negative pressure. The negative pressures in this regard were those that were below the ambient pressure. At this point, cavity began to set in. This

pressure increases in the negative direction till 210.6262⁰ and back again to the ambient pressure at 360⁰. Then, another cycle began between 360⁰ and 720⁰ and so on.

Note that this research was carried out at a constant inlet temperature of 315K as shown in Table 1 above.

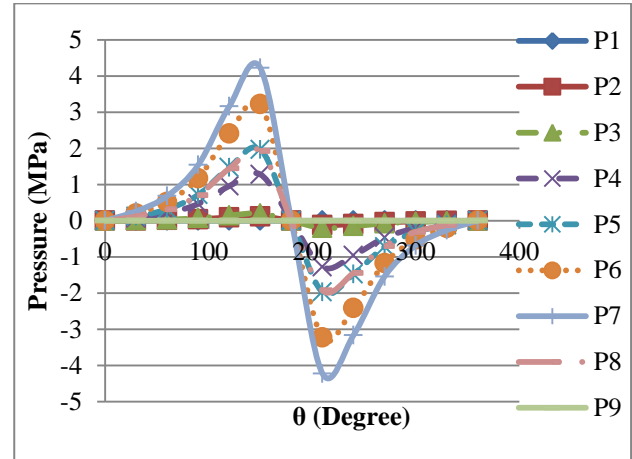


Figure 2. A graph of all the pressures against angular displacement

The result from FEM was validated by comparing it with the result from the analytical solution and the result published by [18]. The comparison shows a strong positive correlation. The FEM approximates the solution to the analytical solution better than the result by [18]. This is shown in Table 2.

Table 2: Comparison between FEM, COSMOL and Analytical solution

Q (°)	ANALYTICAL	COSMOL	FEM
0	0	0	0
30	122565	120231	122000
60	317565	315456	318375
90	718245	717546	718023
120	1491345	1415657	1473959
150	2003459	1954563	1969648
180	0	0	0
210	-2003459	-1954563	-1969648
240	-1491345	-1415657	-1473959
270	-718245	-717546	-718023
300	-317565	-315456	-318375
330	-121565	-120231	-122000
360	0	0	0

4.2. Pressure variation with change in radial clearance

In hydrodynamic bearing, the fluid film separates the bearing and journal and thus permits a relative motion between the contacts surfaces with minimal friction. This fluid film reduces the wear of machine elements and also carries away the generated heat. Clearance between the journal and bearing shells is the most important factors when it comes to the health and durability of assembly because that open area is filled with oil which provides a cushion between the journal itself and the bearing. A few micron variations in the clearance may cause serious changes in different performance parameters of the bearing. This important parameter can be managed at three stages of bearing life cycle such as designing, manufacturing and usage.

The graph showing the variation of pressure with change in radial clearance is shown in Figure 3. From Figure 3, the range of radial clearance used is between 0.000005m and 0.0001m. From the foregoing, it is observed that as the radial clearance increases, the pressure in the bearing drops significantly. Therefore, in the design of journal bearings, the radial clearance should a high as possible to reduce the pressure in the bearing.

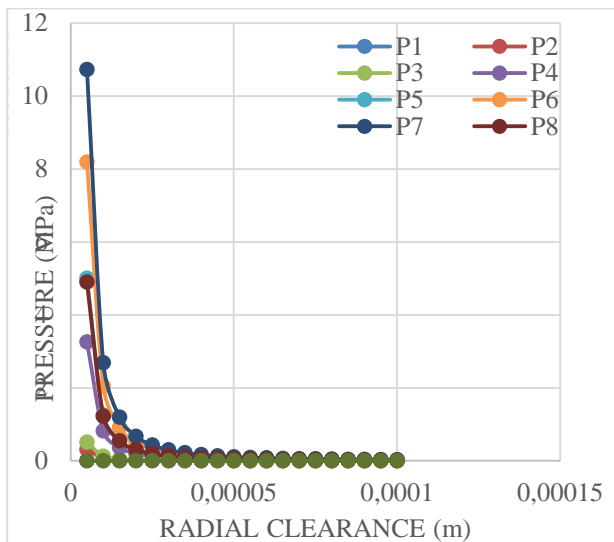


Figure 3. Variation of pressure with radial clearance

5. Conclusion

The pressure distribution of the hydrodynamic journal bearing lubricated with oil under steady state and constant temperature consideration has been analysed. Based on the results and discussion presented in the preceding section, the following conclusions can be reached.

The Finite Element Method (FEM) form of the general governing Reynolds Equation was derived and implemented for hydrodynamic journal

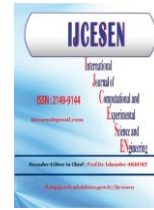
bearing. Using Reynolds Equation, a numerical solution has been developed for short journal bearing under steady state. The finite element method provides the node by node results for pressure distribution. Using FEM, the result obtained was compared with COSMOL and analytical solution. It was found that FEM gives approximately identical solution for short journal bearing.

From the foregoing, it is observed that as the radial clearance increases, the pressure in the bearing drops significantly. Therefore, in the design of journal bearings, the radial clearance should a high as possible to reduce the pressure in the bearing.

References

- [1] P. Tiwari and V. Kumar. Analysis of Hydrodynamic Journal Bearing: A Review, International Journal of Engineering Research and Technology, 1, 7, ESRSA Publications, 2012.
- [2] B. V. Bhandari. Design of Machine Elements, 3rd Edition, Tata Mcgraw Hill Education Private Ltd. New Delhi, India, ISBN-13: 978-0-07-068179-8, 2010.
- [3] S. P. Chu and E. Kay. Optimum Clearance Fits for Journal Bearings in Relation to BS 1916 and to Lubrication Theory, Wear, 27, 3, 329-343, 1974.
- [4] S. Sharma, D. Hargreaves and W. Scott. Journal bearing performance and metrology issues. Journal of Achievements in Materials and Manufacturing Engineering 32, 1, 98-103, 2009.
- [5] W. F. Ocvfik and B. G. D'ubois. Relation of Journal Bearing Performance to minimum oil film, NACA, TN 4223, 1958.
- [6] J. Mitsui, Y. Hori and M. Tanaka. An Experimental Investigation on the Temperature Distribution in Circular Journal Bearings, ASME Journal of Tribology 108, 4, 621- 626, 1986.
- [7] H. Prashad. The Effects of Viscosity and Clearance on the Performance of Hydrodynamic Journal Bearings, Tribology Transactions. 31, 2, 303-309, 1988.
- [8] I. Pierre and M. Fillon. Influence of Geometric Parameters and Operating Conditions on the Thermohydrodynamic Behavior of Plain Journal Bearings" Proc. of the Institution of Mechanical Engineers, Part J: Journal of Engineering Tribology, France, Sage publication, 214, 5, 445-457, 2000.
- [9] A. M. El-Kersh and W. Y. Ali. The effect of thermal expansion and elastic deformation on the performance of polyamide-copper journal bearings, KGK Kautschuk Gummi kunststoffe, 54, (9), 468-473, 2001.
- [10] B. A. Abass, A. A. Alwan and M. B. Hunain. An Investigation into the Performance of Counter Rotating Floating Ring Journal Under Different Working Conditions, Al-Khwarizmi Engineering Journal,3,1, 26-39, 2007.

- [11] A. K. Gangrade and V. M. Phalle. Effect of Clearance and Aspect Ratio On The Performance Of Water Lubricated Hydrodynamic Journal Bearing, *International Journal of Global Technology. Initiatives*, 5, 1, D59-D64, 2016.
- [12] M. Amit, R. K. Awasthi, S. S. Sarabjeet, D. Sandeep and S. Harpuneet. CFD Investigation of Clearance on Pressure Distribution and Fluid Film Thickness in Hydrodynamic Journal Bearing, *International Journal of Advance Research and Innovation*, Volume 4, Issue 2 571-575, 2016.
- [13] J. E. L. Simms and S. J. Dixon. Effect of load direction, preload, clearance ratio, and oil flow on the performance of a 200 mm journal pad bearing” *Tribology Transactions*, 37, 227-236, 1994.
- [14] A. C. Papadopoulos, G. Nikolakopoulos and D. Gounaris. Identification of clearances and stability analysis for a rotor-journal bearing system, *Mechanism and Machine Theory*, 43, 411–426, 2008.
- [15] L. Tian, W. J. Wang and Z. J. Peng. Effects of bearing outer clearance on the dynamic behaviours of the full floating ring bearing supported turbocharger rotor, *Mechanical Systems and Signal Processing*, 31, 155-175, 2012.
- [16] R. Fargere and P. Velex. Influence of clearances and thermal effects on the dynamic behavior of gear-hydrodynamic journal bearing systems, *ASME Journal of Vibration and Acoustics*, 135, 061014-1-061014-16, 2013.
- [17] S. B. Harpreet, P. Gobind, R. K. Awasthi, S. M. Manjeet, S. Davinder, S. Navneet, K. Vijay and E. K. Keshwer. Impact of clearance contact on the performance of hydrodynamic journal bearing system, *International Journal of Advance Research and Innovation*, Volume 5, 1, 110-114, 2017.
- [18] R. M. Mane and S. Soni. Analysis of hydrodynamic plain journal bearing. Excerpt from the proceedings of the 2013 COSMOL Conference in Bangalore.
- [19] G. R. Budynas and K. J. Nisbett. *Shigley’s Mechanical Engineering Design*, 10th Edition, McGraw- Hill Education, New York, ISBN 978-0-07-339820-4. 2015.
- [20] J. N. Reddy, *Introduction to the Finite Element Method*, Second edition, McGraw-Hill series in Mechanical Engineering. 1993.



The Key Factor Analysis to the Reservoirs on the Basis of Bayesian Law

Jian SUN^{1*}, Qi LI¹, Mingqiang CHEN², Zekai ZHANG³

¹China University of Petroleum, College of Petroleum Engineering, 102249, Beijing -CHINA

²Xi'an shiyou University, College of Petroleum Engineering, 710065, Xi'an -CHINA

³ Tarim Oil Field, 84100, Korla -China

* Corresponding Author : xikelsj@163.com

ORCID: 0000-0002-5856-4824

Article Info:

DOI: 10.22399/ijcesen.422691

Received : 10 May 2018

Accepted : 21 February 2019

Keywords

Bayesian Law
Wushi Sag
Probability Theory
Poisson Distribution
Prospection

Abstract:

The oil price shocks further exaggerates the inherent difficulties in studying exploration of complex reservoirs. Therefore, as the main way of reducing cost, it's necessary to analyze the main factors of complex reservoir formation before intensively exploration. Bayesian law is used to build a diagnostic model. Six key factors in the effectiveness of hydrocarbon reservoir are starting points. According to the maximum entropy principle and single well event's probability of drilled wells with prior probability, the probability of adverse factors in the forming of hydrocarbon reservoir can be concluded. Therefore, influencing degree of each factor can be obtained. Meanwhile, by the theory of Slicher, the distribution of oil and gas reservoirs conform to Poisson's distribution. The results can be applied to calculate the probability of hydrocarbon reservoir's discovery and to predict the exploration potential of survey region. From the perspective of testing, this paper use Wushi sag as an example. By using the single well event's probability of nine drilled wells and calculating the influence value of key factors which are adverse to form the hydrocarbon reservoir in Wushi sag, this paper focuses on the key aspects-poor reservoir condition and absent migration pathway. By applying Poisson's distribution to study the exploration prospect, this study reveals that there is at least one district where commercial gas reservoirs will be discovered in Wushi sag. In conclusion, the diagnostic model based on Bayesian law provides a new and unique way of thinking to solve the geological problems in complex condition, and it is effective to the petroleum geological knowledge.

1. Introduction

Along with the sustained decline in oil price and the fall in conventional crude oil, the complexities forming conditions of the reservoirs bring about serious problems like high cost and difficult exploration. In order to reduce the cost and workload of exploration, the reliable and meaningful method is to analyze major influential factors by corresponding mathematical method. Meanwhile, this method can forecast the oil exploration potential. The background of the proposed question is the exploration situation of Wushi sag. Up to now, the degree of exploration in this area is low. Before the 1990's, the main reconnaissance is geological survey. Later in the 1990's, the company Exxon

obtained the mining rights and did some researches. However, Exxon claimed that it is too risky and costly for them to continue, so they finally gave up. Then the Tarim Oil Field Company did a lot of detailed prospecting about surface geology, seismic surveys and comprehensive researches and got some new ideas. One result of all these efforts is that well W1 was drilled and got commercial production [1]. However, the follow-on wells, such as Y2, Y101 and W2, were all dry holes. According to the above researching information of wells, another well S1 was drilled in 2005 and partly succeeded [2]. Since then nothing has been got from the wells such as S201, S3 and S4 [3]. The prospecting experience shows that the conditions in Wushi sag to form reservoirs are complex. The complex manifests in

two ways. One is that multiphase tectonic activities lead to intricate sedimentary facies. The other is that the key factors to reservoirs are uncertain. The poor quality of seismic data for the disadvantage surface creates an impediment to further perception. The only practicable way at present is to analyze the information from the drilled wells on the basis of Bayes formula. Then it is possible to make decision and guard exploration.

2. Theory and methodology

2.1 The concept about mathematics

Full probability formula: suppose that the sample space of stochastic experiment is S. A is an event in experiment. B1, B2...Bn is a partition in S, and P(Bi) > 0 (i=1, 2...n) so

$$P(A)=P(B1)P(A|B1)+P(B2)P(A|B2)+\dots P(Bi)P(A|Bi)\dots\dots (1)$$

That means if it is impossible to get the probability of event A directly, it can be decomposed into a few reciprocal simple events. Then the probability of event A can be got by adding the probability of probabilities of simple events.

The most important thing is to find out a partition in sample space S, then event A is divided into n parts as AB1, AB2...ABn. That is, A=AB1+AB2+...+ABn. Therefore, by additive formula (1) can be attained.

Bayes formula:

$$P(B_i|A) = \frac{P(B_i)P(A|B_i)}{\sum_{i=1}^n P(B_i)P(A|B_i)} \quad i=1, 2\dots n. \dots\dots (2)$$

Assuming that the probability of event A is the sum of event groups BiA (i=1, 2...n) which are incompatible with each other on the basis of partition. Event Bi is the event leading to event A. P(BiA) is the probability of leading result. If event happens, the probability of leading result by Bi, P(BiA)/P(A) is a conditional probability. The Bayes formula can then be obtained by multiplication formula and total probability formula [4,5].

2.2. The introduction of geological concepts

According to the theory on geology of petroleum, there are six key factors in the effectiveness of hydrocarbon reservoir: hydrocarbon source rocks in good conditions, reservoir bed in high quality, available cap rocks, good trap conditions, available migration conditions and steady preservation conditions. They are individually marked by letters G, R, C, T, M, S in this paper and HR means hydrocarbon reservoir. In consideration of logic theory, we can express that six factors can be

necessary and sufficient conditions to effectiveness of hydrocarbon reservoir. Thus we know that it's true for its converse-negative proposition. Then we can express its converse-negative proposition as the reasons which can be identified as poor hydrocarbon source rocks, reservoir bed in poor quality, unavailable cap rocks, poor trap conditions, unavailable migration conditions and unsteady preservation conditions for the ineffectiveness of hydrocarbon reservoir. The hydrocarbon reservoirs are destroyed, marked by capital letters $\bar{G}, \bar{R}, \bar{C}, \bar{T}, \bar{M}, \bar{S}$ and \overline{HR} . Only when the six key factors all in good conditions, it is possible to form an effective reservoir. By the identification of event, it can be described as:

$$HR = G \cap R \cap C \cap T \cap M \cap S$$

That is

$$G \cap R \cap C \cap T \cap M \cap S \subset HR \dots\dots (3)$$

If one of these factors is in poor condition, it is impossible to form hydrocarbon reservoirs. With the identification of sum of events, it can be expressed as:

$$HR \neq \overline{HR} = \bar{G} \cup \bar{R} \cup \bar{C} \cup \bar{T} \cup \bar{M} \cup \bar{S}$$

That is

$$\bar{G} \cup \bar{R} \cup \bar{C} \cup \bar{T} \cup \bar{M} \cup \bar{S} \subset \overline{HR} \neq HR \dots\dots (4)$$

With geologic theories and complete probability formula (1), if the probability of effective hydrocarbon reservoir is P(HR), sample space then can be partitioned into six events, which actually become a complete event group. Because the oil source rock(G), reservoir(R), cap rock(C), trap (T), migration(M), preservation(S) are incompatible with each other, and $G \cup R \cup C \cup T \cup M \cup S = E$ constructs the effective condition to form effective hydrocarbon reservoir. So the requirements of formula of total probability and Bayesian law can be used to analyze geologic problems and predicate the oil and gas distribution. Therefore, it is necessary to get the prior probability, and it is crucial for the problem to be solved [5].

3 Geological setting and geologic characteristics

Wushi sag formed in late Himalaya Movement in Neogene is an intermontane depression located in the west of Kuqa foreland basin (Figure 1). It is limited by southern Tianshan tectonic belt in the north and fault in the south with Wensu uplift, spreading nearly from east to west as a long belt [6,7]. Wushi sag is a Neozoic deposit sag on

Palaeozoic base, about 190 kilometers long from east to west and 35-40 kilometers wide from north to south with an area of about 3400 square kilometers. The tectonic setting is a combined action by tethyan tectonic belt from the end of Palaeozoic Era to Mesozoic Era (the southern Tianshan subduction orogeny belt) and Himalayan belt in Cenozoic Era (southern Tianshan collisional orogeny).

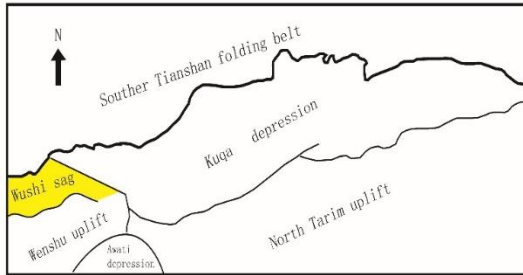


Figure 1. Schematic diagram showing the position of Wushi sag.

There are multiphase tectonic activities in this area. The sag was initiated in Devonian-Permian. During Triassic-Jurassic, it is a downfaulted basin with steady sedimentary facies and the hydrocarbon source rocks in this area deposited [8]. In Cretaceous period, the depositional environments sustained and became the target stratum (Figure 2). From Early Tertiary to Miocene Epoch, extra-thick stratum was formed. Between Miocene Epoch and Quaternary, it was the time that the foreland basin formed with extensive sediment. At the end of Quaternary, a lot of thrust faults in huge scale and folds, influenced by the orogeny in later Himalayan movement, are formed. The main hydrocarbon source rocks being coal measure strata formed in lake facies in Triassic-Jurassic [9].

Generally, terrigenous sequence is controlled by tectonic movement. The strata in the southern Wushi sag is controlled by the fault between Wushi sag and Wensu uplift (Figure 2). The accommodation space in this area changes and develops along with faults activity, so various depositional system tracts are formed. (Unit I :Fault as boundary with steep slope, near provenance in deep water with alluvial fans; Unit II :Fault and steep slope as boundary with deep water having local secondary fault horst zone—complex alluvial fans; Unit III :Double faults as boundaries, with shallow water-complex alluvial fans; Unit IV :Gentle slope, far away from provenance, shallow water with braided river deltas; Unit V :Local secondary fault horst zone, far away from provenance with semi-deep water; Unit VI :Strike-slip fault, far away from provenance with semi-deep water; Unit VII :Gentle slope, far away from provenance, semi-deep water with deltas; Unit

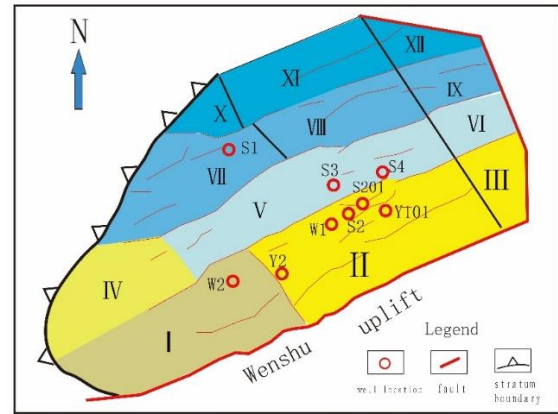


Figure 2. Schematic diagram of well locations-rift system-prospecting units.

VIII:Local secondary fault horst zone, far away from provenance with deep water; Unit IX : Strike-slip fault, local secondary fault horst zone, far away from provenance with deep water; Unit X :Gentle slope, far away from provenance with semi-deep water with subaqueous fans; Unit XI :Far away from provenance with deep water; UnitXII:Strike-slip fault as boundary with deep water—slope deep lake.)

In the early stage of lower sequence, due to the stronger fault activity, the accumulation space increases rapidly and topographic height difference is obvious. In W1 and Y101, coarse size sediments are found in low stand system tract (Figure 2), because they are close to Wensu uplift with rich provenance. S2 and S201 are far from the Wensu uplift, and fine size sediments are found (Figure 2). To the north, the water is deeper with hydrocarbon source rock. Lithologic traps and stratigraphic traps can be formed in the front of fan shaped lithosomic bodies, incised valleys and water transgression deltas and unconformity surface with underlying formation. With the development of fault, the setting velocity and the accumulation space increase to form the transgressive system-the sediments. To the north, the hydrocarbon source rocks distribute extensively because of the deeper water, but coarse size sediments deposit with smaller accumulation space and more obvious topographic height difference because of the faults activity in the sag, eg. S2 (Figure 2, 3A, 3B). There are transgressive actions of lithologic traps in the front of deltas and deep water turbidite fans. Then sediments deposit in the accumulation space to form the main target stratum-high stand system, because the faults are less active in this area. The deepest water, deep lake mudstone and condensed section are critical in forming underlying ability of oil production. The deltas, fan deltas and turbidite fans in this stage are reservoirs with high quality to form lithologic traps. After Cretaceous, there are four sets of tectonic movements to form a set of traps and faults, which

are late Yanshan Movement, early Himalaya movement, middle Himalaya movement and late Himalaya movement. The hydrocarbon rocks in the area of coal measure strata belonged to Triassic-Jurassic with extensive distribution. In this area, the Shushanhe formation in Cretaceous is the target zone [9]. According to the lithology, it can be divided into mud member, sand-conglomerate member and mud-sand member from top to bottom, corresponding to two sequences [10]. Sequence 1: upper Yageliemu formation to middle sand-conglomerate member; sequence 2: middle sand-conglomerate member to mud member. There are three systems tracts in sequence1: upper Yageliemu formation-lower of lower mud member belongs to low stand system tract; lower to middle of lower mud member belongs to transgressive system tract; middle to upper of lower mud member to lower sand-conglomerate member belongs to high stand system tract. Sequence 2 can be divided into two system tracts: the low stand system tract correlating with member from the lower sand-conglomerate to the top of sand-mud; transgressive system tract correlating with mud member (Figure 3A, 3B).

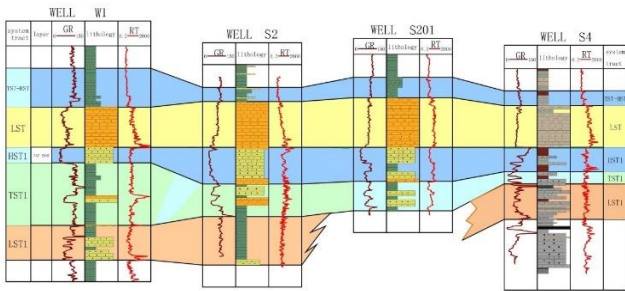


Figure 3A. Well Correlation in Wushi sag from east to west

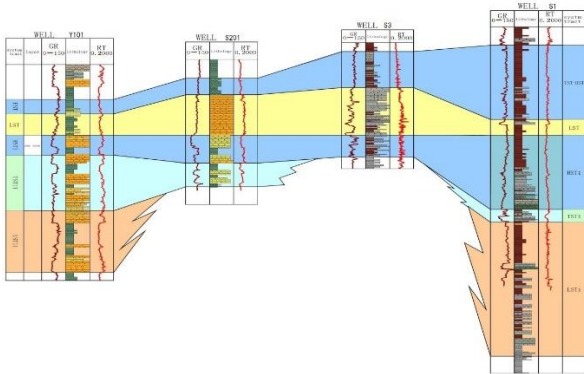


Figure 3B. Well Correlation in Wushi sag from north to South

The pay zone is the high stand system tract in sequence 1 with the facies of alluvial fans in the rocks of mud, silty shale, fine sandstone and conglomerate fine sandstone. Due to the great difference in sedimentary environment in this area, the thickness and components of target zone change both along the directions of trend (Figure 3A) and to

the lake center (Figure 3B), leading the geologic condition too complex to identify.

4 The application of Bayesian law in oil and gas prediction

4.1 The identification of prior probability

The cap rock is the upper compaction conglomerate bearing calcium. With same tectonic background, the reservoirs have the same sealing condition. Because reservoirs, cap rocks, lithologic traps can be formed in plenty kinds of system tracts and the form, distribution and preservation of structural traps are controlled by tectonic movements, the weighting of oil source rock, reservoir, cap rock, trap, oil-gas migration and hydrocarbon preservation (G, R, C, T, M, S) to form effective oil-gas traps is the same at one-sixth, so the prior probability of each factor is $P(G)=P(R)=P(C)=P(T)=P(M)=P(S)=1/6$.

By the way, theoretically the advisable prior probability can be attained by Bayes assumption with no known information. According to the Bayes assumption, when nothing is known about the prior probability, it is available to get the prior probability when it is considered as uniform distributed in the variable range. By the maximum entropy principle, for discrete information, it is supposed that the occurrence frequency of the sign for discrete information is $P_i (i=1, 2 \dots n)$. Then the information entropy can be identified as the expected information table from the sources of information.

$$H(X) = -\sum P_i \log(p_i)$$

It is entropy that characterizes the overall characteristics of uncertain degree for information source. Although it is less certain to get the information, the information quantity is abundant, as long as the information is available. For separate random variable, the entropy is at its maximum in equal probability mode [11].

Supposing Bayes on uniform distribution is accepted for prior probability, the result should be $P(G)=P(R)=P(C)=P(T)=P(M)=P(S)=1/6$. And the oil source rock, reservoir, cap rock, trap, oil-gas migration and hydrocarbon preservation (G, R, C, T, M, S) as discrete information sources, have the same information variant value by the maximum entropy principle.

That is, $P(G)=P(R)=P(C)=P(T)=P(M)=P(S)=1/6$. By the analysis on actual facts and theory, the prior probability of each key factor to the effective reservoirs is one-sixth.

4.2 The analysis of key factors for reservoir in Wushi sag

The reasons for each failure well in this area can be got by geologic analysis (Table1). ”√” and ”x”

stand for the favorable factors for the form of reservoirs ($A \subset HR$) and unfavorable factors for the form of reservoirs ($\bar{A} \subset \bar{HR}$).

Table 1. The factors to control the reservoirs from well in Wushi sag

Well factor	S1	S2	S201	S3	S4	W1	W2	Y2	Y101
Source rock condition	✓	✓	✓	✓	✓	✓	✓	✓	✓
Reservoir condition	✓	✓	✓	✗	✗	✓	✗	✗	✗
Cap rock condition	✓	✓	✓	✓	✓	✓	✓	✓	✓
Trap condition	✓	✓	✗	✓	✓	✓	✗	✗	✓
Migration condition	✓	✓	✓	✗	✗	✓	✗	✗	✗
Sealing condition	✓	✓	✓	✓	✓	✓	✓	✓	✓

By analyzing the data in Table 1, the information of each key factor can be figured out (Table 2). Using Bayes formula, the $P(A|Bi)$ of adverse factors in the forming of hydrocarbon reservoir can be concluded (Table 2). Ordering the values in sequence from the largest to the smallest, the key factors destroying the hydrocarbon reservoir can be shown.

Table 2. The cartogram of failure factors in wells, Wushi sag

failure factor	\bar{G}	\bar{R}	\bar{C}	\bar{T}	\bar{M}	\bar{S}
number	0	5	0	3	5	0
$P(A Bi)$	0	0.5556	0	0.3333	0.5556	0

Table 2 is the probability of failure wells from Bayes formula corresponding to various factors. For example, failure probability because of the poor reservoir \bar{R} is:

$$P(\bar{R}|\bar{HR}) = \frac{P(\bar{R})P(\bar{HR}|\bar{R})}{P(\bar{R})P(\bar{HR}|\bar{R}) + P(\bar{G})P(\bar{HR}|\bar{G}) + P(\bar{T})P(\bar{HR}|\bar{T}) + P(\bar{C})P(\bar{HR}|\bar{C}) + P(\bar{M})P(\bar{HR}|\bar{M}) + P(\bar{S})P(\bar{HR}|\bar{S})}$$

By plugging data into the formula, the result can be obtained as the following:

$$P(\bar{R}|\bar{HR}) = \frac{\frac{1}{6} \times \frac{5}{9}}{\frac{1}{6} \times \frac{5}{9} + \frac{1}{6} \times \frac{0}{9} + \frac{1}{6} \times \frac{3}{9} + \frac{1}{6} \times \frac{0}{9} + \frac{1}{6} \times \frac{5}{9} + \frac{1}{6} \times \frac{0}{9}} = 0.3846$$

Table 3. The failure probability of factors, Wushi sag

failure factor	\bar{G}	\bar{R}	\bar{C}	\bar{T}	\bar{M}	\bar{S}
$P(\bar{B}_i \bar{HR})$	0	0.3846	0	0.2308	0.3846	0

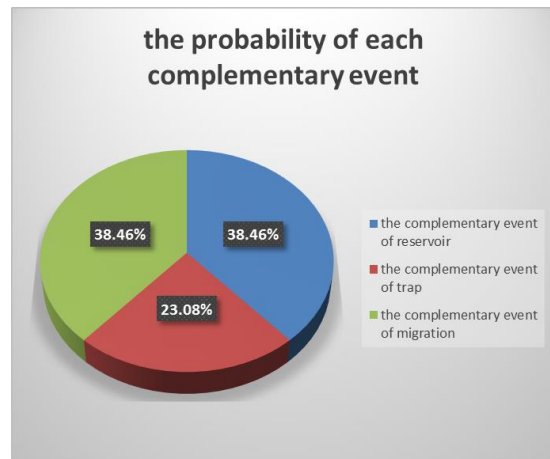


Figure 4. The probability of each complementary event

By the way, the failure probability of each key factor can be figured out (Table 3). So in conclusion, from Table 3 and Figure 4, there are three key factors leading to the spoiled oil-gas reservoir, which are poor reservoir condition, poor trap condition and the absent migration pathway. If the corresponding factor is sorted by value, it can be mathematically expressed as $\bar{R} = \bar{M} > \bar{T}$.

Thus, for the oil and gas exploration in Wushi sag, more attention should be paid to the range of reservoir distribution, reservoir lithology, reservoir quality and the faults connecting the underlying hydrocarbon rocks, unconformity characters and the relationship among the reservoir, faults and unconformities. Then the trap quality is the following aspect which is worthy of attention. Therefore, all these factors are directly related to problem that whether or not more oil and gas reservoirs with commercial production will be explored.

4.3 The number of potential hydrocarbon reservoirs

The Wushi sag can be divided into twelve districts sorted by standards such as the distance from the provenance, the boundary style, the slope ratio (gentle or steep), and the depth of water (Figure 2). The oil and gas reservoir is one of the mineral resources in nature. By the theory of Slichter, the distribution of oil and gas reservoirs conforms to Poisson's distribution. Currently, the reservoirs conditions, in Wushi sag, are that one district with one gas reservoir (unit VII), one district with two gas reservoirs (unit II) and ten without reservoirs (Table 4). The λ can be attained by unbiased estimation:

$$\lambda = \frac{\sum_{k=0}^2 k \times f_k}{\sum_{k=0}^2 f_k} = \frac{0 \times 10 + 1 \times 1 + 2 \times 1}{10 + 1 + 1} = \frac{3}{12} = 0.25$$

Then λ is plugged into Poisson equation (5)

$$P\{X = k\} = \frac{\lambda^k e^{-\lambda}}{k!} \dots (5)$$

Table 4. The number of oil and gas reservoirs discovered in units

Unit	I	II	III	IV	V	VI	VII	VIII	IX	X	XI	XII
Oil and gas reservoirs discovered	0	2	0	0	0	0	1	0	0	0	0	0

The probability of potential oil and gas reservoirs in Wushi sag can be figured out (Table 5). The percentage of districts without oil and gas reservoirs is 77.88%. In fact, up to now, the percentage of districts in which no oil and gas reservoirs have been found is 83.33%. The percentage of districts where the gas reservoirs have been found is 5.45% (83.33%-77.88%=5.45%). The number of districts where oil and gas reservoirs will be found is $12 \times 0.0545 = 0.654 \approx 1$. That is, in Wushi sag, there is at least one district where commercial oil and gas reservoirs can be discovered.

Table 5. The number of oil and gas reservoirs predicted by Poisson equation

The number of gas reservoirs discovered(K)	Frequent number (fx)	frequency	K*fx	Poisson theoretical probability
0	10	0.830	0	0.7788
1	1	0.083	1	0.1947
2	1	0.083	2	0.0243
Σ	12	0.996≈1	3	0.9978≈1

5 Conclusions

The probability theory is a rigorous and logical subject. In principle, the regularities among objectivities will be understood and mastered. On the basis of Bayes formula and information from well, the key factors to control the reservoirs can be identified.

The key factors in Wushi sag are reservoir condition and migration pathway. So, in the following stage, the researches about sequence stratigraphy, sedimentary and structures should be emphasized. Also the relationship between tectonic process with high quality reservoirs and the form of migration pathway deserves more attention.

In conclusion, by applying Bayes formula into available well information, the hydrocarbon potential is predicted. What's more, combining Bayes formula with the knowledge of oil geology provides an effective way to solve puzzling problems which can not be solved by other geological ways.

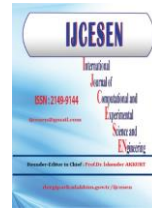
Acknowledgment

Grateful acknowledgement is made to my teacher, Professor Chen Mingqiang, who gave me

considerable help by means of suggestion, comments and criticism. In addition, I deeply appreciate the contribution to this thesis made by my friend, Zhang Bo.

References

- [1] Gong Deyu, Li Ming et al. (2014) Geochemical Characteristics and Origins of the Oils in Wushi Sag, Tarim Basin. *Natural Gas Geoscience* Vol.25 No.1 Jan.
- [2] Lei Ganglin, Ran Qigui et al. (2013) Characteristics and Controlling Factors of Mesozoic Reservoirs in Eastern Wushi Sag, Tarim Basin. *XINJIANG PETROLEUM GEOLOGY*. Vol.34 No.1Feb. 17-19.
- [3] Zhou Yanzhao, Lu Xuesong et al. (2016) The main controlling factors of reservoir physical property and oiliness in the structural lithologic reservoirs in the east of Wushi Sag, Kuqa foreland basin. *Natural Gas Geoscience*. Vol.27 No.6 Jun.
- [4] Advanced Mathematics Teaching Research Group of Zhejiang University. (1985) *Engineering Mathematics Probability Theory and Mathematical Statistics*. Beijing: Higher Education Press, 21-26.
- [5] Wang Rongxin (1996) *Mathematical Statistics*. Xian: Xi'an Jiaotong University Press.
- [6] Zhang Zhenhong, Lv Xiuxiang et al. (2004) Petrogeologic feature of Wushi Sag in Talimu Basin. *Journal of Xi'an Shiyou University (Natural Science Edition)* Vol.18 No. 4Jul. 29-31+65-3.
- [7] Jia Jinhua, Zhou Dongyan et al. (2004) Petroleum geologic characteristics of Wushi Sag in Tarim Basin. *ACTA PETROLEI SINICA*. Vol.25 No.6Nov. 12-17.
- [8] Zheng Min, Peng Gengxin et al. (2008) Structural pattern and its control on hydrocarbon accumulations in Wushi Sag, Kuche Depression, Tarim Basin. *PETROLEUM EXPLORATION AND DEVELOPMENT*. Vol.35 No.4Aug. 444-451.
- [9] Zhang Bo, Li Jianghai et al. (2007) PRELIMINARY DISCUSSION ON GEOLOGICAL DISTRIBUTION OF METAMORPHIC CORE COMPLEX AND HYDROCARBON IN KUCHE DEPRESSION. *NATURAL GAS GEOSCIENCE*. Vol.18 No.2Apr. 200-203.
- [10] Yang Fan, Jia Jinhua (2006) Alluvial Fan and Fan-delta Sedimentary Facies and Favorable Assemblage of Reservoir and Seal of Wushi Sag (Cretaceous) in Tarmi Basin. *ACTA SEDIMENTOLOGICA SINICA* Vol.24 No.5Oct. 681-689.
- [11] Yu Hai, Chen Yong et al. (2008) The Way to Identify the Prior probability Distribution on the Base of Maximum Entropy Principle Risk. *CHINA SCIENCE AND TECHNOLOGY INFORMATION*. Feb. 276-277.



Decreasing the Cogging Torque using Virtual Positive Impedance Based Active Damping Control Method for PMSMs

Ahmet AKSÖZ^{1,*}, Ali SAYGIN²

¹ Cumhuriyet University/ Mechatronics Engineering Department, Sivas, TURKEY

² Gazi University/ Electrical and Electronics Engineering Department, Ankara, TURKEY

* Corresponding Author : aaksoz@cumhuriyet.edu.tr

ORCID: 0000-0002-2563-1218

Article Info:

DOI: 10.22399/ijcesen.522865
Received : 05 February 2019
Accepted : 27 February 2019

Keywords

ADC
PMSM
VPI.

Abstract:

In this paper, active damping control based virtual positive impedance for a PMSM driver is proposed. The proposed model is assumed to achieve the better motor current with a better harmonic response. 6 switches can be employed in the design of the driver to obtain high performance with a simultaneous reduction in the motor current harmonics and thus the torque ripple of PMSM. However, the reduction of input current harmonics is very important to operate the PMSM with less cogging torque. The proposed concept offers a significant decreasing in harmonics. Thus, the effect of VPI on the cogging torque can be understood. The inverter with a Field Oriented Control (FOC) method operates in 3-phase and 20 kHz switching frequency. The PMSM motor is fed by the inverter. The VPI based active damping control for the motor drive is discussed to confirm the performance of the proposed method. The simulation results based on MATLAB are provided to validate the proposed control strategy.

1. Introduction

Last trends in control methods area show that a better control approach supplies more desired results [1]. It means better control is the more efficiently system [1-5]. Especially, motor drivers must have more efficient. Because of the fact that complicated linear or nonlinear loads are used more than ever. Also using multi drivers cause more unexpected situation. Both variable speed drivers and adjustable speed drivers have the embedded diode-rectifier. It has high nonlinear characteristic due to nonsinusoidal input currents. However, this nonlinear characteristic leads more cogging torque on the motor, even if it is designed very well [6, 7]. In order to achieve longer lifetime drivers, the modulation of switch and inverter design must be succeeded beside the control method [8-11].

This paper investigates the cogging torque issue of PMSM. Using active damping control (ADC) and virtual positive impedance method (VPI), increasing

the performance of inverter is investigated. Thanks to desired inverter behaviour, the cogging torque of the motor can be decreased [12, 13].

A new inverter model is simulated according to the control method. Two case are designed and compared for understanding results of this control method on proposed cases. Case 1 is classical field oriented control (FOC) method without ADC based VPI method. And using ADC based VPI in FOC is case 2. After the simulation results, the DC bus voltage and motor currents are discussed.

2. System Description

2.1. Driver of the PMSM

This driver system, as shown in Fig. 1, consists of 5 divisions. They are a grid connected autotransformer, a diode rectifier, DC link capacitors, an inverter and a sensor card In Fig. 1, 400V-48Hz grid supplied the.

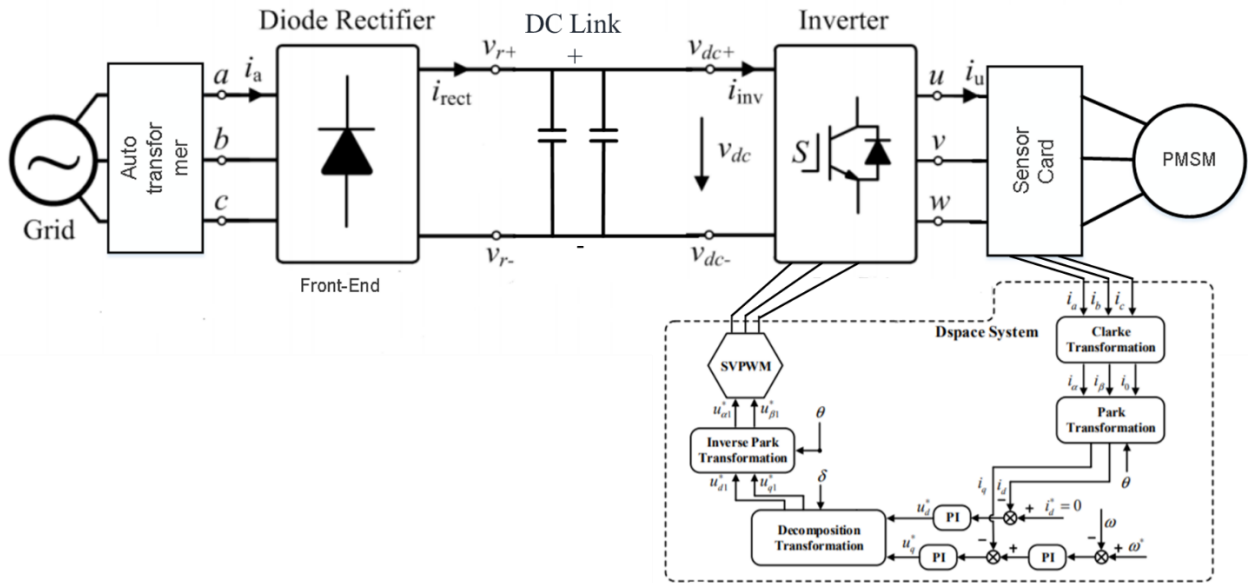


Figure 1. Driver Block Diagram.

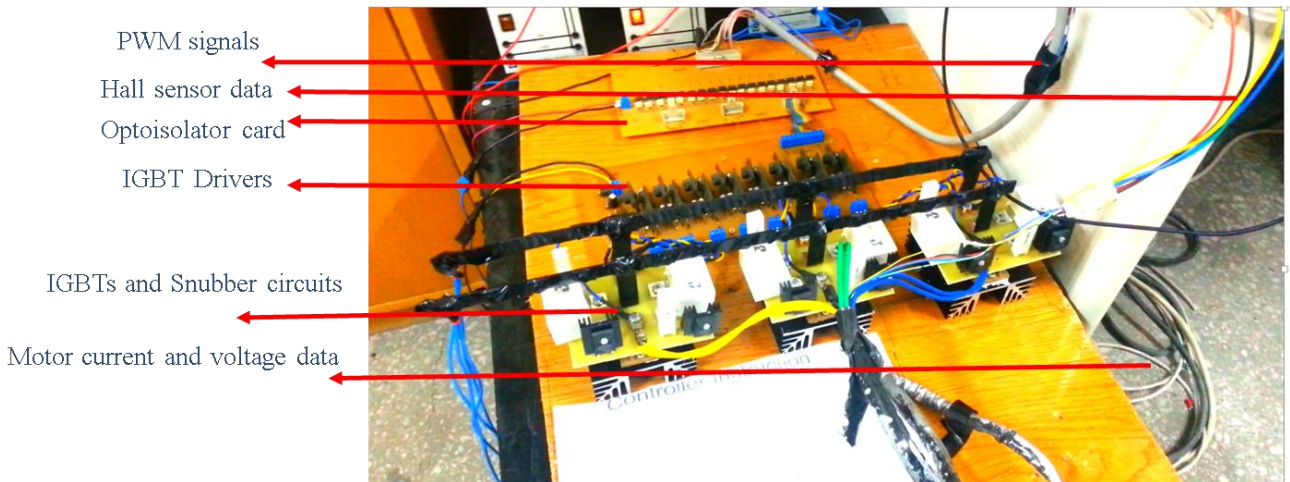


Figure 2. Inverter System

autotransformer transforms to voltage value from 400V to 48V. Then the diode rectifier rectifies AC 48V to DC 48V. Thanks to DC link capacitors, the DC voltage value gets closer to constant 48V with some voltage ripples. The inverter system feeds the motor with AC 50V. Lastly, the motor currents are measured from sensor card and transferred to DSpace system. PWM signals are generated using control method with or without ADC based VPI on d-q frame.

2.2. Inverter System

Designed and simulated inverter system is given in Fig 2. PWM signals, hall sensor data cables, an optoisolator card, IGBT drivers, IGBTs and snubber circuits and motor measuring data cables can be seen

below. Generated PWM signals are isolated from the optoisolator card. Then IGBT switches produce the AC voltage thanks to these PWM signals. Here, hall sensor data can be used when sensed position control is achieved. The block diagram of this inverter is illustrated in Fig 3 Above, the speed control and the position control can be desired in this inverter. But, only the speed control is realized in this study.

2.3. Control Methods

The virtual impedance method supplies less voltage ripples on DC link voltage. Thus, the inverter can be more stable thanks to more stable DC link voltage value. The VPI block diagram is displayed in Fig 4. Using VPI method, DC link voltage feedback go into

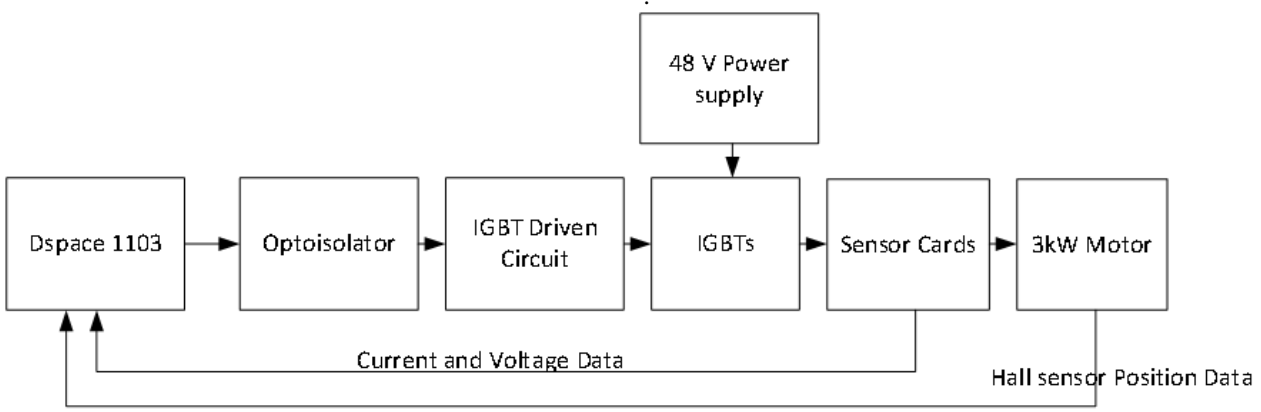


Figure 3. Block Diagram of Inverter

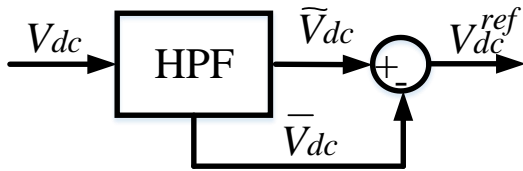


Figure 4. Block Diagram of VPI method.

HPF block. Firstly, the high pass process but totally the low pass operation is realized in this block. The DC reference voltage value is used for generating PWM signals. VPI method in FOC control and the FOC control block diagram in DSpace and simulation is given in Fig. 5. Clarke-Park Transformation and PI control are used in this FOC block.

3. Simulation of the System

Two cases are designed in Matlab by using Fig. 1, Fig. 2, Fig. 3, Fig. 4 and Fig. 5. The main difference of two cases is using ADC based VPI method in case 2. Thus, the cogging torque results are obtained from two cases. Table 1 gives the cogging torque results of two cases. Cogging torque results of 3kW-48V PMSM motor are represented in Table 1. The cogging torque value of Case 1 is 0.444Nm. When using ADC based VPI method, the cogging torque value is 0.327Nm for Case 2. Although two parallel 5e-2F capacitor filter the diode rectifier output, voltage ripples on the DC link voltage cause worse trapezoidal voltage signals in output of the inverter. But better voltage output and better results are obtained when ADC based VPI is used as seen in Fig. 6. This figure and results are come into by using Eq. 1,

Table 1. Cogging Torque Results.

Models	Cogging Torque (Nm)
Case 1	0.444
Case 2	0.327

Eq. 2, Eq. 3 and Eq. 4.

$$T_{cog} = \frac{1}{2} \phi_g^2 \frac{dR}{d\theta} \tag{1}$$

where ϕ_g is the air gap flux, dR is air gap reluctance and $d\theta$ is angle of rotation. Periodically changing the reluctance of the air gap causes periodically changing of the cogging torque. Because of this periodic variation, the value of the cogging torque can be calculated by the Fourier series.

$$T_{cog}(\theta_m) = \sum_{k=1}^{\infty} T_k \sin(kN_c\theta_m + \varphi_k) \tag{2}$$

where the rotor position is θ_m , T_k is the amplitude of k th harmonic, φ_k is the phase angle of k th harmonic and N_c is the least common multiple of rotor pole number and stator slot number. Also, the density of the surface flux of ideal slotless motor can be expressed as,

$$B_{rl}(\theta) = \sum_{n=1,3,5...}^{\infty} 2 \frac{\mu_0 M_n}{\mu_r} \frac{np}{(np)^2 - 1} \left(\frac{R_m}{R_s} \right)^{np+1} \left[\frac{(np-1) + 2 \left(\frac{R_m}{R_s} \right)^{np+1} - (np+1) \left(\frac{R_m}{R_s} \right)^{2np}}{\frac{\mu_r + 1}{\mu_r} \left[1 - \left(\frac{R_r}{R_s} \right)^{2np} \right] - \frac{\mu_r - 1}{\mu_r} \left[\left(\frac{R_m}{R_s} \right)^{2np} - \left(\frac{R_r}{R_m} \right)^{2np} \right]} \right] \cos(np\theta) \tag{3}$$

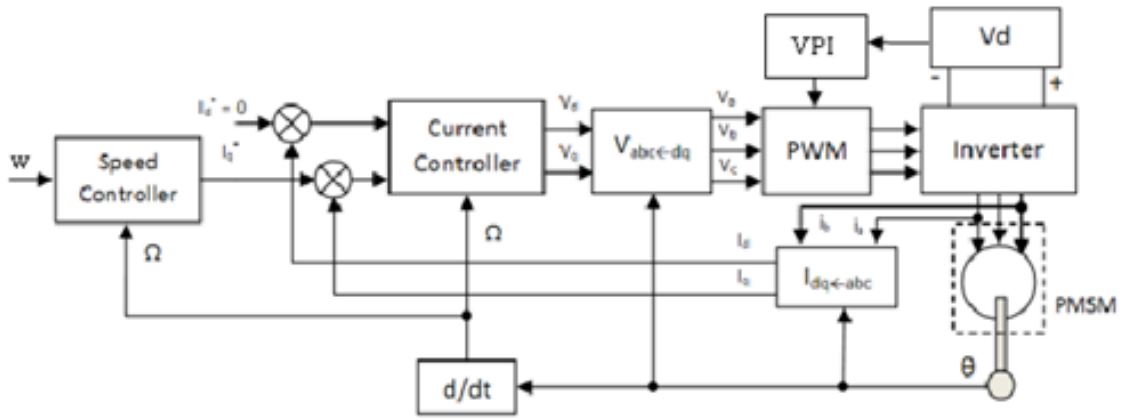


Figure 5. FOC Control Block Diagram

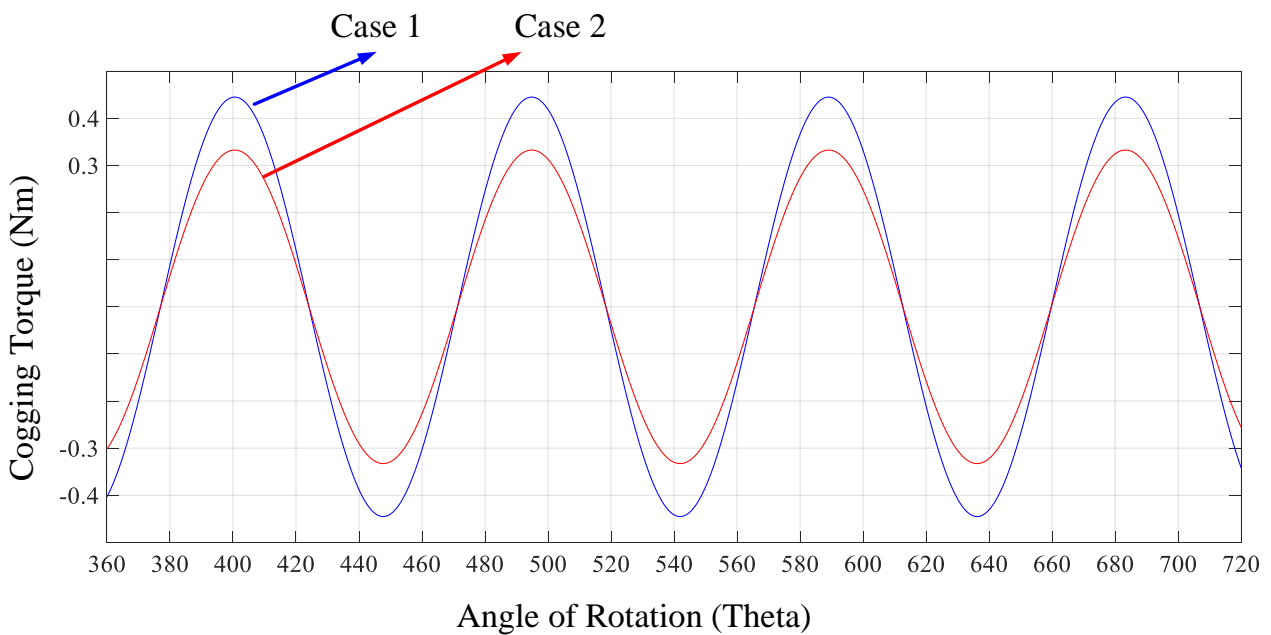


Figure 6. Cogging Torque of Two C

$$M_n = 2 \left(\frac{B_r}{\mu_0} \right) \alpha_p \frac{\sin\left(\frac{n\pi\alpha_p}{2}\right)}{\frac{n\pi\alpha_p}{2}} \quad (4)$$

where R_m is the outer radius of the magnet, R_s is the outer radius of the stator, R_r is the outer radius of the rotor, p is the double pole number and α_p is the pole step.

4. Conclusion

The active damping control based virtual positive impedance is developed for a PMSM driver is FOC control. After two cases are designed, the better motor current with less voltage ripple on the DC link voltage is get by ADC based VPI method. In order to achieve longer lifetime and high performance motor driver, it must be more stable with less voltage ripple and less cogging torque. Simulated cases show that the more stable driver and the less cogging

torque can be obtained using ADC based VPI method in FOC.

Acknowledgement

Authors thanks to TUBITAK 2211-A (Grant number: 1649B031400107).

References

- [1] A. Saygin, A.M. Rashid, Position control of a turret using LabVIEW, Acta Physica Polonica A (2017) 132 (3), pp. 970-973. DOI: 10.12693/APhysPolA.132.970
- [2] S. Altuntaş, H. Hapoğlu, S. Ertunç, M. Alpbaz, Experimental Self-Tuning Proportional Integral Derivative pH Control: Application to a Bioprocess, Acta Physica Polonica A (2017) pp 1006. DOI: 10.12693/APhysPolA.132.1006

- [3] M.K. Döşoğlu, U. Güvenç, Y. Sönmez, C. Yılmaz, Enhancement of demagnetization control for low-voltage ride-through capability in DFIG-based wind farm, *Electrical Engineering*, (2018) 100 (2), pp. 491-498. DOI: 10.1007/s00202-017-0522-6
- [4] N.G. Adar, R. Kozan, Comparison between Real Time PID and 2-DOF PID Controller for 6-DOF Robot Arm, *Acta Physica Polonica A* (2016) pp 269. DOI:10.12693/APhysPolA.130.269
- [5] N.G. Adar, A. Egrisogut Tiriyaki, R. Kozan, Real Time Visual Servoing of a 6-DOF Robotic Arm using Fuzzy-PID Controller, *Acta Physica Polonica A* (2015) pp B-348. DOI: 10.12693/APhysPolA.128.B-348
- [6] Y. Sarikaya, H. Apaydin, Ş. Kıtış, A Hydrolysis System Design and Ana-lysis for Vehicles with Microprocessor Based and PWM Controlled Card, *Acta Physica Polonica A* (2015) pp B-211. DOI: 10.12693/APhysPolA.128.B-211
- [7] A. Saygin, A. Aksoz and E. N. Yilmaz, A different model of WECS connected to smart grid through matrix converter, 2016 4th International Istanbul Smart Grid Congress and Fair (ICSG), Istanbul (2016), pp. 1-5. DOI: 10.1109/SGCF.2016.7492419
- [8] E.N. Yilmaz, A. Aksoz and A. Saygin, *Electr Eng* (2018).DOI: 10.1007/s00202-018-0734-4
- [9] E. Can, H.H. Sayan, A novel SSPWM controlling inverter running nonlinear device, *Electrical Engineering*, (2018) 100 (1), pp. 39-46. DOI: 10.1007/s00202-016-0480-4
- [10] E. Can, H.H. Sayan, The increasing harmonic effects of SSPWM multilevel inverter controlling load currents investigated on modulation index, *Tehnicki Vjesnik*, (2017) 24 (2), pp. 397-404. DOI: 10.17559/TV-20151020134629
- [11] A. Saygin, A. Kerem, Speed control of an induction motor by 6-switched 3-level inverter, *Open Physics*, (2017) 15 (1), pp. 1072-1076. DOI: 10.1515/phys-2017-0138
- [12] R. Kiliç, Determination of Imbalance Problem in Electric Motor and Centrifugal Pump by Vibration Analysis, *Acta Physica Polonica A* (2016) pp487. DOI:10.12693/APhysPolA.130.487
- [13] A. Saygin and A. Aksoz, Design optimization for minimizing cogging torque in Axial Flux Permanent Magnet machines, 2017 International Conference on Optimization of Electrical and Electronic Equipment (OPTIM) Brasov (2017), pp. 324-329. DOI: 10.1109/OPTIM.2017.7974991



Natural Radiation Measurement in Some Soil Samples from Basra oil field, IRAQ State

Hadi AL-BAIDHANI^{1*}, Kadir GUNOGLU² and Iskender AKKURT¹

¹ Suleyman Demirel University/Department of physics, Isparta, TURKEY

² Suleyman Demirel University /Technical Vocational School, Isparta, TURKEY

* Corresponding Author : hadi_albadany@yahoo.com

ORCID: 0000-0001-9230-1510

Article Info:

DOI: 10.22399/ijcesen.498695

Received : 30 December 2018

Accepted : 01 March 2019

Keywords

Radiation
Soil
Uranium
Thorium

Abstract:

The main objective of this project is to study the natural radioactivity in the oil field environment, and its potential future effects on the workers in particular and the environment in general when increasing the concentration of natural radionuclides resulting from oil extraction. This is done by collecting a number of soil samples, were taken from one of the oil fields north of the Basra city, and the measurement was performed using a gamma ray spectrometry that contains a 3"x3" NaI(Tl) detector at gamma spectrometry laboratory of Süleyman Demirel University,Isparta-Turkey. The normal radioactivity of radionuclides for natural isotopes ²³⁸U, ²³²Th and ⁴⁰K are evaluated after measuring by comparing results with worldwide average values in natural soil. The average values of the measurement results were within the worldwide average values, and there were increase Radioactivity concentrations of Radium and potassium in sample 3, that required monitoring to this site for any increase in radioactivity, also to taking of the preventive measures.

1. Introduction

The exposure of Radiation is varying in the environment; some of them come from industrial sources as Medical exposure sources (X-ray), or from natural sources which are found around us, such as cosmic rays and terrestrial radiation [1].

The natural terrestrial radioactivity is present resulting of radionuclides already present in the earth's crust with different concentrations in nature, which does not pose a risk to the environment unless there are human processes and activities that lead to an increase in the concentration of radionuclides and concentration of activity which leads to exposure to radiation risk, as a Mineral exploration, coal mine drilling, and oil and gas extraction [2].

The natural radionuclides found in geological deposits are occurring from decay to the natural elements with a long half-life, such as uranium-238, thorium-232, and potassium-40. The produce radionuclides by this decay are transferred through

the pores of the rocks to the oil formations places, they brought to the surface by produced water that accompanying with oil extracted in the form of soluble salts such as Radium-226 salts, The changes of some physical factors such as pressure or temperature etc. leads to accumulation of sediments Inside the oil equipment in different forms, containing radionuclides that are more concentrated by increasing the accumulation of those sediments which lead to the reduction of oil production over time, which requires to cleaning of the equipment periodically and continuously, which leads exposure of radiation risk to the workers and pollution of land surrounding the oil fields and the environment if they are not handled safely and uncontrolled to prevent their spread [3].

In the literature, some researchers have carried out a series of studies to identify and evaluate ²²⁶Ra, ²³²Th and ⁴⁰K activity concentrations in environmental samples such as stone, soil in various parts of the world [4-16].

In this study, ^{226}Ra , ^{232}Th and ^{40}K activity concentrations of 4 soil samples that collected from one of the oil fields north of the Basra city were measured.

2. Materials and Methods

2.1 Area of Study

Basra oil fields, a group of oil wells discovered, which is actually investment of oil and extends from the middle of the west of Basra to the north of Kuwait, includes a vast area of 1,600 Km². Basra fields are divided into two parts the Northern Basra and the Southern Basra close to Kuwait, see Figure 1. The type of oil extracted in this field from sandstone layers, at depths of up to four kilometres, Sand formations are characterized by their high quality, which has an average porosity of 20% in addition to high permeability.

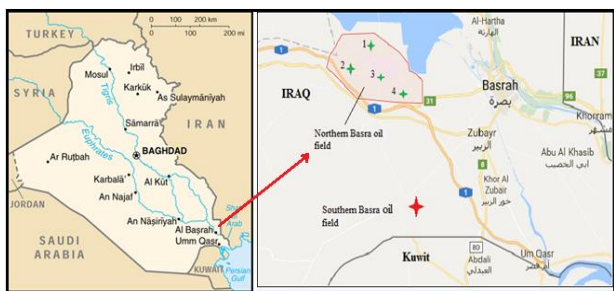


Figure 1. Samples location of Basra oil fields on Iraq map

2.2 Sample Collection and Preparation

Randomly four soil samples from the area shown in the Figure 1 were taken from the surfaces near to the different oil equipment at Northern Basra oil field. All samples were dried to remove moisture using an oven at 100 °C for 12 hours; About 200 g for each sample was taken after removal of stones and biological parts by using a 1mm sieve and then filled in a special plastic counting container. The containers were stored for one month before counting its radioactivity allowing for achieving the equilibrium between isotopes of ^{226}Ra , ^{228}Ra , and decay of its products.

2.3 Radioactivity Measurement

The natural radioactivity of the radionuclides that emit gamma-ray can be measured based on the high penetration strength of the gamma-rays in materials, using electronic counting and analysis system used in the detection of nuclear radiation, from the sodium iodide detector with thallium NaI(Tl) that have dimension (3" × 3") which was connected with high voltage (HV), preamplifier and

multichannel analyser, (ORTEC-Digit Base) which contains 16384 channel, connects In a unit called ADC (Analog to Digital Converter) Helps the analyst to convert the coming pulse into digital form, Radiation measurements and analysis are done by computer software called (MAESTRO-32) to record data, as illustrated in figure. 2

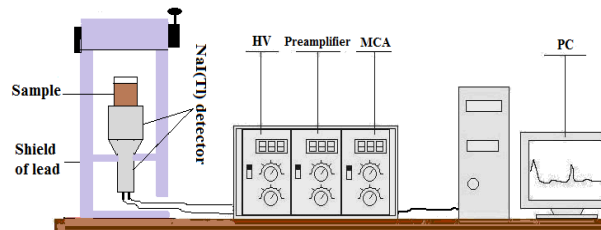


Figure 2. Schematic of gamma-ray spectrometer system

The radioactivity measurement of the samples was done after measuring the background radiation; by subtracting the value of radiation background from the value of radioactivity of the measured sample we obtain the net of the radioactivity, in the same time period as the sample measurement (84000) sec. The qualitative analysis is depending on determining the gamma-ray energy emitted from the measured sample, and recording of quantities for the natural radioactivity of isotopes ^{226}Ra , ^{232}Th , and ^{40}K which are counted its energies from the photo peak which equal to 1760, 2610, and 1461 keV, respectively [4], as illustrated in figure.3

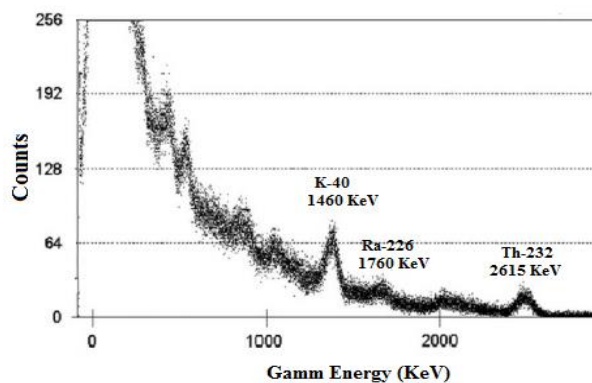


Figure 3. A spectrum measurement for natural radioactivity

In the quantitative analysis, the radioactivity was calculated by calculating the net area under the photo peak of gamma-ray to infer the concentration of radioisotope in the sample. The activities for the natural radionuclides of ^{40}K , ^{226}Ra and ^{232}Th in the measured samples at Becquerel per unit mass Bq/kg were calculated using the following relation [4].

$$A = \frac{N_{net}}{\epsilon \cdot \gamma \cdot t \cdot m} \quad (1)$$

where A is the radioactivity of measured radionuclides in Bq/kg, N_{net} is the net count rate

area under the photopeaks calculated from (Total counts – background counts), ϵ is the efficiency of detector to emitted gamma rays, γ is the relative intensity of all gamma energy emitted, t is the time of counting and m is a mass of sample in (kg).

3. Results and Discussion

The activity concentration of the radionuclides for the 4 soil samples from North Basra oil field were obtained using the relation 1 and given in Table 1.

Table 1. The radioactivity concentration in soil samples

Sample Id	⁴⁰ K (Bq/Kg)	²²⁶ Ra (Bq/Kg)	²³² Th (Bq/Kg)
1	430.3475	18.562	19.1908
2	403.1239	27.961	22.2103
3	684.3209	62.533	25.8814
4	528.624	25.297	15.3056
Average	511.604	33.588	20.647

In this table, it can be seen the activity variation for these samples. The radioactivity of natural radionuclides is evaluated after measuring by comparing results with worldwide average values in natural soil. The worldwide average value of ⁴⁰K, ²²⁶Ra, and ²³²Th in the normal soil is 400, 35, and 30 Bq/kg, respectively [17,18]. It can be seen that activity concentration of ⁴⁰K for all samples are more than the worldwide average value and activity concentration of ²²⁶Ra for sample 3 more than the worldwide average value. While the activity concentration value of the other samples was lower, these results are displayed in Figure 4 and Figure 5. In Table-2, the activity concentrations of the ⁴⁰K, ²³²Th and ²²⁶Ra radionuclides obtained in this study were compared with similar studies in different countries and with recommended limit values.

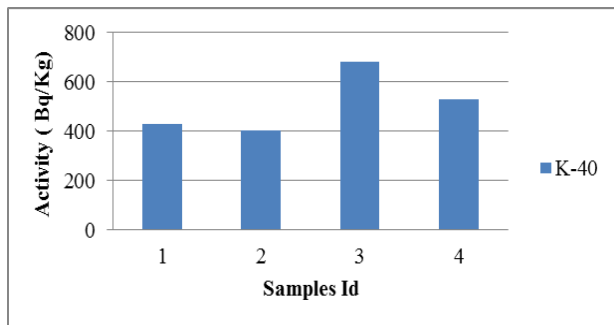


Figure 4. Activity concentrations of ⁴⁰K

4. Conclusion

The average activity results obtained from the

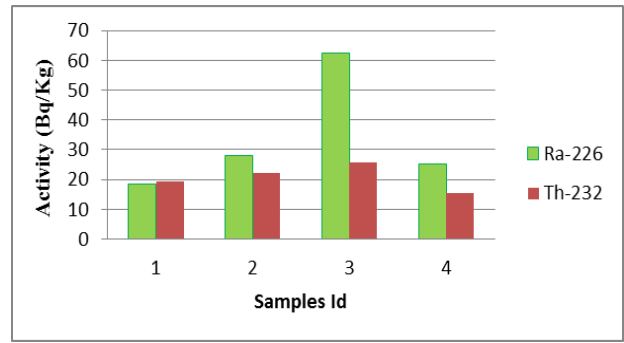


Figure 5. Activity concentrations of ²²⁶Ra and ²³²Th

Table 2. A comparison of radioactivity content from other parts of the world.

Location	Activity concentration (Bq/kg)			References
	⁴⁰ K	²²⁶ Ra	²³² Th	
Egypt	21,1	930	11,6	[19]
Saudi Arabia	641,08	11,42	19,26	[20]
Thailand	523	22,6	26,4	[21]
Malaysia	369	31	36	[22]
Palestine	113	41	19	[23]
Pakistan	575	31	44	[24]
Nigeria	710	25	77	[25]
Turkey	12,2	157,7	9	[26]
Saudi Arabia	153,8	11,3	6,7	[27]
World (average)	400	35	30	[17]
Iraq	511,6	33,59	20,65	This Work

measurements are consistent with the activity values given in the UNSCEAR 2000 reports for all samples except for the ⁴⁰K activity values. Therefore, these activity concentrations are acceptable levels for human health or environmental pollution.

Acknowledgement

The Authors would like to thanks to Iraq Ministry of oil and Suleyman Demirel University, Turkey for supporting these research activities.

References

- [1] Australian Radiation Protection and Nuclear Safety Agency (ARPANSA). Management of Naturally Occurring Radioactive Material (NORM) No. 15. (2008).
- [2] Khadhim, N. F., & Adnan, O. H, 2016. Measurement of natural radioactivity in Al-Dora Refinery by using (HPGe) detector.

- [3] AL-MASRI, M. S., SUMAN, H., NORM waste in the oil and gas industry: the Syrian experience, *J. Radioanal. Nucl. Chem.* 256, (2003), 159-162.
- [4] Akkurt I. and Gunoglu, K., 2014. Natural Radioactivity Measurements and Radiation Dose Estimation in Some Sedimentary Rock Samples in Turkey. *Science and Technology of Nuclear Installations Volume 2014*, Article ID 950978
- [5] Akkurt, I., Oruncak, B., Gunoglu, K., 2010. Natural radioactivity and dose rates in commercially used marble from Afyonkarahisar – Turkey. *International Journal of the Physical Sciences Vol. 5* (2), p:170-173.
- [6] Günay O., 2018, Determination of Natural Radioactivity and Radiological Effects in some Soil Samples in Beykoz-Istanbul, *European Journal of Science and Technology No. 12*, pp. 9-14, April 2018 ISSN:2148-2683
- [7] Carvalho, C., Anjos, R.M., Veiga, R., Macario, K., 2011. Application of radiometric analysis in the study of provenance and transport processes of Brazilian coastal sediments. *J. Environ. Radioact.* 102, 185–192. <https://doi.org/10.1016/j.jenvrad.2010.11.011>
- [8] İskender AKKURT, N. Ayten UYANIK, Kadir GÜNOĞLU “Radiation dose Estimation: An in vitro Measurement for Isparta-Turkey” *IJCESEN 1-1(2015)1-4* DOI: 10.22399/ijcesen.194376
- [9] Carvalho, C., Anjos, R.M., Veiga, R., Macario, K., 2011. Application of radiometric analysis in the study of provenance and transport processes of Brazilian coastal sediments. *J. Environ. Radioact.* 102, 185–192. <https://doi.org/10.1016/j.jenvrad.2010.11.011>
- [10] Günay, O. (2018). Assessment of lifetime cancer risk from natural radioactivity levels in Kadikoy and Uskudar District of Istanbul. *Arabian Journal of Geosciences*, 11(24), 782.
- [11] Ramasamy, V., Sundarajan, M., Paramasivam, K., Suresh, G., 2015. Spatial and depth wise characterization of radionuclides and minerals in various beach sediments from high background radiation area, Kerala, India. *Appl. Radiat. Isot.* 95, 159–168.
- [12] Seçkiner S., Akkurt, I., Günoglu K., 2017, Determination of 40K concentration in gravel samples from Konyaaltı Beach, Antalya. *Acta Phys. Pol. A.*, Vol 132 (3-II), 1095-1097, doi: 10.12693/APhysPolA.132.1095.
- [13] I Akkurt, B Oruncak, K Gunoglu 2010, Natural radioactivity and dose rates in commercially-used marble from Afyonkarahisar-Turkey *International Journal of Physical Sciences 5* (2), 170-173
- [14] NA Uyanık, O Uyanık, İ Akkurt 2013, Micro-zoning of the natural radioactivity levels and seismic velocities of potential residential areas in volcanic fields: The case of Isparta (Turkey) *Journal of Applied Geophysics 98*, 191-204
- [15] B Çetin, F Öner, I Akkurt 2016, Determination of natural radioactivity and associated radiological hazard in excavation field in Turkey (Oluz Höyük) *Acta Physica Polonica A 130* (1), 475-478
- [16] NA Uyanık, I Akkurt, O Uyanık 2011, A ground radiometric study of uranium, thorium and potassium in Isparta, Turkey *Annals of Geophysics 53* (5-6), 25-30
- [17] UNSCEAR, 2000. Sources and effects of ionizing radiation. United Nations Scientific Committee on the effect of atomic radiation. Report to the General Assembly, with Scientific Annexes. United Nations, New York.
- [18] N. Zaim, A.B. Tugrul, H. Atlas, B. Buyuk, E. Demir. Investigation of Natural Radioactivity of Surface Soil Samples in the Vicinity of Edirne - Turkey, *Acta Physica Polonica A*, page 64 (2016), DOI: 10.12693/APhysPolA.130.64.
- [19] Harb, S., 2008. Natural radioactivity and external gamma radiation exposure at the coastal Red Sea in Egypt. *Radiat. Prot. Dosimetry 130* (3), 376–384.
- [20] Al-Trabulsi, H., Khater, A., Habbani, F., 2011. Radioactivity levels and radiological hazard indices at the Saudi coastline of the Gulf of Aqaba. *Radiat. Phys. Chem.* 80, 343–348.
- [21] Malain, D., Regan, P.H., Bradley, D.A., Matthews, M., Al-Sulaiti, H.A., Santawamaitre, T., 2012. An evaluation of the natural radioactivity in Andaman beach sand samples of Thailand after the 2004 tsunami. *Appl. Radiat. Isot.* 70 (8), 1467–1474.
- [22] Almayahi, B.A., Tajuddin, A.A., Jaafar, M.S., 2012. Effect of the natural radioactivity concentrations and 226Ra/238U disequilibrium on cancer diseases in Penang, Malaysia. *Radiat. Phys. Chem.* 81, 1547–1558.
- [23] Abu Samreh MM, Thabayneh KM, Khrais FW (2014) Measurement of activity concentration levels of radionuclides in soil samples collected from Bethlehem Province, West Bank, Palestine. *Turk J Eng Environ Sci* 38:113–125.
- [24] Rafique M, Ur Rahman S, Basharat M, Aziz W, Ahmad I, Lone KA, Ahmad K, Matiullah M (2014) Evaluation of excess life time cancer risk from gamma dose rates in Jhelum valley. *Journal of Radiation Research and Applied Sciences* 7:29–35.
- [25] Oyeyemi KD, Usikalu MR, Aizebeokhai AP, Achuka JA, Jonathan O (2017) Measurements of radioactivity levels in part of Ota Southwestern Nigeria: Implications for radiological hazards indices and excess life-time cancer-risks IOP. *Conf. Series: Journal of Physics: Conf. Series* 852:1–8.
- [26] Özmen, S.F., Cesur, A., Boztosun, I., Yavuz, M., 2014. Distribution of natural and anthropogenic radionuclides in beach sand samples from Mediterranean Coast of Turkey. *Radiat. Phys. Chem.* 103, 37–44.
- [27] Al-Ghamdi, H., Al-Muqrin, A., El-Sharkawy, A., 2016. Assessment of natural radioactivity and 137 Cs in some coastal areas of the Saudi Arabian gulf. *Mar. Pollut. Bull.* 104, 29–33.



Experimental Comparison of Al5083 Alloy Subjected to Annealing and Equal-Channel Angular Pressing

Mehmet ŞAHBAZ^{1,2*}, Hasan KAYA³, Aykut KENTLİ¹, Mehmet UÇAR⁴, Serkan ÖĞÜT¹, Kerim ÖZBEYAZ¹

¹ Marmara University, Faculty of Engineering, Mechanical Engineering Department, İstanbul-Turkey

² Karamanoglu Mehmetbey University, Mechanical Engineering Department, 70100, Karaman, Turkey

³ Kocaeli University, Asım Kocabıyık Vocational School, Machine and Metal Technology Dep., Kocaeli-Turkey

⁴ Kocaeli University, Faculty of Technology, Department of Automotive Engineering, Kocaeli-Turkey

* Corresponding Author : mehmentsahbaz1@gmail.com

ORCID: 0000-0001-6379-8345

Article Info:

DOI: 10.22399/ijcesen.394542

Received : 13 February 2018

Accepted : 04 March 2019

Keywords

Al5083

ECAP

SPD

Microstructure

Hardness

Abstract:

In this study, the hardness and electrical resistivity of Al5083 alloy were investigated after equal-channel angular pressing (ECAP) and annealing processes. The effects of the annealing and ECAP processes on the properties of the alloy were investigated, and the results of the processes were compared with each other. The major reason for the different results between the two processes was changes in the microstructure, which were observed by optical microscopy and scanning electron microscopy. The results showed that, ECAP decrease the grain size, in parallel with it increase the hardness and electrical resistivity of material.

1. Introduction

Equal-channel angular pressing (ECAP) is a well-known severe plastic deformation (SPD) method. ECAP is indeed an extrusion method; however, to obtain ultrafine grains, it is carried out with the material at a temperature under its recrystallization temperature. The difference between ECAP and other plastic deformation methods is that it can be applied several times to the same material. In addition, traditional deformation methods decrease the toughness while increasing the hardness of a material. The material is thus made more brittle, which is undesirable in many applications. After the ECAP process, the geometrical shape or the cross-section of the material is unchanged; the workpiece can therefore be passed numerous times through the ECAP die, further reducing the grain size with each pass. This process increases the hardness and strength of the material according to the Hall–Petch relationship (Eq.1), without affecting the toughness. The Hall–Petch equation is given as

$$\sigma_a = \sigma_0 + \frac{k}{\sqrt{d}} \quad (1)$$

where σ_a is the yield stress for a polycrystalline material, σ_0 is yield stress for a single crystal, k is a constant, and d is the grain size. ECAP is generally used for nonferrous alloys of aluminum, magnesium, and copper because of their excellent properties. ECAP-treated materials can be used in numerous application fields, including machine parts that require high toughness, aerospace devices that require lightweight materials and defense vehicles that require high strength [1-7]. In the present study, we investigate the hardness and electrical resistivity of Al5083 alloy specimens subjected to ECAP and annealing processes [8-9].

2. Materials and Methods

In this study, AA5083 was selected for workpieces because of its high strength among non-heatable alloys. Impax Supreme (1.2738) steel was used to

produce the hexa-die, whereas 1.2344 steel was used for the pins (or top die). The pressing process was carried out using a 120-ton-capacity hydraulic press, and a high-temperature industrial furnace was used for the annealing and heating processes. The workpiece was produced from extruded bulk material as a cylinder with a diameter of 20 mm and a length of 55 mm. The traditional ECAP process was selected as the processing method; the applied steps are described in section 2.1.

2.1. Experimental Setup

Firstly, the workpieces were homogenized at 520°C for 2 h and then cooled to room temperature by natural convection. Secondly, the specimen and die were heated to 350°C for pressing. After the specimen was lubricated with MoS₂, it was pressed using a hydraulic press along the channel of the hexa-die. The channel angle and corner angle of the hexa-die were 90° and 0°, respectively. The pressing speed was constant at 1 mm/s in these experiments. During the pressing operation, the workpiece was positioned in the top channel of the die and pressed with the top die, as shown in Figure 1. The channel used for pressing was left open, whereas the other channels were closed with pins. The sample flowed through the open channel under the applied hydraulic force. In Figure 2a, half of the hexa-die is shown along with the workpiece and pins after the pressing operation. Figure 2b shows the pressed sample after ejection from the die.

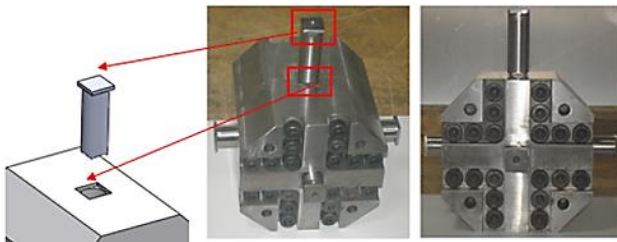


Figure 1. A schematic and pictures of the hexa-die with pins [4]

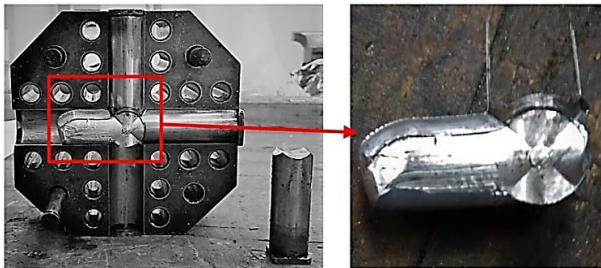


Figure 2. The pressed sample a) in the hexa-die and b) after ejection from the die

2.2. Tests and Analyses

After the ECAP process, three samples were prepared for tests and comparisons of each process. The first sample was in the as-received state (pre-hardened), the second sample was annealed, and the third sample was that obtained after the ECAP process. The samples were prepared for metallographic examination using optical microscopy (OM) and scanning electron microscopy (SEM) to measure their grain sizes. For these observations, the samples were molded with Bakelite and then finely ground, polished, and etched. OM and SEM observations in conjunction with energy-dispersive X-ray spectroscopy (EDS) measurements were then performed. The electrical resistivity and hardness of the samples were subsequently measured.

3. Results and Discussion

This part of the paper includes the result and discussion of the all applied test on three state of AA5083 before and after ECAP operation. The tests can be ordered as OM and SEM imaging, EDS analysis, electrical resistivity and hardness tests.

3.1. Optical Microscopy

OM was used to assess whether the surface of each sample was suitable for SEM analysis. For this aim specimens were prepared with sandpapers and diamond cloths, then etched with Keller's reagent. Figure 3 shows, from left to right, OM images of the as-received, annealed, and ECAP-treated samples with 100µm scales. These images reveal that, compared with the as-received sample, the annealed sample exhibits reduced porosity and the ECAP-treated sample exhibits a smaller average grain size.

3.2. SEM and EDS Analyses

SEM was used to observe and measure the fine grain sizes of the samples for comparison. The same precipitations were observed at the grain boundaries of all of the samples; these precipitations resist dislocation propagation and increase the strength in the ECAP-treated sample, whereas they increase the electrical conductivity of the annealed sample. Below figure presents, SEM image of the ECAP-treated samples. After that, EDS spectrum of the AA5083 alloy and its corresponding chemical composition are shown in Figure 4.

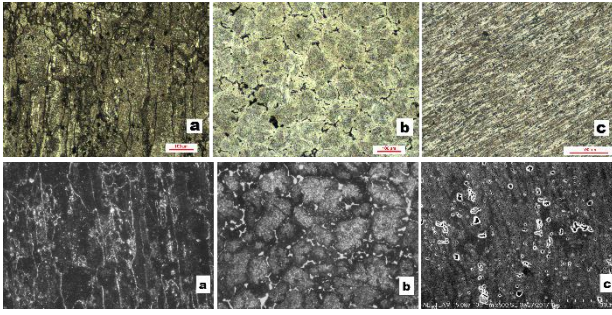


Figure 3. OM and SEM micrographs of the a) as-received, b) annealed, c) ECAP-treated samples

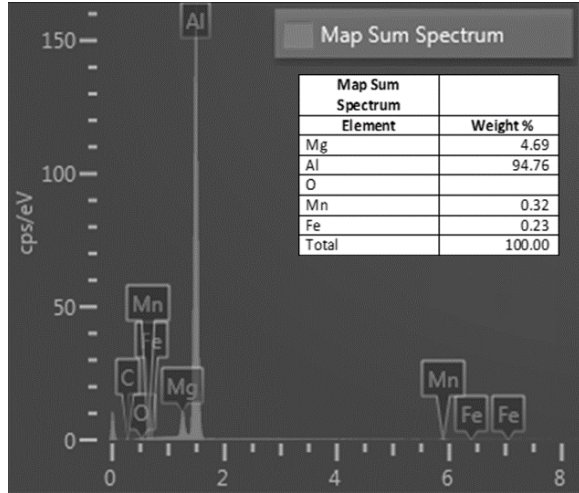


Figure 4. EDS spectrum and the corresponding chemical composition of the AA5083 alloy

3.3. Electrical Resistivity

Electrical resistivity tests were performed on the surfaces of the three workpieces using a four-point probe device. During the tests, a constant current was supplied to the sample via the two outside probes and the voltage was measured by the two inner probes. At the end of the tests, the measured voltages for all of the samples differed from the electrical resistivity calculated using the main equation. The electrical resistivity of the as-received AA5083 was $5.9 \times 10^{-6} \Omega \cdot \text{cm}$; the samples subjected to the annealing and ECAP processes exhibited minimal lower and higher electrical resistivity values, respectively. It showed that, grain size change with SPD has negligible effect on the electrical resistivity of AA5083 material [10].

3.4. Hardness Test

The Vickers method was used for the hardness tests; the test parameters included an applied load of 1000 g and a dwell time of 9 s. The annealing process decreased the hardness, whereas the ECAP process increased it, as expected (Table 1).

Table 1. Vickers hardness of samples

Sample	Vickers Hardness
As-received	91.6
Annealed	80.3
ECAP-treated	121.1

The annealing process increased the grain size of the material and eliminated some inner stresses; thus, the hardness of the material decreased. By contrast, the ECAP process substantially decreased the grain size of the material, resulting in an increase in hardness.

4. Conclusion

Al5083 alloy was investigated, and the workpieces in the annealed, ECAP-treated, and as-received (unprocessed) states were subjected to hardness tests and electrical resistivity tests. OM, SEM, and EDS analyses were carried out to characterize the change of the grain size of the material. The obtained results are summarized as follows:

- Hardness increased as a result of the ECAP process, whereas it decreased as a result of the annealing process.
- Electrical resistivity (at the least) increased as a result of the annealing process, whereas it decreased as a result of the ECAP process.
- OM and SEM images showed that the average grain size decreased as a result of the ECAP process, whereas it increased as a result of the annealing process and some precipitations formed at the grain boundaries.
- EDS analyses showed that the chemical composition was nearly same after each treatment.

Acknowledgment

This work was supported by the Marmara University Scientific Research Project within project number FEN-C-DRP-120417-0183. Paper presented as abstract at "4th International Conference on Computational and Experimental Science and Engineering (ICCESEN-2017)"

References

- [1] Valiev, R. Z., Islamgaliev, R. K., Alexandrov, I. V. "Bulk nanostructured materials from severe plastic deformation". *Progress in Materials Science*, 45(2), pp. 103–189. 2000. DOI:10.1016/S0079-6425(99)00007-9
- [2] Valiev, R. Z., Langdon, T. G. "Principles of equal-channel angular pressing as a processing tool for grain

- refinement”. *Progress in Materials Science*, 51(7), pp. 881–981, 2006. DOI: 10.1016/j.pmatsci.2006.02.003
- [3] Kaya, H., Uçar, M. “The effects of mechanical properties on fatigue behavior of ecap’ ed aa7075”. *High temperature materials and processes*, 35(3), pp. 225–234, 2016. DOI: 10.1515/htmp-2014-0193
- [4] Kaya, H., Uçar, M., Cengiz, A., Samur, R., Özyürek, D., Çalışkan, A. “Novel molding technique for ECAP process and effects on hardness of AA7075”. *Mechanika*, 20 (1), pp. 5–10, 2014. DOI: 10.5755/j01.mech.20.1.4207
- [5] Need, R.F., Alexander, D.J., Field, R.D., Livescu, V., Papin, P., Swenson, C.A., Mutnick, D.B. “The effects of equal channel angular extrusion on the mechanical and electrical properties of alumina dispersion-strengthened copper alloys”. *Materials Science and Engineering A*, 565, pp. 450–458, 2013. DOI: 10.1016/j.msea.2012.12.007.
- [6] Singh, D., Jayaganthan, R., Nageswara Rao, P., Kumar, A. & Venketeswarlu, D. ‘Effect of initial grain size on microstructure and mechanical behavior of cryorolled AA 5083’, *Materials Today: Proceedings*, 4 (8), pp. 7609–17, 2017. DOI: 10.1016/j.matpr.2017.07.094
- [7] Esgin, U., Özyürek, D., KAYA, H. “Investigation of wear behavior of precipitation-strengthened nickel-copper based K-500 alloy produced by powder metallurgy”. *Acta Physica Polonica A*, 129, pp. 544–547, 2016. DOI: 10.12693/APhysPolA.129.544
- [8] Chen, Y. J., Chai, Y. C., Roven, H. J., Gireesh, S. S., Yu, Y. D., & Hjelen, J. “Microstructure and mechanical properties of Al-xMg alloys processed by room temperature ECAP”. *Materials Science and Engineering: A*, 545, pp. 139–147, 2012. DOI: 10.1016/j.msea.2012.03.012
- [9] Fakhar, N., Fereshteh-Saniee, F., & Mahmudi, R. “High strain-rate superplasticity of fine- and ultrafine-grained AA5083 aluminum alloy at intermediate temperatures”. *Materials & Design*, 85, 342–348, 2015. DOI: 10.1016/j.matdes.2015.06.158
- [10] Lipińska M, Bazarnik P, Lewandowska M. “The influence of severe plastic deformation processes on electrical conductivity of commercially pure aluminium and 5483 aluminium alloy”. *Archives of Civil and Mechanical Engineering*, 16 (4), pp. 717–23. 2016 DOI: /10.1016/j.acme.2016.04.013